Development of a Wind Turbine Test Rig and Rotor for Trailing Edge Flap Investigation

by

Ahmed Abdelrahman

A thesis
presented to the University of Waterloo
in fulfillment of the
thesis requirement for the degree of
Masters of Applied Science
in
Mechanical Engineering

Waterloo, Ontario, Canada, 2014

I hereby declare that I am the sole author of this thesis. This is a true copy of the thesis, including any required final revisions, as accepted by my examiners.

I understand that my thesis may be made electronically available to the public.

Abstract

Alleviating loads on a wind turbine blades would allow a reduction in weight, and potentially increase the size and lifespan of rotors. Trailing edge flaps are one technology proposed for changing the aerodynamic characteristics of a blade in order to limit the transformation of freestream wind fluctuations into load fluctuations within the blade structure. An instrumented wind turbine test rig and rotor were developed to enable a wide-range of experimental set-ups for such investigations. The capability of the developed system was demonstrated through a study of the effect of stationary trailing edge flaps on blade load and performance. The investigation focused on measuring the changes in flapwise bending moment and power production for various trailing edge flap parameters. The blade was designed to allow accurate instrumentation and customizable settings, with a design point within the range of wind velocities in a large open jet test facility. The wind facility was an open circuit wind tunnel with a maximum velocity of 11m/s in the test area. The load changes within the blade structure for different wind speeds were measured using strain gauges as a function of flap length, location and deflection angle. The blade was based on the S833 airfoil and is 1.7 meters long, had a constant 178mm chord and a 6° pitch. The aerodynamic parts were 3D printed using plastic PC-ABS material. The total loading on the blade showed higher reduction when the flap was placed further away from the hub and when the flap angle (pitching towards suction side) was higher. The relationship between the load reduction and deflection angle was roughly linear as expected from theory. The effect on moment was greater than power production with a reduction in moment up to 30% for the maximum deflection angle compared to 6.5% reduction in power for the same angle. Overall, the experimental setup proved to be effective in measuring small changes in flapwise bending moment within the wind turbine blade.

Acknowledgements

Dedication

To my Family.

Table of Contents

viii

List of Figures

List of Tables

Nomenclature

α	Angle of attack $[deg]$
β	Location of a point along the blade span measured from the root $[m]$
η	Flap deflection angle $[deg]$
θ	Blade pitch angle $[deg]$
λ	Tip speed ratio $[-]$
λ_r	Local tip speed ratio $[-]$
μ	Fluid viscosity $[kg/ms]$
ν	Kinematic viscosity $[m^2/s]$
ρ	Fluid density $[kg/m^3]$
σ	Solidity $[-]$
σ_β	Mechanical Stress $[N/m^2]$
σ_r	Standard deviation of measurements
Φ	Coning angle $[deg]$
φ	Relative velocity angle $[deg]$
Ω	Rotor angular velocity $[rad/s]$
ω	Wind angular velocity $[m/s]$
A	Projected airfoil area $[m^2]$
A_c	Cross-sectional area $[m^2]$
a	Axial induction factor $[-]$
a'	Tangential induction factor $[-]$
a_c	Critical angle of attack (tip loss correction) $[deg]$
B	Number of blades $[-]$
b_r	Bias error

C_d	Drag coefficient $[-]$
C_l	Lift coefficient $[-]$
C_m	Airfoil pitching moment coefficient $[-]$
C_P	Power coefficient $[-]$
C_T	Thrust coefficient $[-]$
C_x	Axial force coefficient $[-]$
C_y	Tangential force coefficient $[-]$
c	Airfoil chord length $[m]$
D	Drag force $[N]$
E	Modulus of elasticity $[N/m^2]$
F	Prandtl's tip loss factor $[-]$
F_D	Blade element drag force $[N]$
F_L	Blade element lift force $[N]$
f_1	Fundamental natural frequency $[Hz]$
I_b	Area moment of inertia $[m^4]$
L	Lift force $[N]$
L_e	Effective length $[m]$
M	Airfoil pitching moment $[Nm]$
M_β	Bending moment at point β $[Nm]$
m	Mass $[kg]$
P	Rotor power $[W]$
p_r	Precision error $[\%]$
Q	Torque $[Nm]$
Re	Reynolds number $[-]$
r	Blade radius (span) $[m]$
U	Freestream wind velocity $[m/s]$
u_r	Total uncertainty $[\%]$
r_g	Radius of gyration $[m]$
T	Thrust force $[N]$
U_{rel}	Relative velocity $[m/s]$

Acronyms

2D	Two-dimensional
3D	Three-dimensional
BEM	Blade element theory
CSA	Canadian Standards Association
DBR	Dynamic brake resistor
HAWT	Horizontal axis wind turbine
NACA	National Advisory Committee for Aeronautics
NREL	National Renewable Energy Laboratory
NWTC	National Wind Technology Center
TEF	Trailing edge flaps
VFD	Variable frequency drive

Chapter 1

Background

1.1 Introduction

Wind mills traditionally converted wind power into a usable mechanical form that could provide torque for activities such as grinding and pumping. Wind turbines developed from wind mills with a similar purpose; to convert wind power into electrical power. The work on wind turbine development focuses on building more efficient and more economic wind turbines. This resulted in larger rotors being built and more sophisticated technologies being applied in operating modern wind turbines. One of the strategies to improve performance and life-span of wind turbines is active flow control. Active flow control involves the modification of the aerodynamic characteristics of a wind turbine blade by means of moveable aerodynamic control surfaces. The aerodynamic control surface can be the full blade, segments of it or smaller more distributed surfaces along the blade such as micro tabs and flaps [1]. Pitch control has become one of the traditional and widely used active flow control methods for wind turbines. It involves regulating the rotor performance and loads by pitching the full blade to change the relative angles with the flow. Recently, research has focused on blades that incorporate distributed and embedded intelligent systems of sensors and actuators instead of single control mechanisms. Such technology is referred to as 'smart blades' [2]. Active trailing edge flaps (TEFs) are one of the methods proposed in designing a smart blade. Flaps are relatively small movable control surfaces that directly modify the lift of a blade or airfoil section. The ultimate goal of the technology is to reduce the effect of freestream wind fluctuations on the blade load.

The idea to directly control lift on a blade using small movable surfaces was inspired by existing technology in aircraft and helicopters; from the contribution it made for these applications, it seems promising [1]. These movable surfaces can achieve significantly high changes in the lift coefficient of the sections they alter in response to their small deflections [3]. This is an effect of the increase or decrease of the camber of the airfoil of that section based on the side of deployment as shown in Figure 1.1. These distributed surfaces are usually operated by separate control mechanisms (sensors and actuators) which have several advantages compared to traditional full blade pitch systems. They have better structural and safety features and require less power for activation since they have significantly lower surface inertia than full span pitch control, mainly due to their size [1]. Lower surface inertia is also pivotal to enable high frequency control which is required to respond to smaller more frequent wind fluctuations.

1
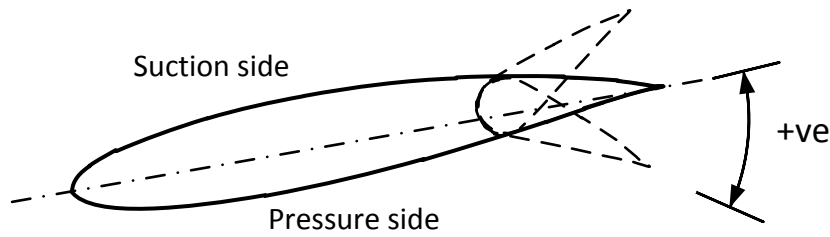
Figure 1.1 Illustration of a hinged trailing edge flap on an S833 airfoil.

1.2 Project Motivation

Power generation through wind energy is one of the fastest developing renewable energy technologies [4]. As developers compete towards building more cost-effective and efficient wind turbines, several challenges arise that require new strategies and innovations to overcome [5]. The size of a wind turbine is proportional to its economic advantage on the long term. The size of current and work-in-progress wind turbines is quickly increasing, as shown in Figure 1.2. One of the main challenges facing the continually increasing size of wind turbine blades is the fluctuating loads caused by the natural conditions in which they operate. The ability to alleviate such loads would allow us to reduce the weight, and increase the size and life-span of blades. Wind turbines are subject to extreme fatigue load cycles due to the highly fluctuating nature of the wind resource. Hence, most wind turbine components' design are governed by fatigue instead of ultimate loads [6].
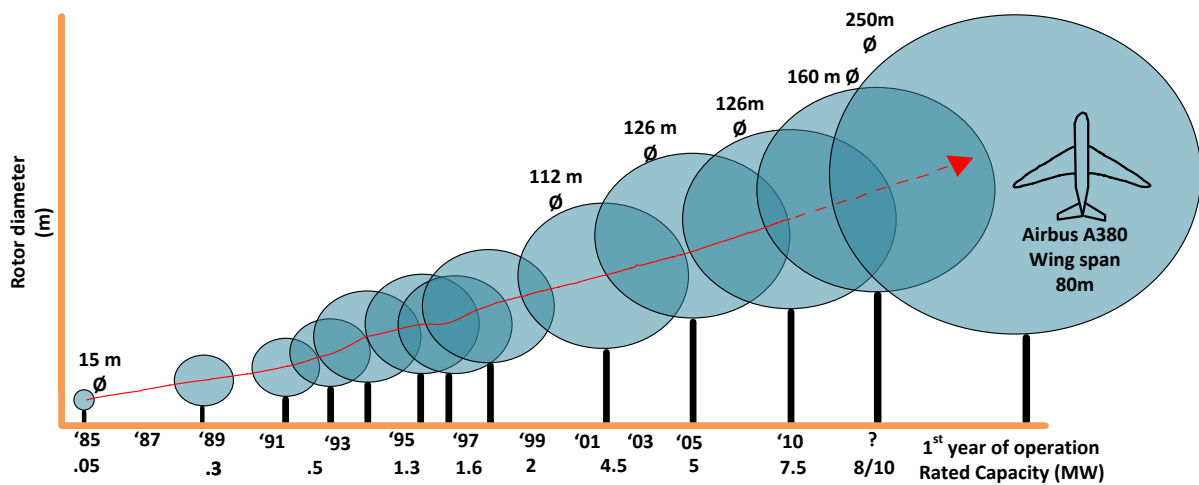
Figure 1.2 Wind Turbine diameter size development. Adapted from [5].

2

Active flow control is one of the methods that can alleviate fatigue load in order to enable larger wind turbines to use lighter and less material in their blade design and increase the operational-life expectancy of the rotor and other wind turbine components. Pitch control is one of the traditional and widely used active flow control methods for large wind turbines. Pitch control has proved to significantly reduce fatigue load increments due to relatively low frequency variations on the blade conditions caused by yaw error, wind shear and gusts [7]. Larsen et al. [8] showed that individual pitch can reduce fatigue loads by 25% and the maximum load on the turbine by 6% when measuring bending moment at the hub. As wind turbines become larger, however, their blades become heavier and more flexible. This adds more stress on pitch bearings and increases the response time between the stimulating input and actuation of the active system.

Smaller more distributed control devices can achieve faster response times and require smaller embedded components. Several computational simulations were carried out by researchers that assessed the ability of such devices to alleviate load and regulate power as an alternative to full blade pitch systems. The studies yielded consistently promising but varying results. The differences were usually attributed to different operating conditions and controller design approaches. In addition, scarce but also promising experimental studies were carried out to validate the flow control potential of such devices. The computational and experimental studies and their results are discussed in the following Literature review chapter.

Development of the proposed method will allow developers to build larger wind turbines and more economic versions of the current sizes in the market, which will positively contribute to further integration of wind power generation in the global energy system.

1.3 Thesis objectives and outline

The potential of flow control using aerodynamic control devices is strongly supported through modelling and limited experiments. Upon the review of related studies, it was found that there was significantly more work done on computational simulations and numerical modelling with solemn experimental validation. The potential contribution of an experimental platform that can investigate the effects of aerodynamic control devices in controlled operating conditions was evident.

The first objective of this thesis is to develop an instrumented wind turbine test rig and rotor to enable a wide-range of experimental set-ups for investigations focusing on TEFs. The second objective is to demonstrate the capability of the developed systems through a steady state study of the effect of TEFs on blade load and power production. This study sets a foundation for solid contributions towards experimental work using operational rotating wind turbines in controlled and realistic conditions.

This thesis covers three main phases. First, the design and building of a wind turbine test rig. Second, the aerodynamic and structural design and fabrication of a modular customizable blade. Third, an experimental study of the effect of TEFs on blade load and power production carried out using the developed test rig and blade. The thesis is organized into seven chapters, starting with this introduction and followed by:

- **Chapter 2 Literature Review:** Provides an outline of the concepts, terminology and theories that apply to the investigation and an overview of related work in the field.

- **Chapter 3 Wind Turbine Test Rig:** Discusses the design requirements and constraints of the wind turbine test rig, the design methodology and outcome, and the manufacturing and assembly of the wind turbine test rig.

- **Chapter 4 Modular 3D Printed Blade:** Discusses the aerodynamic and structural design requirements, the design process and outcome, and the fabrication and assembly of the rotor.

- **Chapter 5 Experimental Procedure:** Describes the facility and measurement equipment, the experimental setup, and calculations related to the TEF investigation.

- **Chapter 6 Results and Discussion:** Presents an overview and a discussion of the results of the experimental investigation.

- **Chapter 7 Conclusion:** Provides an assessment of the developed wind turbine test rig and rotor in light of the study objectives, outlines the conclusions from the findings of the experiment performed, and recommendations for continuation of future studies.

Chapter 2

Literature Review

2.1 Theory

2.1.1 Wind turbine overview

The most common modern design for wind turbines is the horizontal axis wind turbine (HAWT) [9]. A HAWT is aligned such that the axis of rotation of the wind turbine blade, also known as the rotor, is parallel to the ground, in normal operating conditions it will also be parallel to the direction of the oncoming freestream wind. The main subsystems of a HAWT, shown in Figure 2.1, are listed below:

- *Rotor.* The rotor is the main rotating subsystem of the wind turbine and it consists of the blades and hub. It is the most important component of a wind turbine from a performance and cost point of view. The rotor blades are the most critical elements in determining the amount of energy captured by the wind turbine. A rotor typically accounts for more than 25% of the full cost of a wind turbine system [10].

- *Nacelle and yaw system.* The nacelle includes the drive-train and energy conversion systems of the wind turbine. Typically consisting of a motor/generator, gearbox, drive shaft and bearing and is supported by the main frame. The yaw system allows the nacelle to rotate around a vertical axis.

- *Tower and foundation.* The tower provides structural support to the wind turbine systems and places them at the required height from the ground. Steel tubes, lattice structures and cement towers are typical for modern wind turbines.

- *Balance of electrical systems.* These include electrical components other than the motor/generator such as transformers, power correction capacitors, power electronic converters, cables, switchgears, etc.
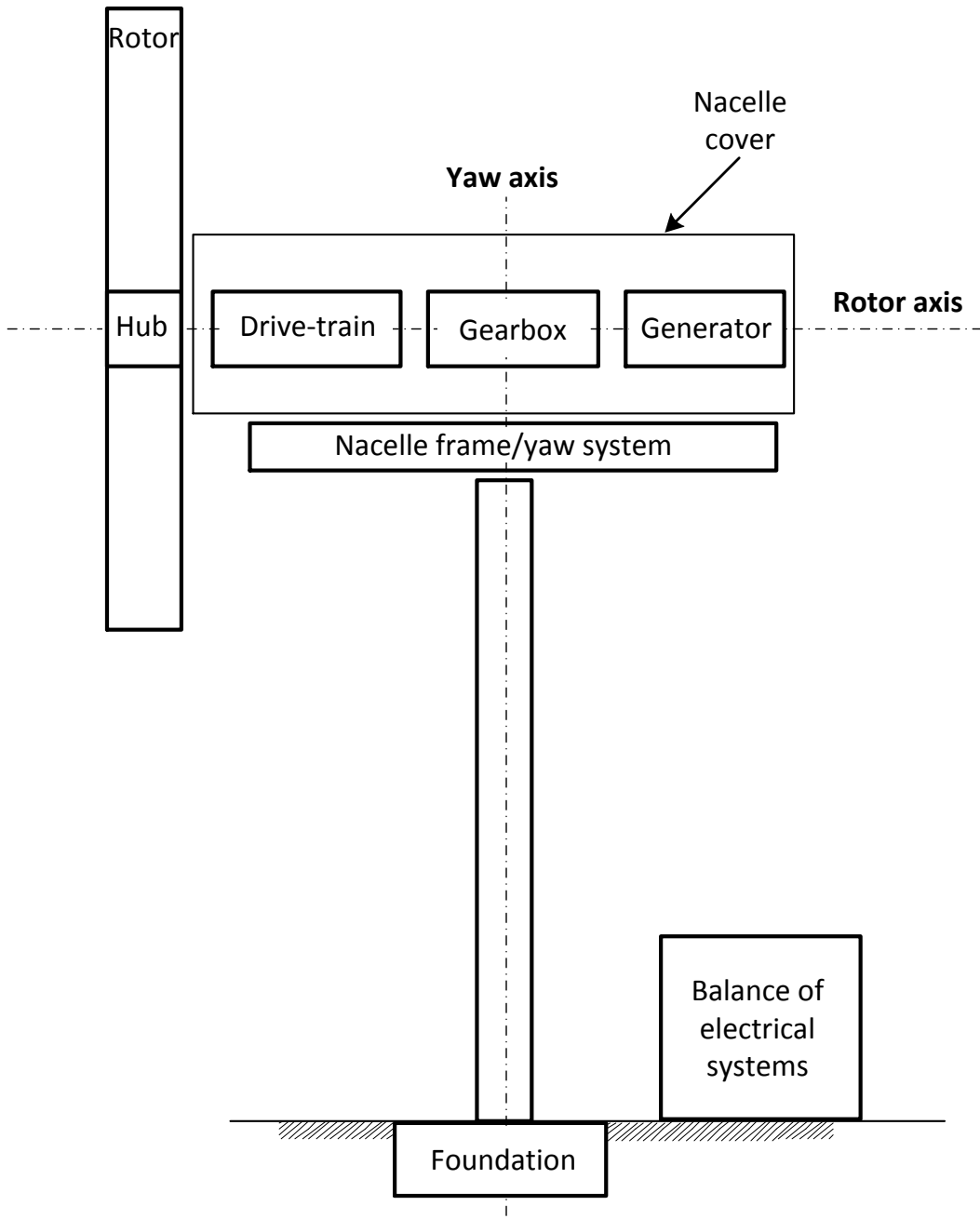
Figure 2.1 Main wind turbine components.

2.1.2 Airfoil concepts and terminology

Airfoils are structures with specific cross-sectional geometries that generate mechanical forces from the relative motion between the structure and the surrounding fluid. Wind turbines use airfoils to generate torque that drives the generator to produce power. The airfoil properties including the shape, length and width are determined based on the required aerodynamic performance.

2.1.2.1 Geometry of an airfoil

Figure 2.2 shows the common items that are used to characterize an airfoil. The mean camber line is the line that passes the mid-points between the top and bottom surfaces. Camber is a measure of the curvature of airfoil. The chord line is a straight line between the leading and trailing edges. If the chord line and camber line are the same, the airfoil is symmetric. The angle of attack, α, is the angle between relative velocity of the fluid moving around the airfoil and its chord line. The mechanical forces generated by the movement of the airfoil are dependent on the angle of attack.
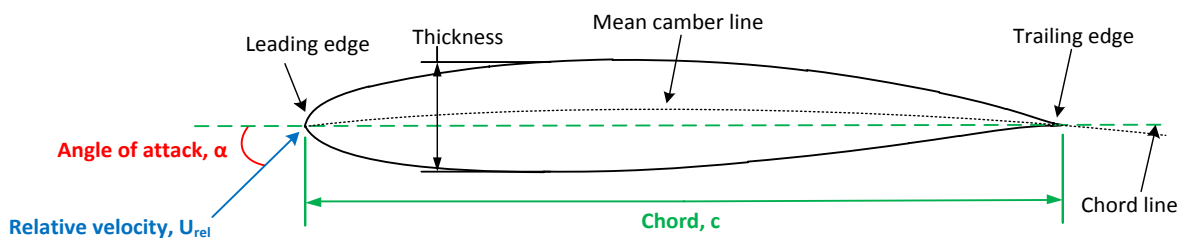
Figure 2.2 Airfoil nomenclature.

2.1.2.2 Forces on an airfoil

The flow velocity on the convex side of the airfoil increases and the pressure decreases making it the 'suction' side of the airfoil. The opposite happens on the concave side which is called the 'pressure' side. The flow along the surface also creates drag due to viscous friction and pressure distribution. These two phenomena create a distribution of forces on the surface of the airfoil that are resolved in two main directions, the lift force and drag force, and a moment, the pitching moment. The forces are resolved at the aerodynamic center, which is the point where the pitching moment does not vary with the angle of attack [11]. For symmetric airfoils, the aerodynamic center lies exactly at the quarter-chord from the leading edge, however, it is still used as an approximation for cambered airfoils [11]. Figure 2.3 shows an illustration of the resultant airfoil forces.

- *Lift force* is the resultant perpendicular force to the angle of attack and is caused by the pressure imbalance on both sides of the airfoil that are parallel to the flow.

- *Drag force* is the resultant force parallel to the direction of the flow and is caused by both viscous friction and the pressure imbalance.

7

- *Pitching moment* is a moment caused by the pressure distribution on the airfoil surface that acts about an axis perpendicular to the airfoil cross-section.
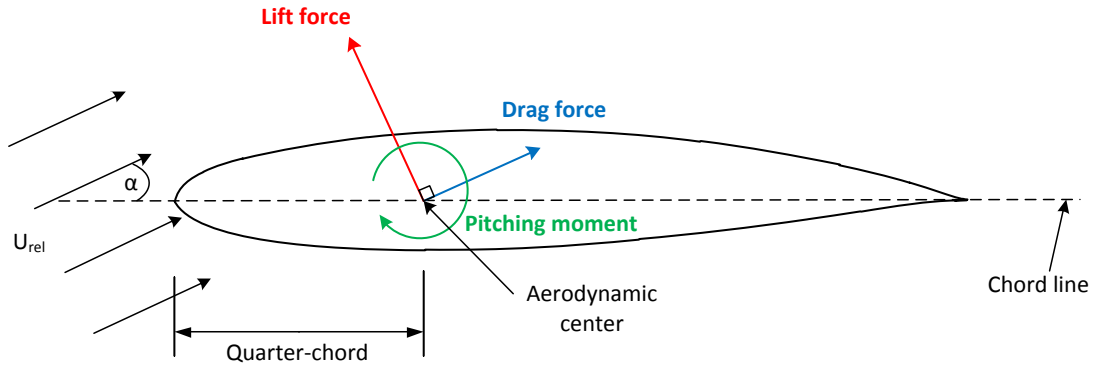
Figure 2.3 Airfoil forces.

An important non-dimensional parameter used to characterize fluid flow is the Reynolds number, Re. the Reynolds number is the ratio between inertial and viscous forces in a fluid and is defined for airfoils by:

$$Re = \frac{Uc}{\nu} = \frac{\rho U c}{\mu} = \frac{Inertial\ force}{Viscous\ force}$$

2.1

where U is the fluid velocity, c is the chord length of the airfoil, ρ is the fluid density, ν is the kinematic viscosity and μ is the fluid viscosity. Rotor design uses non-dimensional coefficients for the forces and moments of a two-dimensional airfoil [9]. The values of these coefficients are determined from wind tunnel tests as a function of the Reynolds number and angle of attack. They are defined as follows [9]:

The lift coefficient:

$$C_l = \frac{L}{\frac{1}{2}\rho U^2 c} = \frac{Lift\ force/unit\ length}{Dynamic\ force/unit\ length}$$

2.2

The drag coefficient:

$$C_d = \frac{D}{\frac{1}{2}\rho U^2 c} = \frac{Lift\ force/unit\ length}{Dynamic\ force/unit\ length}$$

2.3

8

The moment coefficient:

$$C_m = \frac{M}{\frac{1}{2}\rho U^2 A c} = \frac{Pitching\ moment}{Dynamic\ moment} \qquad\qquad 2.4$$

where A is the projected airfoil area, c is the chord and U is the freestream fluid velocity. M is the pitching moment, while L and D are the lift and drag forces per unit length of the span of the airfoil into the page. The two-dimensional coefficients are based on the assumption that the airfoil span is infinite and the experiments are designed to measure them such that edge effects are negligible [9].

The slope of the linear part of a typical C_l curve for airfoils, shown in Figure 2.4, is approximately equal to $2\pi/rad$ according to thin airfoil theory [3], however, when a critical α is reached C_l decreases in a manner that strictly depends on the airfoil geometry [11]. This is known as the stall point. Stall is a phenomenon where the boundary layer separates from the upper (suction side) of the airfoil causing a rapid drop in the lift force.

Thin airfoil theory applies the concepts of circulation, streamlines and pressure distribution around a transformed shape to predict the airfoil characteristics. It assumes that the airfoil thickness is small compared to the chord length and only applies to small α [12]. The theory provides a useful understanding of the relationship between C_l, α and the airfoil geometry, however, since it breaks down for thicker airfoils and higher α that violate its assumptions, in practice the values are usually obtained from numerical and computational studies and wind tunnel experiments [12] for all aerodynamic design applications.
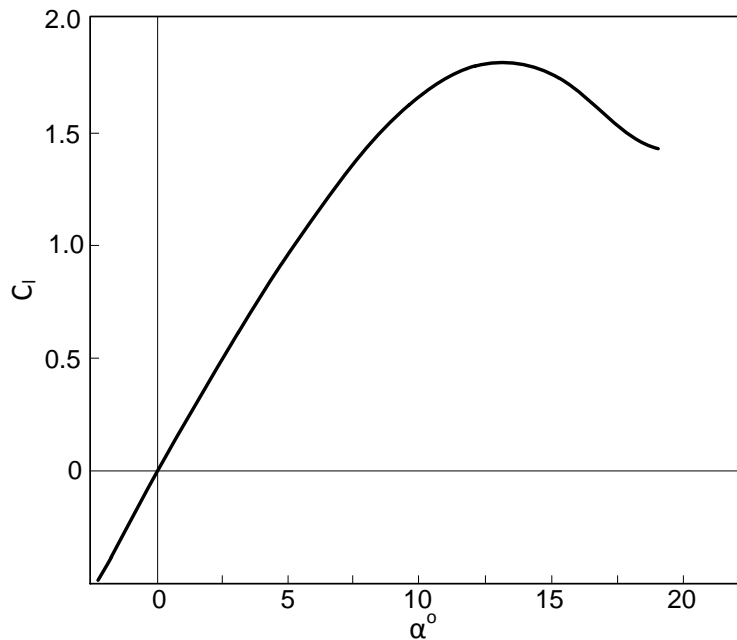
Figure 2.4 Typical C_l vs. α.

Three-dimensional effects

A rotor blade in reality is made up of a finite series of airfoils. This creates a finite beam with a pressure difference between the upper and lower surfaces that generates lift. Flow leakage occurring at the tips cause the streamlines at the upper and lower surfaces to deflect on opposite sides and a discontinuity is seen in the tangential velocity at the trailing edge [13]. This jump creates trailing vortices due to the continuous stream-wise vortices in the wake. The result of these effects is that the actual lift of the three-dimensional blade is reduced compared to the two-dimensional airfoil at the same α and Re, and the lift has a component parallel to the direction of the flow, called the induced drag [13].

2.1.3 Aerodynamics of HAWTs

A HAWT extracts mechanical energy from a stream of moving air by means of a rotating disc-like converter [14]. Assuming only the mass of air going through the disc is affected and a portion of its kinetic energy is extracted, the mass of air slows down. A boundary surface can then be imagined separating the affected mass going through the disk-like converter. By extending the boundary upstream and downstream a long stream-tube of circular cross-section is formed [6]. Since no air flows across the boundary, the mass flow of the air remains the same through the length of the stream-tube. The cross-sectional area of the stream-tube will vary with the speed of the mass of air according to continuity.

2.1.3.1 Betz momentum theory

Betz's momentum theory is based on the modelling of a two-dimensional flow through the converter disk described above, called the 'actuator disk' [14]. The model analysis assumes a control volume whose boundaries are the stream tube boundary and two cross-sections upstream and downstream of the rotor plane, as shown in Figure 2.5. The flow passes through the cross sections only. The actuator disk creates a discontinuity in the pressure of the stream flowing through it and represents the power absorbed by the wind turbine [6]. This model makes the following assumptions [9]:

- Incompressible steady state flow,
- No frictional drag,
- Infinite number of blades,
- Uniform thrust per unit area,
- No wake-rotation,
- Far upstream and far downstream static pressures are equal to the ambient undisturbed pressure.
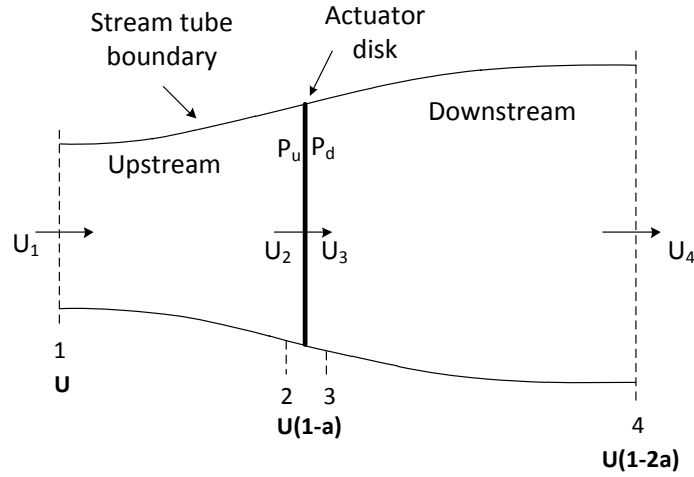
Figure 2.5 Actuator disk model of a wind turbine.

The influence of the wind turbine on the flow velocity is represented by the axial induction factor (or the retardation factor) *a* [15]. The axial induction factor represents the fraction of velocity decrease such that:

$$U_2 = U_3 = U(1 - a) \qquad\qquad 2.5$$

$$U_4 = U(1 - 2a) \qquad\qquad 2.6$$

where U_2 and U_3 are the velocities at the actuator disk, U_4 is the velocity downstream and U is the freestream velocity as shown in Figure 2.5. Applying linear conservation to the control volume, the net force of the system can be found. This net force is equal and opposite to the thrust force T which is the axial force on the wind turbine [9]. Applying Bernoulli's Equation between the freestream and upstream side of the actuator disk and again between the upstream and downstream sides, it can be shown that [15] :

$$T = \frac{1}{2}\rho A U^2 [4a(1 - a)] \qquad\qquad 2.7$$

where A is the area of the actuator or rotor disk and ρ is the fluid density. Thrust is characterized by a non-dimensional thrust coefficient:

$$C_T = \frac{T}{\frac{1}{2}\rho U^2 A} = \frac{Thrust\ force}{Dynamic\ force} \qquad\qquad 2.8$$

$$C_T = 4a(1 - a) \qquad\qquad 2.9$$

where C_T is the coefficient of thrust. The power extracted at the disc P is related to the momentum change and it is equal to the thrust times the velocity at the disc. Applying the first law of thermodynamics it can be shown that [15]:

$$P = \frac{1}{2}\rho A U^3 [4a(1 - a)^2] \qquad\qquad 2.10$$

Similarly, the coefficient of power that characterizes this rotor disk is equal to:

$$C_P = \frac{P}{\frac{1}{2}\rho U^3 A} = \frac{Rotor\ Power}{Power\ in\ wind} \qquad\qquad 2.11$$

$$C_P = 4a(1 - a)^2 \qquad\qquad 2.12$$

where C_P is the coefficient of power. Equation 2.11 has a maximum at $a = 1/3$. The maximum possible theoretical C_P known as the Betz limit becomes:

$$C_{P,max} = \frac{16}{27} \approx 0.593 \qquad\qquad 2.13$$

An important conclusion of this is the maximum theoretical power that can be extracted by a rotor, which is a function of the rotor area A and freestream velocity U only such that:

$$P_{max} = \frac{1}{2}\rho A U^3 \frac{16}{27} \qquad\qquad 2.14$$

2.1.3.2 Angular momentum and wake rotation

In reality, a rotating blade will additionally impose a spin to the flow in the rotor wake. To conserve angular momentum, this spin is equal to the torque of the rotor [14]. The Betz momentum theory can be expanded to include these effects and can be called the general momentum theory. Note that all other assumptions from Betz theory still apply. An annular stream tube with a radius r and a thickness dr is applied to the actuator disk model, as shown in Figure 2.6. the area of the control volume cross-section becomes $2\pi r dr$ [9].
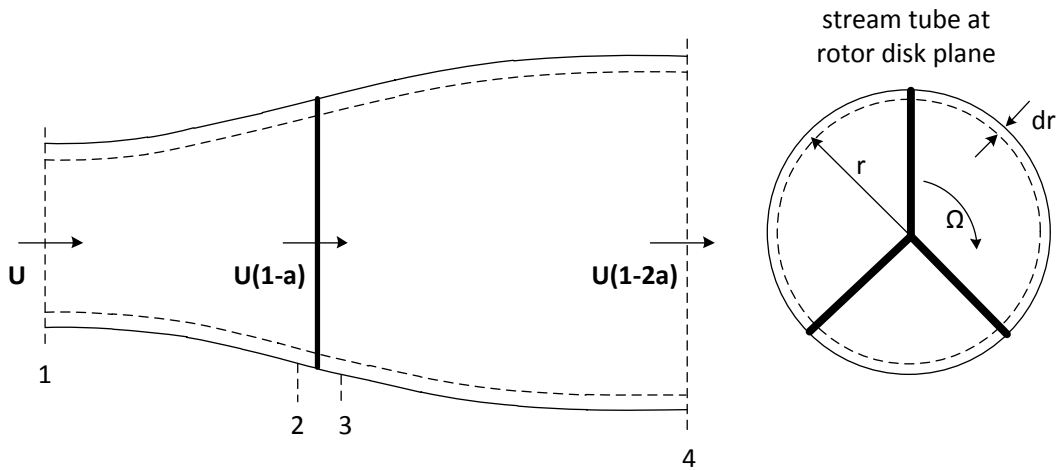
Figure 2.6 Annular control volume.

The angular velocity imparted on the flow ω is assumed to be small compared to the angular velocity of the rotor Ω such that the pressure in the far wake is equal to the pressure in the freestream. The tangential induction factor a' is a measure of the impact of the rotor rotation on the fluid.

$$a' = \omega/2\Omega \qquad\qquad 2.15$$

In addition to the axial component, $U(1 - a)$, the total induced velocity at the rotor now has a component in the angular plane $r\Omega a'$. The tip speed ratio λ is defined as the ration between the blade tip speed and the freestream velocity. At the tip:

$$\lambda = \Omega R/U \qquad\qquad 2.16$$

At the control volume radius:

$$\lambda_r = \Omega r/U \qquad\qquad 2.17$$

where λ_r is the local tip speed ratio.

By applying conservation of linear momentum, the differential contribution to thrust T can be expressed as:

$$dT = [4a(1 - a)]\rho U^2 \pi r dr \qquad\qquad 2.18$$

Similarly by applying conservation of angular momentum the differential contribution to torque Q can be expressed as:

$$dQ = [4a'(1-a)]\rho U \pi r^3 dr \qquad \qquad 2.19$$

The power generated by each element is equal to the differential torque dQ multiplied by the angular rotation of the rotor. Using the definition of the local speed ration in equation 2.17 the differential power contribution by each segment can be expressed as:

$$dP = \left[\frac{4}{\lambda^2}a'(1-a)\lambda_r^3 d\lambda_r\right]\rho A U^3 \qquad \qquad 2.20$$

The momentum theory provides an understanding of the flow field and relates it to thrust and power production of the rotor through the flow induction parameters a and a'. However, it fails to link the rotor performance to the rotor geometry [15].

2.1.3.3 Blade element theory

The blade element theory determines the forces on the rotor solely by the lift and drag characteristics of the airfoil. The blade is divided into a finite number of segments (or elements) for the analysis [9]. The lift and drag forces in an airfoil is a function of its geometry and the relative velocity of the fluid surrounding it as discussed earlier in section 2.1.2. For a rotating blade, the relative velocity is the resultant of both the angular and axial velocity as show in Figure 2.7. The blade segment is pitched at an angle θ. The angle of the U_{rel} vector is φ. U_{rel} can be compared to its counter-part in Figure 2.3 for the lift and drag force directions.
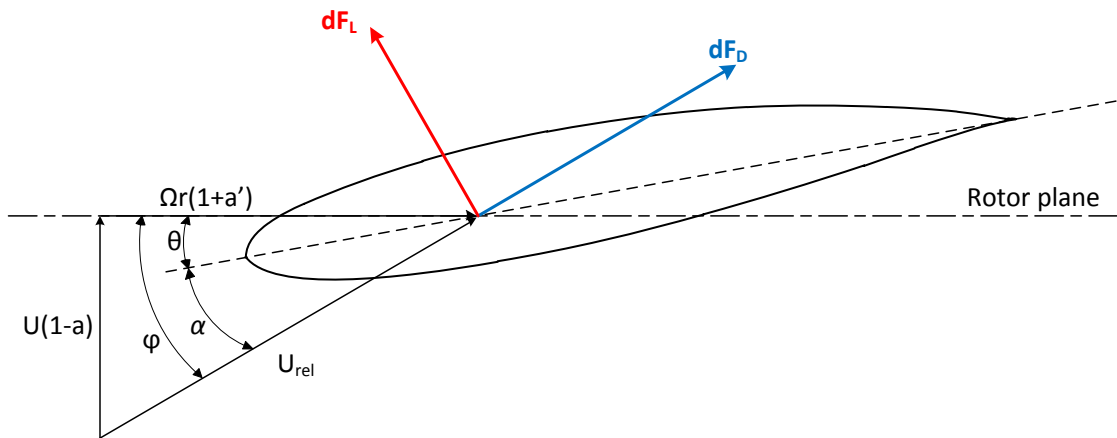
Figure 2.7 Blade element velocities.

14

The angle of attack of the segment is:

$$\alpha = \varphi - \theta \qquad 2.21$$

The principle blade element theory assumption is that the forces acting on the blade segment are identical to the forces on a two-dimensional airfoil with the same geometry. The pitch angle θ is modified along the blade to acquire α that has the desired C_l and C_d values based on known sets of data from wind tunnel experiments as discussed in section 2.1.2. The following relations can also be deduced from Figure 2.7:

$$\tan \varphi = \frac{U(1-a)}{\Omega r(1+a')} \qquad 2.22$$

$$U_{rel} = \frac{U(1-a)}{\sin \varphi} \qquad 2.23$$

The differential contribution to lift and drag can be acquired for each blade segment by the resolving the lift and drag forces based on the airfoil data into the thrust and torque directions, as shown in Figure 2.8.
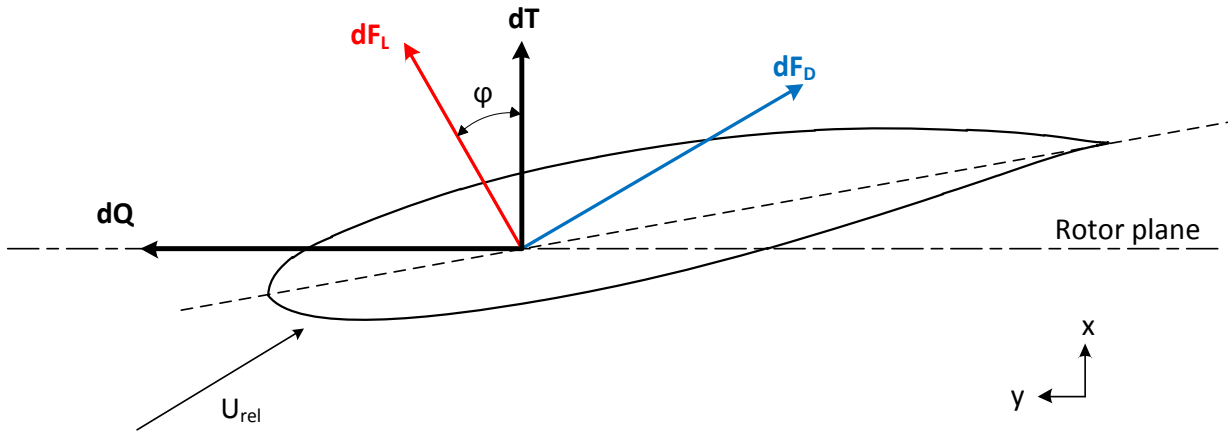
Figure 2.8 Blade element forces.

The axial thrust on the blade segment becomes [6]:

$$dT = \frac{1}{2}\rho U_{rel}^2 Bc(C_l \cos \varphi + C_d \sin \varphi)dr \qquad 2.24$$

15

where dr is the segment thickness, B is the number of blades and c is the cord length. The torque on the blade segment becomes [6]:

$$dQ = \frac{1}{2}\rho U_{rel}^2 Bcr(C_l \sin \varphi - C_d \cos \varphi)dr \qquad 2.25$$

An important conclusion is that an increase in C_l leads to an increase in both the torque and the thrust, while an increase of C_d leads to a decrease in torque but an increase thrust. The blade element theory provides a definition for the thrust and torque of a blade segment as a function of the flow angles and blade characteristics. Noting that the blade segment in a rotating frame is a representation of the control volume used in the momentum theory (as in Figure 2.6), the two theories are combined to be used to design the ideal blade shape or to analyze the performance of a blade with any arbitrary shape [9].

2.1.3.4 Blade element momentum (BEM) theory

The BEM theory couples the momentum theory with local effects at the actual blades represented by the blade element theory. In this method the influence of the flow field on the aerodynamic response of the blade segments is analyzed. The BEM model is capable of calculating the steady loads, torque and power, for different settings of freestream velocity, angular blade velocity and pitch angles [13], while accounting for the finite number of blades and their airfoil characteristics along their radius. This is achieved by equating the force relationships concluded from the momentum theory, equations 2.18 and 2.19 with the force relations concluded from the blade element theory, equations 2.24 and 2.25. This produces a relationship between the induction factors, a and a', and the blade characteristics for the given flow, C_l and C_d. The relationships are applied at the radius of the control volume at each segment:

$$a = \frac{1}{\frac{4 \sin^2 \varphi}{\sigma C_x} + 1} \qquad 2.26$$

and

$$a' = \frac{1}{\frac{4 \sin \varphi \cos \varphi}{\sigma C_y} - 1} \qquad 2.27$$

where σ is defined as the solidity at radius r. Solidity accounts for the finite number of blades.

$$\sigma = \frac{cB}{2\pi r} \qquad 2.28$$

C_x and C_y are the resolutions of the C_l and C_d in the direction of the axial and tangential force as shown in Figure 2.8, so that:

$$C_x = C_l \cos \varphi + C_d \sin \varphi \qquad \text{2.29}$$

$$C_y = C_l \sin \varphi - C_d \cos \varphi \qquad \text{2.30}$$

In designing an optimized rotor for specified flow conditions, a BEM algorithm solves these equations iteratively for each radial segment of the control volume to achieve the ideal values of a and a'. For analyzing a known rotor for a range of flow conditions, freestream wind speeds for example, a sweep of the iterative process is performed on discrete values of the entire range to predict the performance curves of the rotor. Details of the iteration steps can be found in [13].

The overall coefficient of power and coefficient of torque, C_P and C_T, are the standard parameters that are used to characterize and compare different rotor performance [6]. Using the values of a and a' from the BEM algorithm output, C_P and C_T can be calculated by integrating the power and torque contributions from each blade segment [15].

$$C_P = \frac{\int_0^R \Omega dQ}{\frac{1}{2} \rho \pi R^2 U^3} \qquad \text{2.31}$$

$$C_T = \frac{\int_0^R dT}{\frac{1}{2} \rho \pi R^2 U^2} \qquad \text{2.32}$$

where R is the rotor radius. Figure 2.7 shows an example of a C_T and C_P curve for an ideal rotor.

17
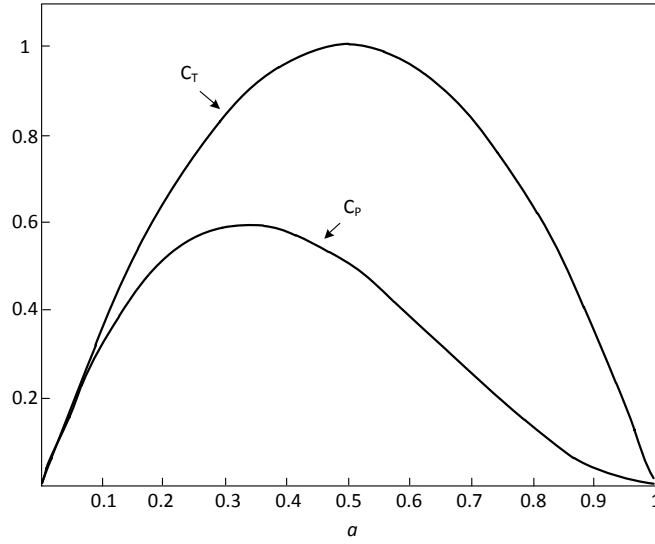
Figure 2.9 C_P and C_T for an ideal HAWT vs. axial induction factor a [13].

2.1.3.5 Limitations and corrections

The BEM model is agreed to be a suitable for the design and analysis of a modern HAWT [6], [9]. However, the design has limitations and several corrections have been suggested to improve its accuracy. Two important effects that must be accounted for are tip losses and high values of the axial induction factor.

Prandtl's tip loss factor. For a rotor with finite blades the vortices produced in the wake are different from those produced by a rotor with a finite number of blades. Prandtl's tip loss factor accounts for the assumption of infinite number of blades made by the momentum theory. A correction factor derived by Prandtl is applied to the differential force equations of the momentum theory such [13]:

$$dT = [4a(1-a)]\rho U^2 \pi r F dr \qquad \text{2.33}$$

and

$$dQ = [4a'(1-a)]\rho U \pi r^3 F dr \qquad \text{2.34}$$

where F is the the tip loss factor and is computed as follows [9]:

$$F = \left(\frac{2}{\pi}\right) \cos^{-1} \left[\exp\left(-\left\{ \frac{(B/2)[1-(r/R)]}{(r/R)\sin\varphi} \right\} \right) \right] \qquad \text{2.35}$$

18

F varies with φ and is unique to the flow conditions. Equations 2.18 and 2.19 should be replaced by 2.33 and 2.34 in the execution of the BEM algorithm, and a step for the calculation of F should be added.

Glauert correction. The general momentum theory breaks down at a critical value of $a{=}0.4$, known as a_c. An empirical relationship between C_T and a has been made to fit with measurements and is used for high induction values [13]:

$$C_T = \begin{cases} 4a(1-a)F, & a < a_c \\ 4(a_c^2 + (1-2a_c)a)F, & a \geq a_c \end{cases} \qquad 2.36$$

where F is the tip loss factor. By equating to the differential thrust equation on an annular segment, the axial induction factor for $a > a_c$ becomes [13]:

$$a = \frac{1}{2}\left[2 + K(1-2a_c) - \sqrt{(K(1-2a_c)+2)^2 + 4(Ka_c^2 - 1)}\right] \qquad 2.37$$

where:

$$K = \frac{4F sin^2 \varphi}{\sigma C_x} \qquad 2.38$$

In order to compute the velocities correctly for cases where $a > a_c$ equation 2.37 should replace equation 2.26 in the BEM algorithm.

2.1.3.6 PROPID Design code

PROPID [16] is a computer program code based on a multipoint inverse design method [17] for the design and analysis of horizontal axis wind turbines [18]. PROPID uses the PROPSH BEM code [19], which is an updated version of the PROP code [20], for its analysis. The codes are based on the BEM equations and algorithm discussed in the previous sections. PROPID allows the user to specify different BEM correction models from the theory to be applied in the analysis. Table 2.1 shows some of the models that can be activated during analysis.

The strength of the code is its inverse design capability. Inverse design allows the specification of the required design operating conditions and the iterative algorithm is used to modify the input parameters (geometric blade characteristics) to achieve the required performance. The number of input parameters the user allows the program to change should be equal to the number of performance characteristics specified. For example, if the program is required to achieve peak C_p at a specific rotation speed and wind speed, it can optimize the blade pitch and chord length. PROPID also allows for the specification of distributions to be used as optimization targets, as long as another equal number of distributions are determined by the

code. For example, the required axial induction distribution at the design point can be specified as a target, and the code is left to optimize the blade twist and chord length for each segment [18]. In contrast, PROPID is also capable of analyzing the off-design aerodynamic capabilities of a rotor with fully specified geometry (chord, twist and airfoil distributions and blade number) to predict the rotor performance in different operating conditions. Table 2.1 shows the basic user input for the analysis case. In the design case, some of the input parameters are left for the code to optimize, details can be found in [18].

Category	Parameter	Setting
Operating conditions	Wind speed	float
	Rotation speed	float
	Blade pitch	float
Input Parameters	Blade length	float
	Hub height	float
	Number of blades	integer
	Hub cutout	float
	Chord and twist	distribution
	Airfoil	distribution
	Rotor cone angle	float
Aerodynamic Models	Tip loss model	On/off
	Hub loss model	On/off
	Brake state model	On/off
	Viterna stall model	On/off
	Wake Swirl	On/off

Table 2.1 PROPID primary user specified parameters for analysis case [18].

The aerodynamic models are based on empirical equations from the different corrections to the BEM algorithm. The tip and hub loss models are based on Prandtl's corrections discussed in the previous section. The brake state model applies a modified version of the Glauert correction for high induction factors. The Viterna stall model applies an approximation to the aerodynamic characteristics of the airfoil when calculating the post-stall performance of the rotor. The wake swirl model is a correction that accounts for the angular momentum.

Typical output parameters from a PROPID wind sweep analysis are shown in Table 2.2. For a detailed and complete list of output parameters and their organization see [18].

Category	Parameter	Range
Aerodynamics	C_l distribution	Radial position
	C_d distribution	Radial position
	α distribution	Radial position
Performance	Rotor power	Wind speed
	C_P	Tip speed ratio
	Thrust	Wind Speed

Table 2.2 PROPID analysis output.

2.1.4 Wind Turbine Loads

Wind turbine loads are forces or moments that act upon the wind turbine. The loads are predominantly dependent on the interaction between the rotor and the wind. In designing the rotor, although it is helpful to maximize the loads that operate the rotor for extraction of useful energy, this also increases the stresses that the wind turbine components must endure. Due to the varying nature of the wind, the stresses on the wind turbine components can be highly dynamic. The structural design of wind turbine components should satisfy two major requirements. First, they should be able to withstand the extreme expected loads. Second, they should be designed such that the fatigue life of their components is guaranteed for their service life which is typically between 20 and 30 years [14]. Accounting for fatigue is especially important since fatigue loading on wind turbine blades is the major factor that contributes towards structural failure [6]. Different loads can be categorized according to their temporal effect on the rotating rotor, as shown in Figure 2.10.

- *Steady loads.* Steady loads are those that do not vary over long periods of time. Steady loads can be an effect of interaction of wind with static or rotating components of the wind turbine.

- *Cyclic loads.* Unsteady loads that vary with a regular pattern over time, or are periodic in nature are called cyclic loads. They can be a result of wind shear, gravity or off-wind yaw motion.

- *Non-cyclic loads.* Loads that are transient in nature and vary with time over relatively short periods without following a specific pattern are called non-cyclic loads. Examples of such loads are the stochastic loads that are caused by wind turbulence and sudden inertial loads caused by the rotor when it is accelerating for start-up or decelerating upon applying brakes.
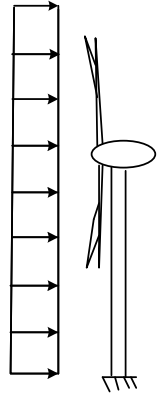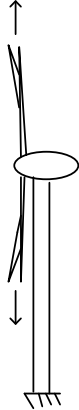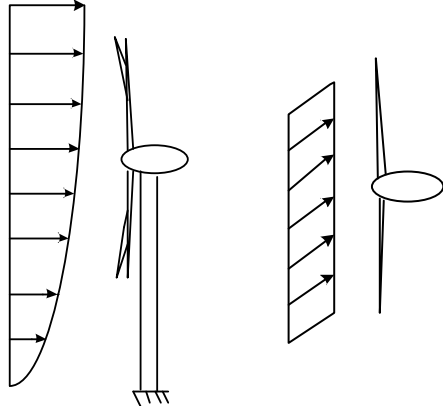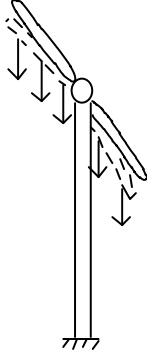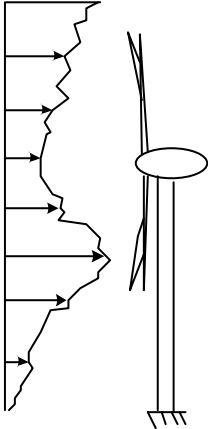
		Aerodynamic forces		Inertial and gravity forces
Steady loads		Steady mean wind speed		Centrifugal forces
Unsteady loads	Cyclic loads	Vertical wind shear	Cross wind (yaw)	Gravity forces
	Non-cyclic loads	Wind turbulence		

Figure 2.10 Aerodynamic, gravitational and inertial loads that affect a HAWT blade. Adapted from [14].

The sources of each of the loads in each of these categories can be aerodynamic or inertial. Aerodynamic loads are the product of the interaction between the rotor and wind. Since the loads are responsible for power generation and structural stresses, controlling aerodynamic loads can be very beneficial in improving the performance of the wind turbine rotor or limiting transformation of freestream wind effects into load changes within the blade structure. As discussed in previous sections (see equations 2.24-2.27), it is evident that C_l is the major factor in determining the differential torque and thrust contribution of the series of blade segments that make the full blade. Although the blade geometry, thus the distribution of C_l, is optimized for the peak performance at the design conditions, off-design performance could be improved by modifying the aerodynamic properties. There are several ways of controlling the aerodynamics loads that all depend on the modification of the aerodynamic performance of a blade, they all rely on modifying C_l of the full blade or different blade segments. Since C_l is a result of the blade geometry and a function of α it can be modified either by changing α, by pitching the blade segment or changing the rotation speed (see Figure 2.7), or by changing the geometry of the blade segment.

2.1.5 Aerodynamic load distribution on HAWT blades

The aerodynamic load distribution over the span of a HAWT wind turbine blade is the result of the collective contribution to the blade loads by the series of airfoils that form the blade geometry. The result of the integration of the differential torque (equations 2.24) is the tangential load distribution which creates a power-producing moment on the blade in the edgewise (in-plane) direction. Gravitational forces on the blades are cyclic loads that also contribute to the edgewise moment. The integration of the differential thrust (equation 2.25) produces the axial force distribution which acts in the flapwise (out-of-plane) direction. The flapwise bending moment resulting from the axial forces is of considerably more significance on the blade strength and will be discussed in more detail. Figure 2.11 shows the lift and drag forces on an airfoil section and the result of their integration along the blade length, it also shows the coordinates and terms used for identifying the load directions.

The distribution profile for the axial and tangential force distributions for different wind speeds can vary distinctly for a blade with local twist angles and different airfoils along its span. This is related to the airfoil characteristics. Although they vary uniformly with α in the normal range of operation, a change in the airfoil geometry or twist angle can cause a change in local load contributions. The twist is optimized for the design wind speed for a load distribution to be as close to the theoretical maximum as possible. This distribution can significantly change especially for higher α if the flow separates creating stall at some segments for the blade. Figure 2.12 shows the tangential and axial distributions for a WKA-60 turbine blade [14] based on a simulation. The wind turbine's rated speed is 12.2m/s. The distributions can be seen to become significantly distorted beyond rated conditions. Also the maximum axial force within the normal operation range is six times greater than the maximum tangential force, hence the significance of flapwise bending moment.
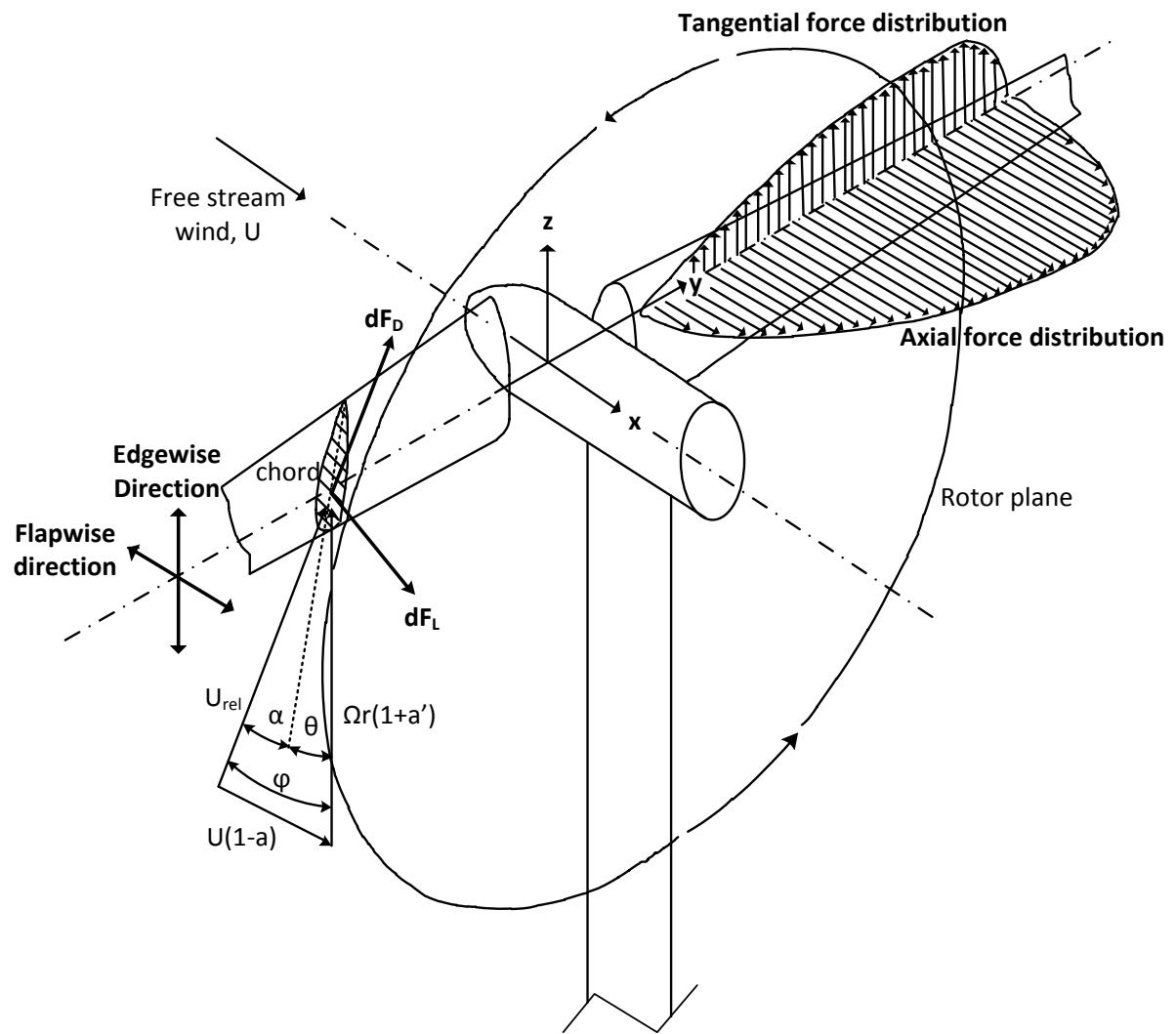
Figure 2.11 Rotor forces co-ordinates and technical terms. Adapted from [14].
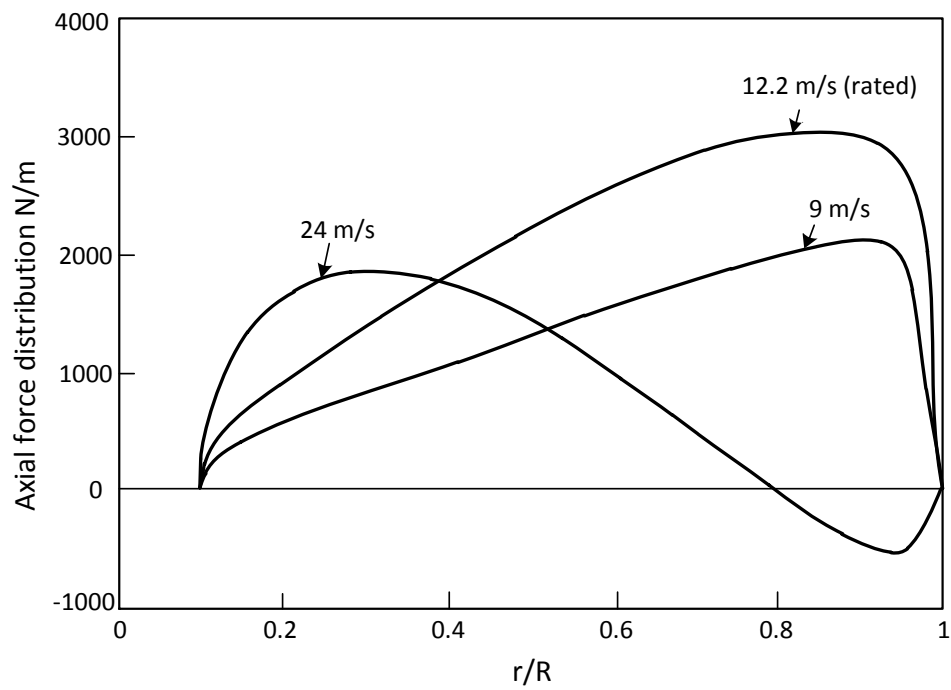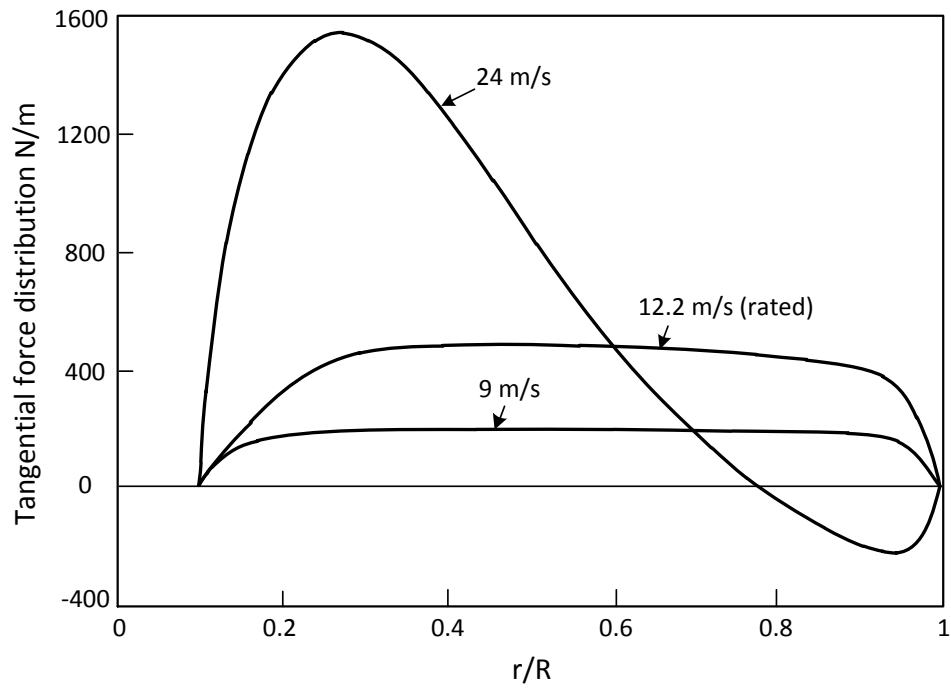
Figure 2.12 Modelled tangential (top) and axial (bottom) force distribution for WKA-60 turbine blade [14].

2.1.5.1 Effect of coning on rotor load and performance

Thrust loading on a rotor can cause the blade to bend in the flapwise direction creating an angle with the typical rotation plane. This deflection, shown in Figure 2.13 is called coning. Since the parameters used for velocity calculations are measured at right angles to the rotor axis, a modification is applied to the airfoil velocities in order to account for the effect of coning on the C_T and C_P and ultimately the rotor torque and thrust loads. The incoming freestream velocity, U, is reduced by the cosine of the coning angle Φ [15].
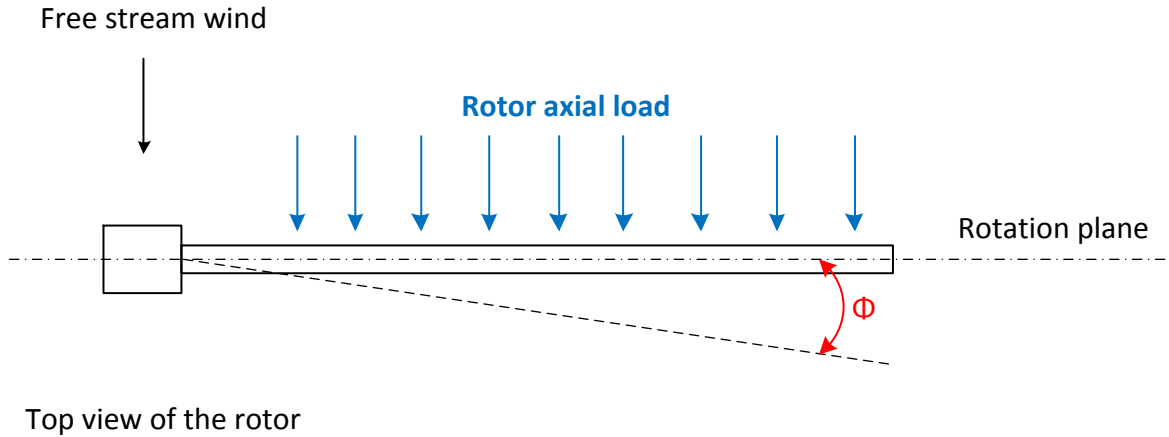
Figure 2.13 Schematic showing the coning angle Φ.

Recalling equation 2.23, the relative velocity U_{rel} for a blade experiencing coning becomes [15]:

$$U_{rel} = \frac{U \cos \Phi (1 - a)}{\sin \varphi}$$

$\qquad$ 2.39

where Φ is the coning angle measured from the plane of rotation. Substituting the new U_{rel} definition into the differential thrust definition (equation 2.24) from the blade element theory gives the new contribution to torque from each blade segment as:

$$dT = \frac{1}{2}\rho B c U^2 (1 - a)^2 \frac{\cos^2 \Phi}{\sin^2 \varphi}(C_l \cos \varphi + C_d \sin \varphi)dr$$

$\qquad$ 2.40

The same can be applied to the torque contribution of blade segments by substituting the modified U_{rel} into the differential torque definition (equation 2.52.25) from the blade momentum theory:

26

$$dQ = \frac{1}{2}\rho B c U^2 (1-a)^2 \frac{\cos^2 \Phi}{\sin^2 \varphi} (C_l \sin \varphi - C_d \cos \varphi) r dr \qquad \text{2.41}$$

An important conclusion is that the coning angle reduces the thrust and torque contribution by a blade segment by the square of the cosine of the angle. In contrast, reducing the coning angle would increase both the power and torque production.

2.1.5.2 Flapwise bending moment

A wind turbine blade under axial loading can be represented as a simple cantilevered beam [9]. The load and stress equations derived for cantilevered beams can be applied to the blade coupled with the aerodynamic force equations to create a representation of the stress distribution along the blade. Stress measured at any point β along the blade span is equal to [9]:

$$\sigma_\beta = M_\beta c / I_b \qquad \text{2.42}$$

where β is the location of a point measured from the rotor center (as shown in Figure 2.14), M_β is the moment measured at that location, c is the distance from the flapwise neutral axis and I_b is the area moment of inertia of the cross-section. The contribution to the flapwise bending moment at any location along the span of the blade can be calculated by integrating the product of the differential thrust force the distance to that point. Recalling equation 2.32 the moment at any point β can be represented as follows:

$$dM_\beta = \frac{1}{B}(r-\beta)\left(\frac{1}{2}\rho C_t U^2 2r\pi dr\right) \qquad \text{2.43}$$

$$M_\beta = \frac{1}{B}\int_\beta^R (r-\beta)(\frac{1}{2}\rho C_t U^2 2r\pi dr), \qquad R > \beta \qquad \text{2.44}$$

where dM_β is the differential contribution to the moment at location β, R is the full length of the blade and C_t is the local coefficient of thrust of the differential element (not to be confused with C_T with a capital subscript that represents the total coefficient of thrust of the whole blade). Using the coefficient of thrust equation 2.32 and including the effect of coning from equation 2.39, C_t can be represented as follows:

$$C_t = \frac{B}{2\pi}\left(\frac{c}{r}\right)(1-a)^2 (\frac{\cos^2 \Phi}{\sin^2 \varphi})(C_l \cos \varphi + C_d \sin \varphi) \qquad \text{2.45}$$

27

Top view of the rotor
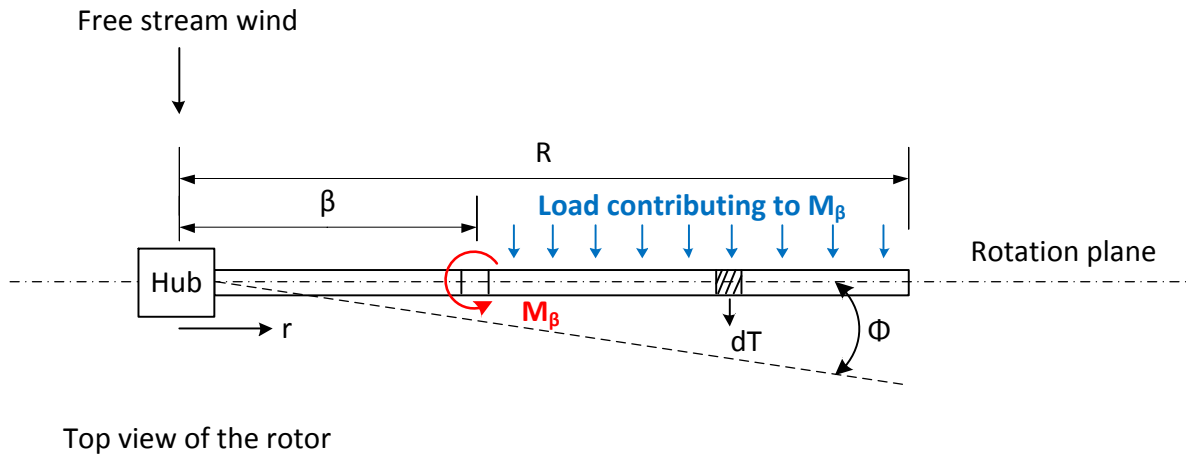
Figure 2.14 Moment at any location β along the blade span.

By combining equations 2.44 and 2.45 and performing the integration, the following important conclusions can be made about the moment at any point β along the blade:

- The moment increases:

    - when the freestream velocity increases,

    - when C_l of the blade segments between the measurement point and the blade radius that contribute to the moment increase.

$$M_\beta \propto f(U, C_l) \tag{2.46}$$

- The moment decreases

    - when β increases moving closer to R,

    - when the coning angle φ increases.

$$M_\beta \propto^{-1} f(\beta, \Phi) \tag{2.47}$$

Figure 2.15 shows an impression of the variation of flapwise bending moment with wind speed measured at different locations along the blade length of the large MOD-2 wind turbine [21]. The MOD-2 has a rotor with 180 ft. (55m) long blades utilizing the NACA 230XX airfoil series and rotates at 17.5 rpm. The mean flapwise moments were measured at two locations along the blade at $r/R = 0.20$ and $r/R = 0.65$. The experimental measurements are plotted along with the numerical prediction of the loads using a rotor performance analysis code [21]. It is clear that measurements at the point close to the blade radius length are less than the ones further off while both increase with wind speed, agreeing with the conclusions made from the theory.

28
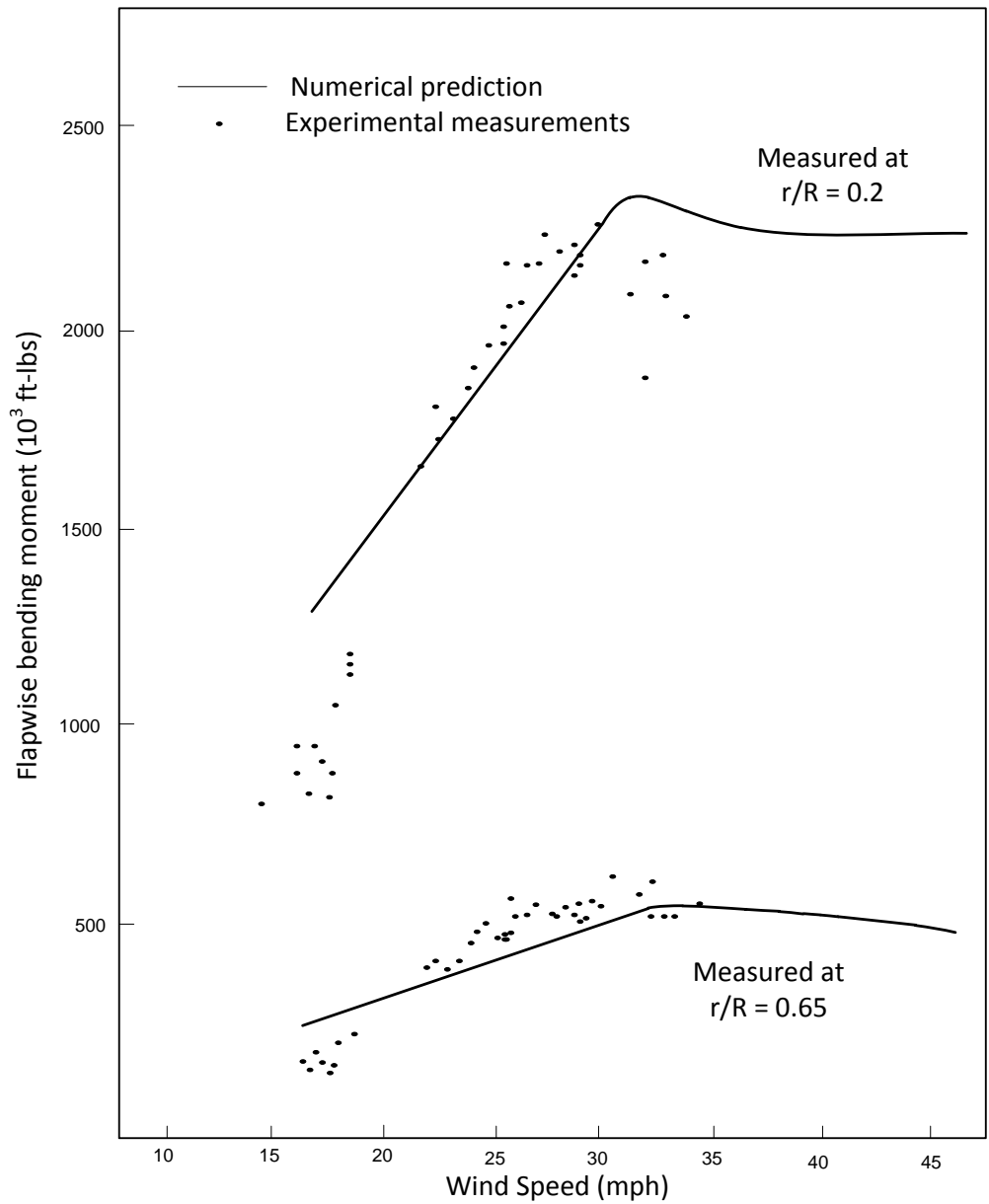
Figure 2.15 Predicted and measured bending moments at different locations of a MOD-2 turbine blade [21].

The normalized spanwise distribution of the mean flapwise bending moment for the same MOD-2 rotor measured by the two stations along with the numerical prediction are shown in Figure 2.16. The numerical prediction for another rotor, the T40, is plotted on the same axis for comparison. The T40 is a 40 m long blade utilizing the NACA 632XX airfoil series [6]. Both rotor blades showed similar spanwise distribution trends despite their distinct designs.

29
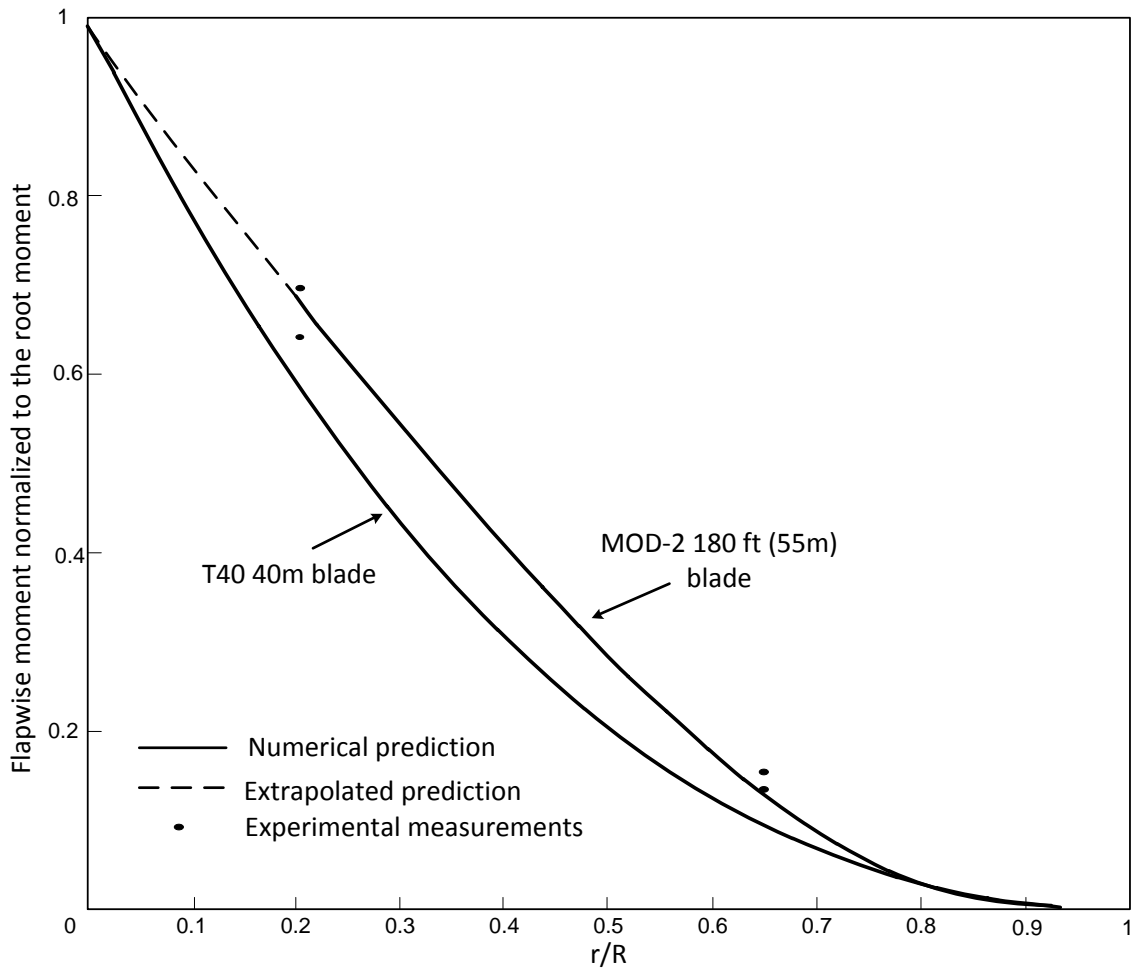
Figure 2.16 Normalized moment distribution along the T40 [6] and MOD-2 blade [21].

2.1.6 Types of aerodynamic load control

2.1.6.1 Passive Control

Passive control involves rotor designs that deform naturally as the loads increase to change the geometry of the blades. Rotor blade modifications can be achieved passively by pitch-twist coupling [9]. In this method the blade is designed such that thrust forces cause the blade to deform varying the pitch along the blade. This decreases the lift force to limit the maximum load on the blade. Another example is intentional pre-coning a rotor with a positive angle so that the rotor bends into the plane of rotation during normal operation.

Active control involves the intentional actuation of aerodynamic control surfaces on the wind turbine blade to modify the lift of the blade or blade segment. This aerodynamic surface can be the full blade, such as the case for pitch-regulated wind turbines. In that case, the blades are pitched to limit the maximum power production at the rated power to alleviate structural loads that are beyond the rated specifications of the wind turbine. More complex control systems, including sensors and controllers, can be applied using fully pitched blades to alleviate cyclic loading such as wind shear. Smaller distributed control surfaces are another example of active control of aerodynamic loads. TEFs and micro-tabs [22], [23] are examples. TEFs are movable ailerons located at the trailing edge of the blade and are the focus of this study. Their effects are discussed in more detail in the following section. Blades that incorporate distributed aerodynamic surfaces controlled by embedded intelligence systems are commonly referred to as 'smart blades' [9].

2.1.7 Effect of TEFs

TEFs are movable surfaces that are used to change the geometry and aerodynamic characteristics of the wind turbine blade sections to control the load or improve the performance in different operating conditions. TEFs were first developed for airplanes to improve the C_l of wings to increase loading during take-off and landing without changing the characteristics of cruising and high-speed flights [3]. They are categorized as high-lift devices, which also include leading edge slats, slotted- flaps, split flaps and external airfoil flap. Some of the common high-lift devices are illustrated in Figure 2.18.

Plain flap*   External airfoil flap   Leading edge slat
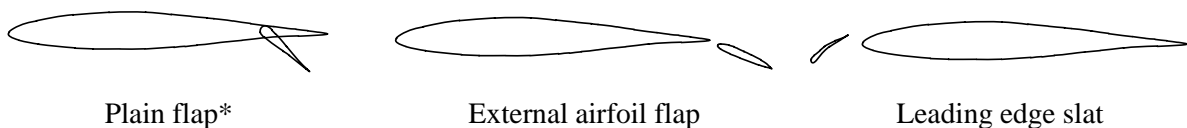
Figure 2.17 Some typical high-lift devices. Adapted from [3]. *used in this study.*

The device of interest for this study is the plain TEF, also known as an aileron. The plain TEF is formed by hinging a trailing edge section at a point within the contour [3]. Downward deflection of the flap (towards the pressure side) is called a 'positive deflection' and increases the coefficient of lift, while an upward deflection decreases the coefficient of lift [11] as shown in Figure 2.18. Deflection of the TEF changes the effective camber of an airfoil resulting in changes to its aerodynamic behavior.
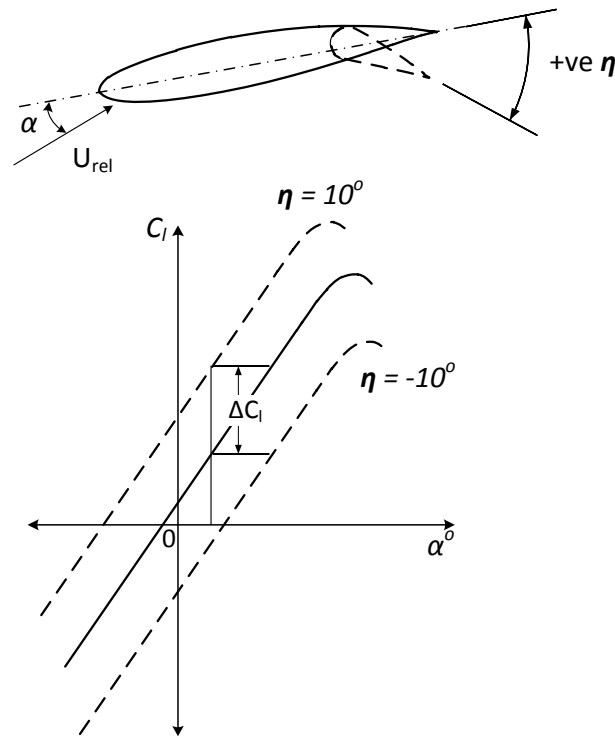
Figure 2.18 Effect of flap deflection on lift coefficient. Adapted from [11].

2.1.7.1 Thin airfoil theory on the flapped airfoil

Thin airfoil theory (see section 2.1.2.2) can be used to predict the effect of a plain TEF on the coefficient of lift of an airfoil [12]. It shows that the distribution of circulation which creates the lift forces consists of the sum of a component due to the angle of attack and a component due to the camber for any general airfoil. Thin airfoil theory solution of the distribution of chordwise circulation based on its assumptions for a general airfoil shows that (derivation can be found in [3], [12]):

$$C_l = 2\pi\alpha + \pi(A_1 - 2A_0)$$

2.48

where A_1 and A_0 are Fourier series constants that are functions of the geometry of the airfoil. The first part of the right hand side, $2\pi\alpha$, accounts for the effect of the angle of attack, while the second part, $\pi(A_1 - 2A_0)$, accounts for the camber of the original airfoil. The addition of the flap modifies the problem to the case of finding the distribution due to a camber line made up of the chord of the airfoil and the chord of the deflected flap at the flap angle.

The influence of a flap deflection can be considered as an addition to both the components above [12]. Figure 2.19 shows the combined contributions to the lift forces on the airfoil.

32
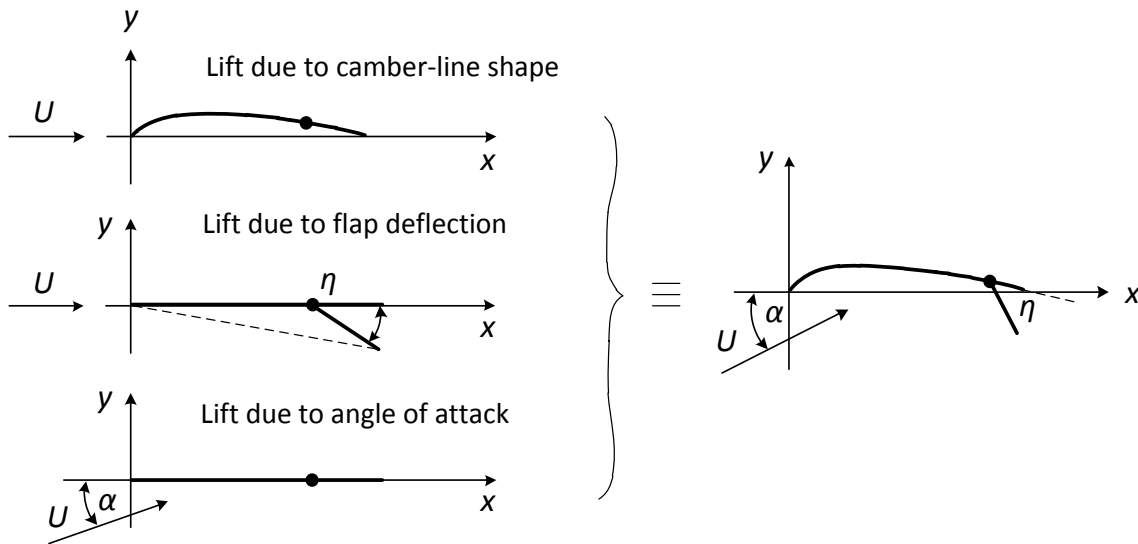
Figure 2.19 Contribution to total lift of a flapped cambered airfoil [12].

The new C_l can be shown as (derivation can be found in [3], [12]):

$$C_l = 2\pi\alpha + 2(\pi - \phi + \sin\phi)\eta \qquad 2.49$$

where η is the flap angle, and ϕ is a constant that is a function of the airfoil geometry. The flap load can be obtained using the thin airfoil theory equation with limited accuracy because the effects of viscosity that are particularly prominent over the trailing edge of the airfoil are not accounted for. Also the theory is limited to small angles of attack and can't predict the increase in maximum C_l due to the flap. However, an important conclusion can be made from these solutions. In theory C_l is linearly changing with the flap deflection angle η.

2.1.7.2 Experimental results for the C_l vs. η

In practice, C_l values are obtained from wind tunnel experiments or numerical and computational calculations. XFOIL [24] is an example of a computer program that can numerically calculate the pressure distribution on an airfoil to derive the lift and drag characteristics based on the 2D geometry. XFOIL [24] results are commonly used for computational simulations when there is a lack of experimental data as will be shown in the following section. Figure 2.20 and Figure 2.21 show an example of wind tunnel experimental results for the variation of C_l with α and η.
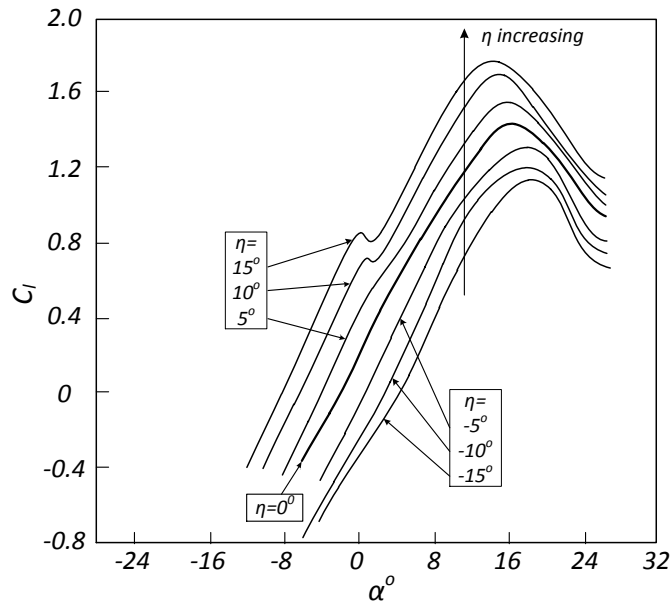
Figure 2.20 Aerodynamic characteristics of the NACA 66(215)-216 airfoil with a flap 20% of chord length [3].

Lines are polynomial fits for discrete data points.
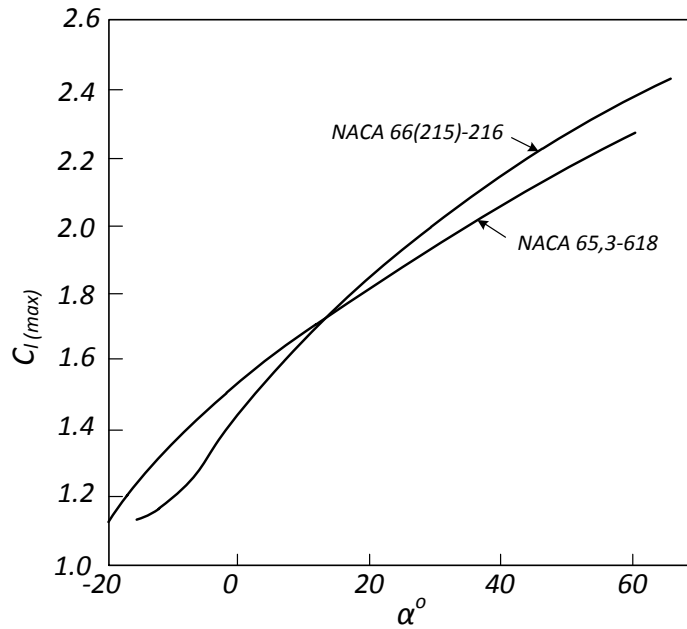
Figure 2.21 Maximum lift coefficients for two distinct airfoils [3]. *Lines are polynomial fits for discrete data.*

The experimental measurements show that the increase in η increases C_l by an amount ΔC_l for the same α. It also increases the maximum C_l although it occurs at a slightly lower α. The relationship between C_l and η is very close to linearity as predicted by thin airfoil theory.

2.2 Related work

Researchers have been working on developing and analyzing aerodynamic devices (see section 2.1.6.2) for rotor braking, power regulation and dynamic load alleviation. Recently, dynamic load alleviation has been emerging as the priority focus for research on advanced control of wind turbines since fatigue loading on large blades has been identified as one of the main obstacles to the development of larger more efficient wind turbines [5]. This study is focused on the effect of different stationary TEF formations on steady aerodynamic loads. The effect is measured for a range of fixed freestream velocities and flap deflection angles as will be outlined later on, hence experiments where the flap deflection frequency is low compared to the rotor rotation frequency were most relevant.

2.2.1 Atmospheric testing of stationery TEFs

An experiment was set-up at the National Renewable Energy Laboratory's (NREL) National Wind Technology Center (NWTC) to investigate aerodynamic control devices that are used for turbine braking applications [25]. The experiment was conducted on a full-scale instrumented HAWT incorporating three different types of TEFs with variable-span to measure the aerodynamic changes as a function of α and η. The goal of the study was to compare the results with wind tunnel experiments that assume an infinite-span to provide an understanding of how to account for finite-span airfoils.

Setup

Three blades with constant chord and twist were modified to install the aerodynamic devices at the outer end of the blade as shown in Figure 2.22. The blade utilizes a single airfoil, the NACA S809, throughout its 5 m span. The blade dimensions are shown in Figure 2.23. The aerodynamic devices covered 40% of the chord length of the airfoil [25].
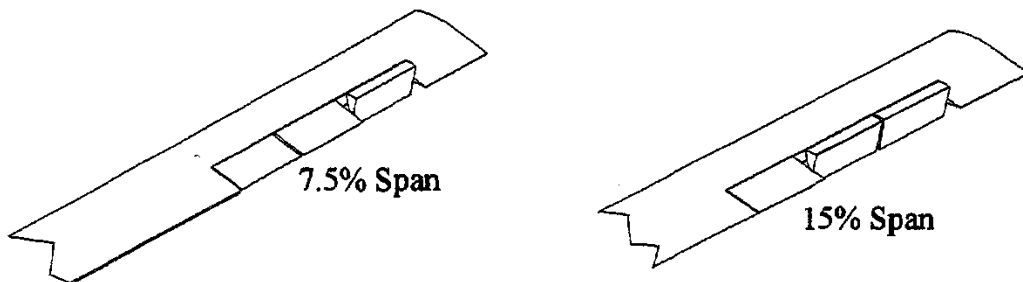
Figure 2.22 Variable span aerodynamic device deflection [25].

35
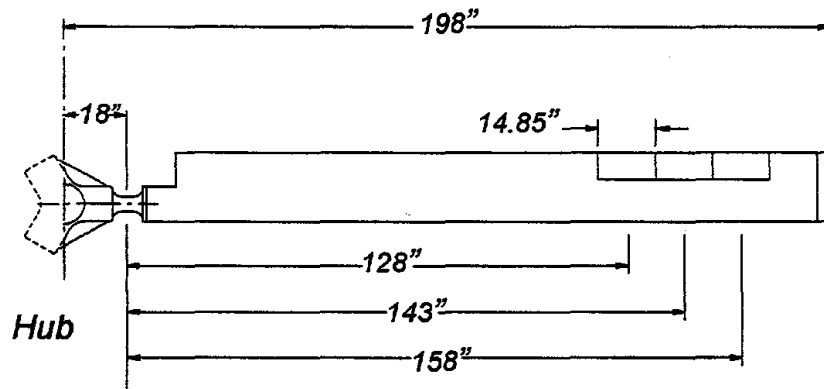
Figure 2.23 Test blade dimensions [25].

Strain gages were placed at the blade root to measure the flapwise and edgewise moments, and at the custom designed aerodynamic device actuator mechanism to measure the flap hinge moment. Additional sensors measured the blade pitch angle, yaw angle, atmospheric pressure and air temperature. The wind velocity was measured at five different lateral and vertical locations [25]. The rotor was fitted with a single blade and two counter-weights as shown in Figure 2.24, similar to this study, for the investigation of each aerodynamic device.
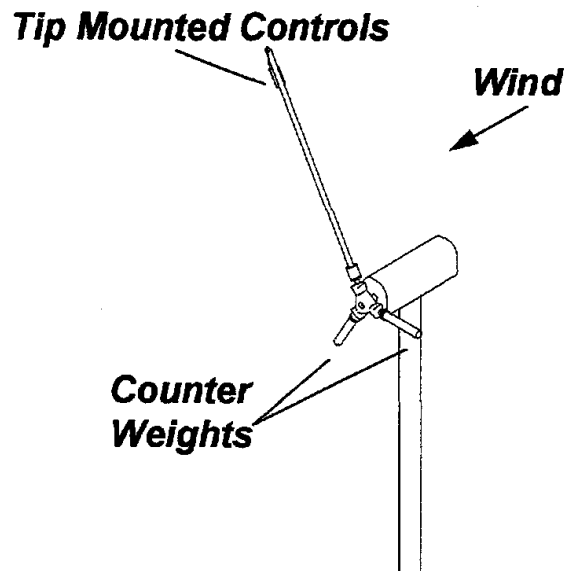
Figure 2.24 Single-bladed down-wind rotor used for investigation [25].

Test procedure

A preliminary visualization test was conducted to verify that the blade wake would convect downstream by fitting a 'smoke grenade' to the blade tip. The results agreed with previous model predictions and the tip flow moved away from the rotor before the next rotation for freestream speeds greater than 2 m/s. This value was set as the threshold for the atmospheric testing [25].

   The primary tests involved sweeping the blade through the desired range of device configurations, listed in Table 2.3, over different periods of atmospheric conditions. The data was time-averaged for 30 rotor revolutions to remove the unsteady effects. Measurements were discarded when there was a yaw error greater than 15° [25].

Parameter	Range	unit
Device deflection angle η	0, 10, 30, 60, 90	degrees
Blade pitch angle θ	0, 5, 9, 12, 15, 18, 21, 26, 31, 36, 41	degrees
Device span Δr	7.5, 15, 22.5	% radius

Table 2.3 Device configurations for testing [25].

Data Analysis

The goal of this study was to compare the effective change on the section aerodynamic coefficients, C_l, C_d and C_s, and the hinge moment coefficient with wind tunnel experiments. C_s is the suction coefficient and is determined as follows [25]:

$$C_s = C_l \cos \alpha + C_d \sin \alpha$$

2.50

The aerodynamic coefficients couldn't be measured directly with the applied setup, so the change in root-bending moment between different configurations was used to identify the effect of the devices. The angle of attack α was calculated using equations 2.21 and 2.22 from section 2.1.3.3 that resolve the velocities based on blade element theory. The induction factors that account for the blade's effect on the flow were ignored because there was no means to measure them during the experiment [25]. The data sets representing each experiment were curve-fit prior to calculating the coefficients.

Results

The flapwise and edge wise moments that were used to calculate coefficients were obtained for different conditions and plotted against mid-span α. The moments were normalized against the dynamic pressure q [25]. A sample of the curve-fit data is shown in Figure 2.25. The coefficient calculations in general showed

that the most prominent differences between the atmospheric and wind tunnel experiments were found near the stall α and Δr less than 15% [25]. Specifically, the difference in drag coefficients followed aspect ratio (the ratio between the chord length and the span) trends for other geometries such as cylinders and flat plates. The drag increments for device spans greater than 15% were similar and consistent, hence a model for prediction of the drag coefficient difference as a function of aspect ratio was suggested. The hinge moment coefficient trends were similar for both experiments [25].
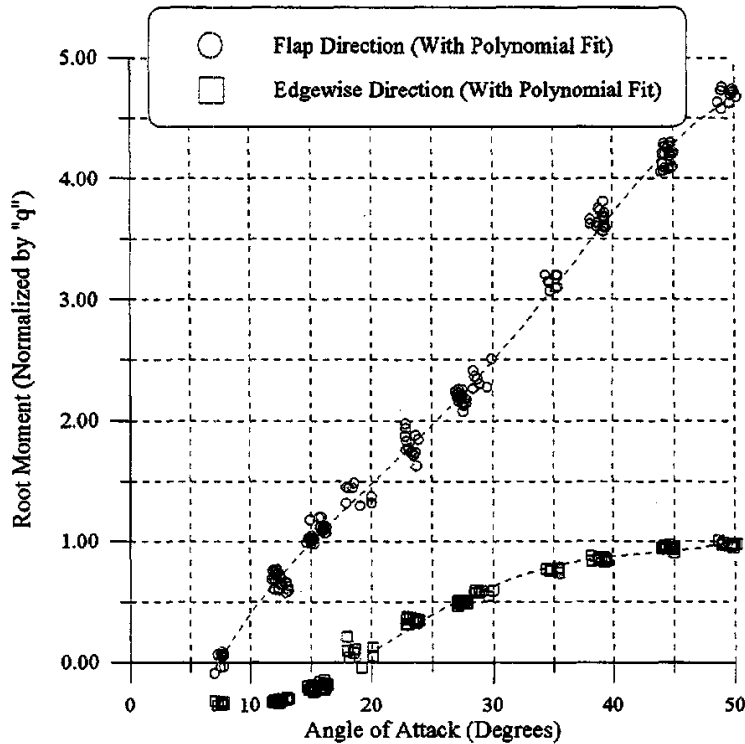
Figure 2.25 Sample data from [25] showing averaged data and the variation.

Notes

The main function of this experiment was to provide an understanding of the variation of aerodynamic characteristics of the trailing edge devices between infinite-span wind tunnel experiment data and finite-span real scenarios. This is valuable for improving the design and analysis of wind turbines that incorporate such technologies.

However, the experimental design had several drawbacks that were not accounted for. The major one is neglecting the effects of the blade on the flow which is defined by the axial and tangential induction factors (see section 2.1.3). This limitation on turbine measurements also prevented a more detailed analysis of the entire blade's aerodynamic profile. Instead root-moment changes were used to account for changes in the device characteristics ignoring interactions between different blade segments. In addition, due to the uncontrolled atmospheric conditions several extensive measurement repetitions, averaging and filtering were required to minimize associated errors.

38

Overall, this study provided an important baseline for correction of wind tunnel characterizing measurements for aerodynamic devices when applied to wind turbines. However, the effects of application of such devices to wind turbines are not limited to the infinite to finite span transition, but also due to induced vortices and rotational effects in general that the blade was exposed to [25]. A similar experiment designed for application in controlled conditions would have more advantages. It could provide the same insight while allowing the implementation of additional instrumentation that can represent the aerodynamic profile of the full-blade in more detail and would eliminate errors due to operating conditions variability. An experiment applied on a 1.6 m blade in an open circuit wind tunnel described in [26] measured the induction factors along the blade, a similar method can be applied to account for the blade effects that were ignored for the investigation.

The present study proposes and tests an experimental design similar to the one described in this atmospheric testing investigation but was applied in a large wind tunnel facility. The objectives stand short of calculating the aerodynamic characteristic changes of the trailing edge devices but provided the means for that purpose and measured the moment changes required for such calculations. The experimental design in this present study can also be combined with the procedure in [26] (as discussed later on in the Future work section) to accurately analyze the aerodynamic characteristic changes of trailing edge devices.

2.2.2 Power regulation using TEFs

A computational study was designed by Joncas *et al*. [27] to investigate the use of TEFs to control wind turbine power. The goal of the study was to assess the ability of TEFs to regulate the power output compared to a traditional pitch-regulated (see section 2.1.6.2) rotor. The objective of regulation is to modify the aerodynamic characteristics in order to keep the power production at a constant value above rated conditions.

Setup

A MATLAB® program was coded to evaluate the steady-state performance of a rotor subject to axial symmetric flow [27]. The code was based on a modified version of the BEM algorithm described earlier in section 2.1.3.4. In addition to the blade element and moment theories, the vortex theory (described in [6], [9], [27]) was incorporated in the algorithm to account for the BEM assumption that no interaction takes place between blade segments in order to improve the accuracy of the prediction of the induced velocities. Similar to PROPID [16] (section 2.1.3.6) functionality, the code was used to optimize the blade geometry for the study and to analyze the off-design performance. XFOIL [24] (section 2.1.7.2) was used to predict the aerodynamic characteristics of the airfoil at different α and η.

The blade parameters used for the design are shown in Figure 2.26. The same blade design was used for the TEF rotor and the pitch-regulated rotor, except for the root airfoil section which was extended to the hub attachment for the TEF rotor to allow flaps of any size or location to be described using the blade parameters [27].

| Hub Radius 5% R | Diameter at root 70% of Cmax | Max. Chord position 20%R | Maximum Chord Length 7,5%R | Rated Wind speed 15 m/s | Specific rating 0,45 kW/m² | Tip speed ratio 7,5 | Chord at tip 20% of Cmax |

Type of Airfoils Used Along Blade Length

| (5-20%R) Blended cross section from circular root to DU97-W-300 | (20-40%R) DU97-W-300 | (40-50%R) DU91-W2-250 | (50-70%R) DU00-W-212 | (70%R to tip) DU96-W-180 |
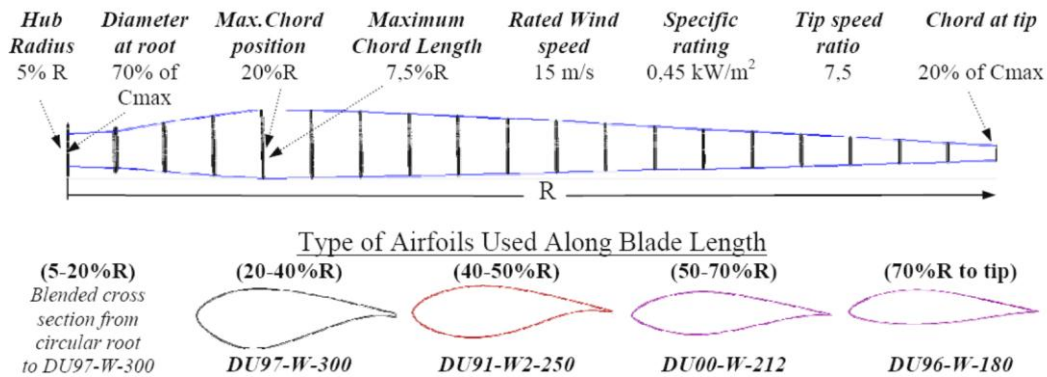
Figure 2.26 Blade parameters as a function or radius used for the blade design [27].

Results

The power below rated conditions showed a slight improvement for the TEF rotor due to the extended airfoil at the root section without the activation of any flaps [27]. To select the best flap formation (size, location), the contribution to steady load alleviation of the different spanwise distributions were compared, for flaps covering 35% of the airfoil chord (it is not clear why this initial chord value was chosen, however further analysis showed that the chordwise flap size does not have a significant influence on the results). It was determined that a flap placed between 75% of the span and the root tip contributed to 50% of the load alleviation and was selected for the simulation. It was found that this flap configuration with a chordwise length of 20% was able to efficiently regulate power above rated conditions with η less than -5º [27]. Figure 2.27 shows the TEF angles that were required to regulate power production for different wind speeds.
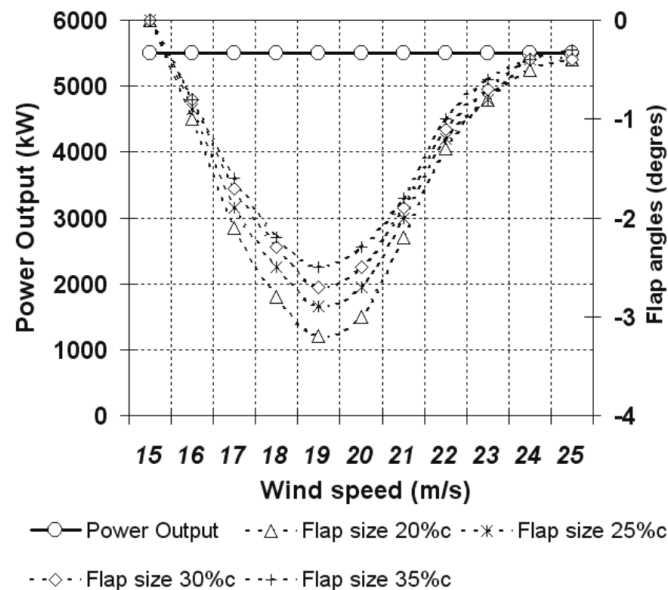
Figure 2.27 TEF angles to regulate the power above rated conditions. [27].

40

Notes

The findings of this study provide a promising insight on the ability of TEFs to regulate power. However, important factors need to be taken into consideration. The moment changes at the root section of the blade due to the operation of TEFs were not calculated or accounted for. The aerodynamics of TEFs are expected to result in higher bending moments at the root of the blade in comparison to pitch-regulation [27]. In addition, the accuracy of the aerodynamic characteristics predicted by XFOIL is limited due to the relatively large η [27], wind tunnel tests on the flapped airfoils are required to remove the uncertainties accompanied with these predictions.

The present study measures the effect of TEFs on both the bending moment and power production of the wind turbine. Currently, the range of operating conditions is limited to below rated conditions for the rotor as will be described later on. However, the experimental design can be modified to test the ability of the TEFs to regulate power above rated conditions.

2.2.3 Dynamic load alleviation

Although the scope of this study is limited to the effect of different stationary TEF formations on steady aerodynamic loads; one of the ultimate goals of this work and the developed apparatus capabilities are both focused on the experimental investigation of axial fatigue load alleviation potential of TEFs in controlled operating conditions. A brief overview of the literature involved in such studies is presented to highlight the promising potential of the technology.

2.2.3.1 Simulations and Computational studies

Lackner and van Kuik [28] investigated the potential of TEF to reduce fatigue load on a 5 MW wind turbine by simulation. The study utilized GH Bladed, an aero-elastic simulation code, and designed external controllers for the turbine and smart rotor to simulate the effect of applying individual flap control. The Upwind 5MW reference turbine [29] was used for the simulation. Applying a flap between 70% and 90% of the blade, they reported reduction between 12% and 15% in the damage equivalent load in the flapwise direction. In a similar study, Andersen *et al.* [30] also reported fatigue load reductions up to 25% applied to a model of the same Upwind reference turbine. This time deformable TEFs were used rather than the more traditional hinged TEFs. This reduced the sharp edges and kept the flow more streamlined, thus keeping the flow attached for higher η and potentially reducing drag. However, there was no direct comparison between the two configurations to quantify the benefits.

2.2.3.2 Wind Tunnel Experiments

In an experimental study, Hulskamp *et al.* [31] designed a two-bladed 1.8m diameter rotor that reflected the dynamic behaviour of the Upwind reference turbine [29] using non-dimensional scaling. Strain gages were used to measure the flapwise bending moments. The setup incorporated TEFs that had fixed length and location, hence only one flap setting could be investigated. Significant dynamic load reductions were

reported using different controller designs for the activating the TEFs. However, the effect on the power production of the wind turbine could not be measured.

2.2.3.3 Full-scale experiments

A full-scale atmospheric study was performed on a wind turbine equipped with TEF by Castaignet *et al.* [32]. The turbine was a Vestas V27 utilizing a three-bladed 26 m diameter rotor. Only one of the blades was instrumented with strain gages and modified to accommodate three hinged TEFs. However, only one of the flaps was used due to technical difficulties. The TEF was 70 cm long (spanwise) covering 5% of the blade span. Measurements with the flaps fixed at the high and low lift configurations [33], similar to this study, showed between 2-3% reduction in root moment. While the flap size was notably smaller relative to the blade than the one used in this study, the deflection angles that caused this reduction were not mentioned. Using the same flap configuration with a closed feedback controller, an average 14% flap-wise load reduction was reported.

Chapter 3

Wind Turbine Test Rig

This chapter starts by describing the previously available test rig and derives the general design requirements from the improvements required based on experience and recommendations from several previous studies that used this equipment [26], [34]. The next section outlines the design, fabrication and assembly of the wind turbine test rig. The design constraints are discussed as the basis for the rationale behind the selection of outsourced components, and the design of the manufactured components. The final section outlines, the geometry, range of operation, instrumentation, and capabilities of the final assembled wind turbine test rig.

3.1 General design requirements

The turbine previously available was a purpose built horizontal axis wind turbine rig with a maximum capacity of 3.6 kW and a maximum rotational speed of 240 rpm. The wind turbine rig was comprised of: the tower, nacelle, generator and the drivetrain. The tower was constructed of two separate inline tubular steel poles downstream one another with guy wire support, as shown in Figure 3.1. This formation involves numerous members and severely limits the ability to instrument the support structure of the wind turbine for load and vibration measurements. The structure also showed instability towards the higher end of the rotation speed range. The towers were supported by long crisscrossing frames laid flat on the ground, they were obstructing an access hatch that allows underground wiring to the control room.

The nacelle was placed on the tower and contained the low speed shaft directly connected to the turbine rotor, a series of toothed belts and shafting to increase the shaft speed to the high speed shaft which was coupled to a DC generator. This speed reduction arrangement required two levels of shafting and resulted in an undesirable nacelle geometry. The nacelle was disproportionately larger than a comparative turbine in both vertical and horizontal directions and is not streamlined. It extended beyond the hub part of the blade causing irregular interference with post-rotor wind streams. An experimental BEM study measuring post rotor wind velocities excluded measurements up to 30% of the blade due to irregular wind patterns caused by nacelle interference [26].

A 3.6 kW DC motor/generator was used as the basis for the electrical design of the system. This dual-mode aspect was used for speed control. The rotational speed control system was manual and was achieved by varying the voltage across the armature and field windings of the motor using two variacs. This method of controlling the speed limited the testing capability of the rig. The two variacs required continuous tuning

to keep the rotation speed close to the required value. It was difficult to keep a consistent value for the rotation. That also limited the scope of measurements to steady-state operating conditions; since measurements during transient conditions (when the freestream wind speed is changing) requires a quick response with accurate feedback.

Generator loading was achieved by using a network of resistive elements in a load bank, to dissipate the energy generated by the turbine blades as heat. The network consisted of six heater bars rated for 500 W each which gave a total rated absorption of 3000 W. The voltage coming from the grid and into the load bank was monitored directly by a Keithley 2700 Digital Multimeter Data Acquisition and Data-logging System [35]. The current was measured at the generator/motor and load bank inputs by determining the voltage drop across in-line shunt resistors. From the voltage and current measurements the power entering and leaving the generator/motor could be determined. In order to determine the amount of power that the generator/motor was absorbing or producing the difference between the power measured at the grid input and the load bank was determined. Calculating power using this method required several repeated measurements and complex calibrations. The friction losses in the different components of the drive-train and specifically the use of belts to reduce speed significantly added to the unpredictable nature of losses between the power producing rotor and the motor output where the measurements were calculated. The geometry of the drive shafts limited the capability of adding a torque sensor or other components without extensive redesign of the drive-train.

Figure 3.1 Image of previous Test Turbine Rig

The general design requirements are derived from the summary of features that require improvement:

- *Support structure*. The new support structure was required to allow accurate instrumentation to measure loading and vibrations due to wind and turbine interaction. Also, to be stable throughout the range of rotational speeds and allow access to the control room hatch.

- *Nacelle geometry*. The nacelle was required to be streamlined and not extend beyond the regular hub portions of a rotor.

- *Speed Control*. The speed control method was required to be automatic and have the shortest possible response time to changes in operating conditions.

- *Power Measurement*. Power was required to be calculated accurately without being subject to friction losses within the system.

In addition, safety, the ability of the grid to be upgraded, and flexibility of the requirements on rotors attached are further considerations for the design.

3.2 Specific design constraints

The turbine test rig's main function was to control the rotation speed of the rotor and provide power measurements. The test turbine rig was designed to operate in the UW wind facility and was required to maintain compatibility with existing rotors. The facility and its characteristics are described in detail in section 5.1. The rotation speed for the rotors range up to 220 rpm [34], [36]. The rig rotational range of operation will be limited to an upper range of 230rpm. Studies done by Devaud *et al.* [37] on the flow characteristics of the facility such as jet stability in different regions in addition to an extensive and comparative blockage analysis of wind tunnel testing on HAWTs performed by previous researchers in this group [38] suggest that the rotor diameter not exceed 3.3 m. These maximums were used as the basis for the determination of any related design parameters. The center of the stable jet region, located at 3.05 m from the ground, is set as the hub height for the test rig.

The maximum wind speed produced by the UW wind facility is 11 m/s (refer to section 5.1 for details) and power available in that wind for a swept area of a 3.3 m diameter based on equation 2.11 (in section 2.1.3.1) is 6.8 kW. The theoretical maximum C_p based on the Betz limit for any wind turbine as discussed in section 2.1.3.1 is 0.59. Medium and small scale rotors tend to have lower C_P and the rotors used in this facility were designed to have their maximum C_p (the design point) in the mid-range of the wind speeds with lower values near both ends of the wind speed operating range. Based on those two facts it was safe to assume that C_p at the maximum velocity of the facility for any rotor will never exceed 0.5. The maximum power capacity requirement of the test rig was the product of the expected C_p and the power available in the wind at the maximum velocity, and was equal to 3.4 kW. The maximum torque calculation was based on the maximum power and an assumption of 200 rpm for the rotation speed, the result was 170 Nm. The axial load capacity of the rig was calculated based on historic data from previous experiments. The rotor design by Gertz [34] theoretically produced approximately 400 N of axial force. A threshold of double that value was set as the factor of safety for the test rig components.

The nacelle size was required to not exceed the hub portion of any rotors used on the test rig. The current rotor has a hub cut-out of approximately 150 mm, 10% of the rotor blade length. The average hub cut-out should not exceed 12%, limiting the maximum size of the nacelle to a 200mm radius. The nacelle was also required to provide a ±15° yaw angle for experiments that simulate cross wind and yaw angle errors. Table 3.1 summarizes the test rig design parameters.

Design parameter	Range	Unit
Rotation speed	≤ 230	rpm
Power capacity	≥ 3400	W
Torque capacity	≥ 170	Nm
Axial load	≥ 800	N
Nacelle size (diameter)	≤ 400	mm
Yaw angle	±15	degrees
Hub height	3.0-3.1	m

Table 3.1 Test rig design constraints

There were two important load frequency ranges that were considered in the design of the load bearing components. Namely the single period (1P) and triple period (3P) load frequencies which are loads that interact with the system once and three times per revolution. The 1P loads are those expected from an unbalanced rotor and have the same frequency range as the rotation speed. The 3P load are those that interact with the system 3 times per revolution based on the usual three-bladed configuration used for rotors. An example of this type of load is the wind drag on the tower during the rotor rotation, and its range is equal to triple the rotation speed frequency. The natural frequencies of the load bearing components were designed to be safely distant from the operational frequencies.

Design parameter	Frequency range (Hz)
Rotation speed	≤ 24.1
1P load	≤ 24.1
3P load	≤ 72.3

Table 3.2 Operational frequency ranges

46

The test rig is a single production unit that is intended for intermittent activity, unlike mass produced commercial wind turbines, thus higher preference is given to safety rather than weight and size optimization for the structural load bearing components as long as they are within the design constraints. Also, in addition to the stated design parameters, the test rig was required to be able to safely handle mechanical and electrical stresses resulting from normal operation and include measures to reduce the risk of damage to the components in cases of emergencies and malfunctions.

3.3 Component Selection

The component selection process was based on comparative research of available components that fulfil the design requirements. Cost and after sales service from different suppliers were additional factors for choosing the most suitable quote. The following sections describe the features of selected components.

3.3.1 Motor and brake

The motor selected was a Marathon Electric Y287 184TC frame vector motor [39]. It requires a 230 V three-phase 60 Hz power supply which is available at the UW wind facility. The maximum continuous power capacity is 5 Hp and the maximum speed is 1800 rpm. This motor is capable of acting as a generator based on the output shaft torque supply, a feature which was a main requirement for our application. It also included an encoder for accurate speed control through a feedback loop with the controller. The outer dimensions of the motor's frame were within the maximum requirement of the nacelle size, the largest dimension was approximately 310 mm. The motor was also coupled with a face mounted coupler brake for emergency braking and for parking the rotor while the rig is not in use or if required to remain stationary for special testing purposes. The coupler brake has the same outer frame diameter as the motor and is triggered electronically by the same control system discussed in a section 3.3.3.

3.3.2 Gearbox

The Nord helical in-line gearbox SK572.1 [40] was used to reduce the motor speed to the required operational range of the wind turbine rotor. The gearbox had the same 184 TC frame size of the motor and a 7.49:1 reduction ration suitable for the operation speed range. Its torque capacity is 430 Nm, safely higher than the expected torque from normal operation of the test rig. The manufacturer rating for the gearbox efficiency is ≥97% [40]. However, this number is expected to drop in cooler temperatures since it is oil lubricated.

3.3.3 Electrical and control systems

The motor is controlled by an SP2203 Control Techniques Vector drive [41]. It is a 7.5 Hp 230V variable frequency drive (VFD) capable of a continuous output of a 22A current. The drive was configured in a closed loop AC mode to communicate with the motor, the encoder and the brake. It was mounted on a panel

and placed 2 m behind the test rig tower inside the test area. An additional communications sub-panel placed inside the control room was connected to the main tunnel through an underground access duct (see the facility description in section 5.1). The power generated by the turbine is dissipated through a dynamic brake resistor (DBR) mounted outside the main panel.

The sub-panel includes start, stop, diagnostic and emergency stop buttons and a touch LCD screen that can be used to set-up input parameters and display output data. The VFD is fully programmable as a proportional-integral (PI) controller [42] to control the process variable, which is the rotation speed in this case. The PI controller tuning was performed by the supplier. The controller parameters, diagnostic and operation commands are accessible through Ethernet connection from either of the panels to a personal computer. The control system can be operated without a personal computer with limited features, Table 3.3 shows the functions that can be completed using the sub-panel directly. The main panel is placed in the test area to allow the DBR to be cooled by the wind generated by the test facility during operation.

Function	Input	Details
Set rotation speed	Touch screen	Selects rotation speed, can be changed during operation
Set acceleration/ deceleration rate	Touch screen	Sets the acceleration/deceleration rate for start, normal stop, and speed change operations
Toggle LCD view	Screen side diagnostic button	Switches between Speed and power reading view, more detailed current and voltage readings and diagnostic view
Start	Green push button	Starts operation for the specified speed
Normal Stop	Red push button	Stops operation normally using the motor for deceleration
Emergency stop / apply brake	Large e-stop button	Applies coupler brake during operation or when already normally stopped
Emergency stop reset / release brake	Orange push button	Releases the coupler brake

Table 3.3 Sub-panel features.

3.3.4 Bearings

Pillow block bearings were selected for supporting the drive shaft for easier alignment and assembly (see section 3.4.3 for details on alignment). The bearings are required to isolate the axial load and radial loads from the rotor from the rest of the drive-train while maintaining its alignment. The best combination for that function is to place two consecutive bearings ahead of the rotor, a taper roller bearing followed by a

regular ball bearing. The main function of the roller bearing is to eliminated the moment on the first bearing and maintain alignment as illustrated in Figure 3.2. Details of the drive-shaft design with the loads involved are discussed in section 3.4.1. It was found that the load capacity of the bearings that fit the shaft size required for our loading calculations were suitable for the design requirements. A Dodge P2B-E-115R [43] double tapered roller bearing was used for as the main bearing placed at B1 as shown in the figure, and a Dodge P2B-SCED-115 [43] ball bearing was used as the secondary bearing placed at B2.
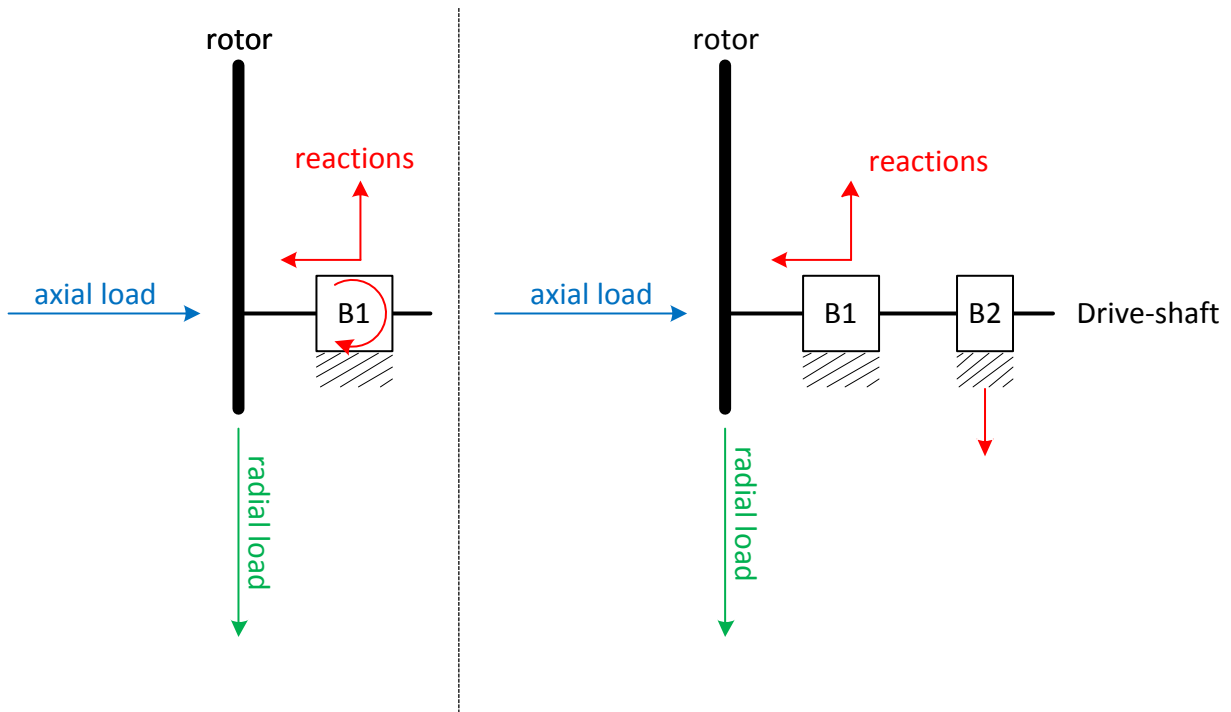
Figure 3.2 Single vs. two bearing reactions.

3.3.5 Torque sensor and couplings

The torque sensor was sized based on the torque capacity requirement in the design constraints (shown in Table 3.1). The Futek TRS 605 [44] was selected for this application. It is a non-contact shaft to shaft rotary sensor with a 200 Nm torque capacity and an additional encoder. The encoder can provide position and speed data to synchronize various measurements from the rotor operation. The torque sensor was not used in this study as it was delivered after the completion of testing and its assembly into the rig is currently a work in progress. An alternative method for power production measurement was used and is discussed in section 5.3.2.

   The torque sensor is the most expensive component in the test rig and is very sensitive to misalignments. Excessive misalignments could lead to damage or skewed readings. To protect the sensor and compensate

49

for minor misalignments it is placed between two couplings. Regular straight shaft coupling are not suitable due to their torsional flexibility and backlash. The R+W BKL metal bellows couplings [45] are special couplings that are torsionally rigid and provide backlash free transmission of torque. They also compensate for lateral, axial and angular misalignment with relatively low restoring forces.

3.4 Component Design and fabrication

The component design process was based on the expected loads from the design constraint ranges. They were required to comply with the geometry and stresses derived from the design parameters and selected component combinations, while fulfilling the general design requirements. The following sections discuss the design and fabrication of the custom-made components.

3.4.1 Drive-shaft

The drive shaft transfers the torque from the rotor along the drive-train while carrying the weight of the rotor. Based on the design constraints and by comparison to available rotors, the maximum allowable weight for any rotor that will be designed for this rig was limited to 40 kg. The rotor designed by Gertz [34] weighs 23 kg and is made from a fiber glass composite with a steel hub. The weight of the rotor used in this experiment is approximately half of that, the detailed design and characteristics of this rotor is discussed in the next chapter. The shaft protrudes 90 mm from the first bearing as shown in Figure 3.3 with the center of gravity of the rotor between 20 to 30 mm ahead of that, this distance multiplies the radial load and adds significant bending stress to the shaft. In addition to the fixed weight, an-unbalanced center of gravity of the rotor was assumed when designing the shift since it adds to the radial load when combined with the angular acceleration of rotation. The shaft was sized based on the bending stress caused by the radial load and the maximum torque for the design constraints in Table 3.1. The shaft design and fabrication procedures can be found in detail in the UW wind turbine test rig: design, installation and operation report [46].
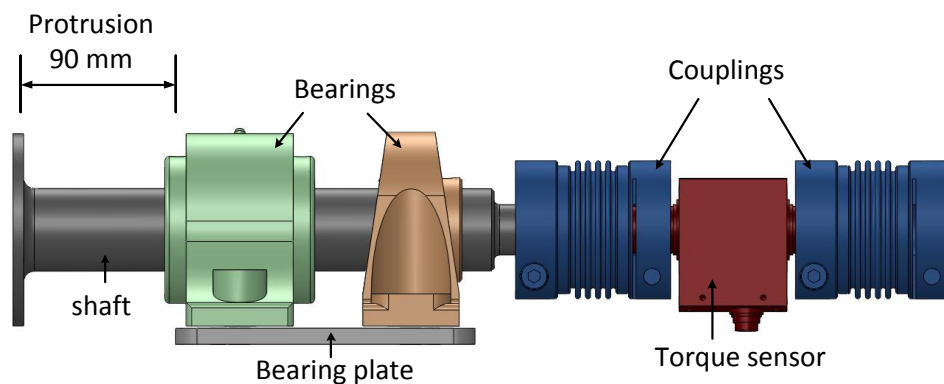
Figure 3.3 Shaft protrusion.

In an ideal design the emergency brake would be placed right behind the rotor before the rest of the drive-train to avoid exposing the other components to the high braking torque. However, it was difficult to find

or design an electromagnetic brake that can easily fit in that space while keeping within the geometric design constraints, so the coupler brake described in section 3.3.1 was used instead. This arrangement puts the components between the brake and the rotor at risk of damage in emergency braking situations due to the momentum of the rotor at high rotation speeds. To address this, safety shear pins are incorporated in the shaft design between the shaft end and the shaft face-plate. The safety shear pins are sized to fracture when the emergency brake is applied, isolating the rotor from the rest of the drive-train. Shear pin design details and replacement process can be found in [46].

3.4.2 Nacelle frame

The nacelle frame design was based on the weight and dimensions of drive-train components. It is also required to provide the range of yaw angles stated in the design constraints. The frame was designed in a ladder-like truss arrangement with two main spars spanning the sides where the components are bolted. Four cross members add torsional rigidity and support to the structure. 4 x 2 inch rectangular structural steel tubes with a quarter inch thickness were used for the frame members. A finite element simulation was performed on the frame using the maximum loads based on the design constraints to confirm its structural capacity, the results can be found in [46]. To facilitate alignment of the drive-train components attached to the frame, steel shims were designed to be welded to the attachment areas and precision machined to a flat surface. Figure 3.4 shows a 3D model of the nacelle with an annotation for the main outer geometry and main features. The frame fabrication process can be found in detail in [46], the dimension drawings can be found in Appendix A.
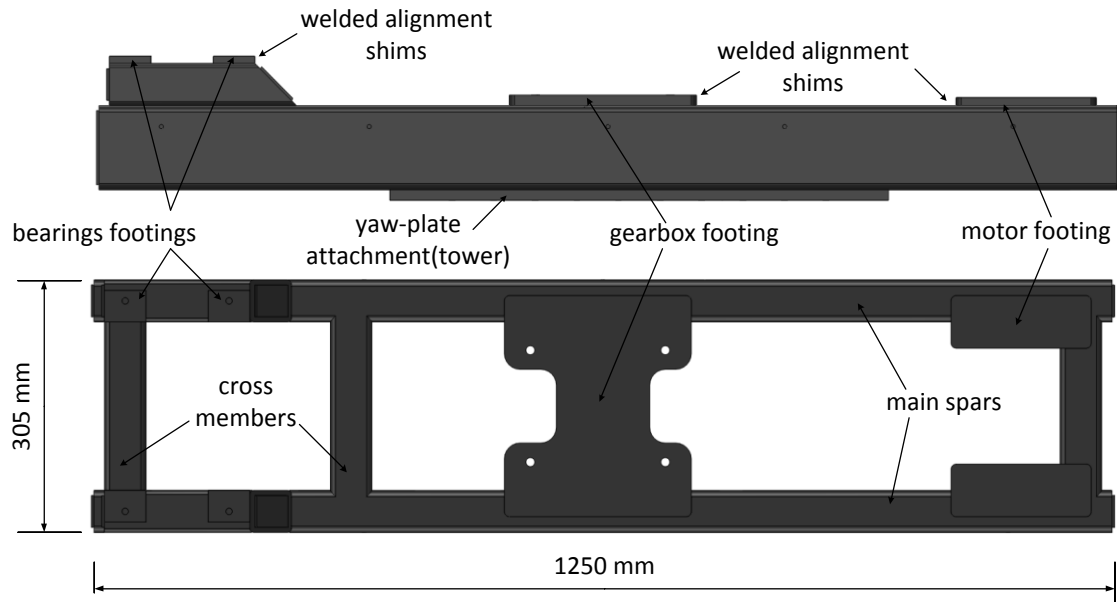
Figure 3.4 Nacelle frame features.

Two additional plates were designed to perform important functions required from the nacelle frame, yaw and center of gravity adjustment above the tower neutral axis. The latter is necessary since the test rig

is expected to function using different rotors with different weights. Re-positioning the nacelle above the tower's neutral axis minimizes stresses on the tower and reduces vibrations. The yaw-plate allows changing the yaw angle in fixed increments of 5°. The center-plate moves fore and aft in fixed increments to adjust the nacelle center of gravity above the tower, keeping the center of gravity within 2 inches of the neutral axis. Figure 3.5 shows a model of the nacelle frame and plates.
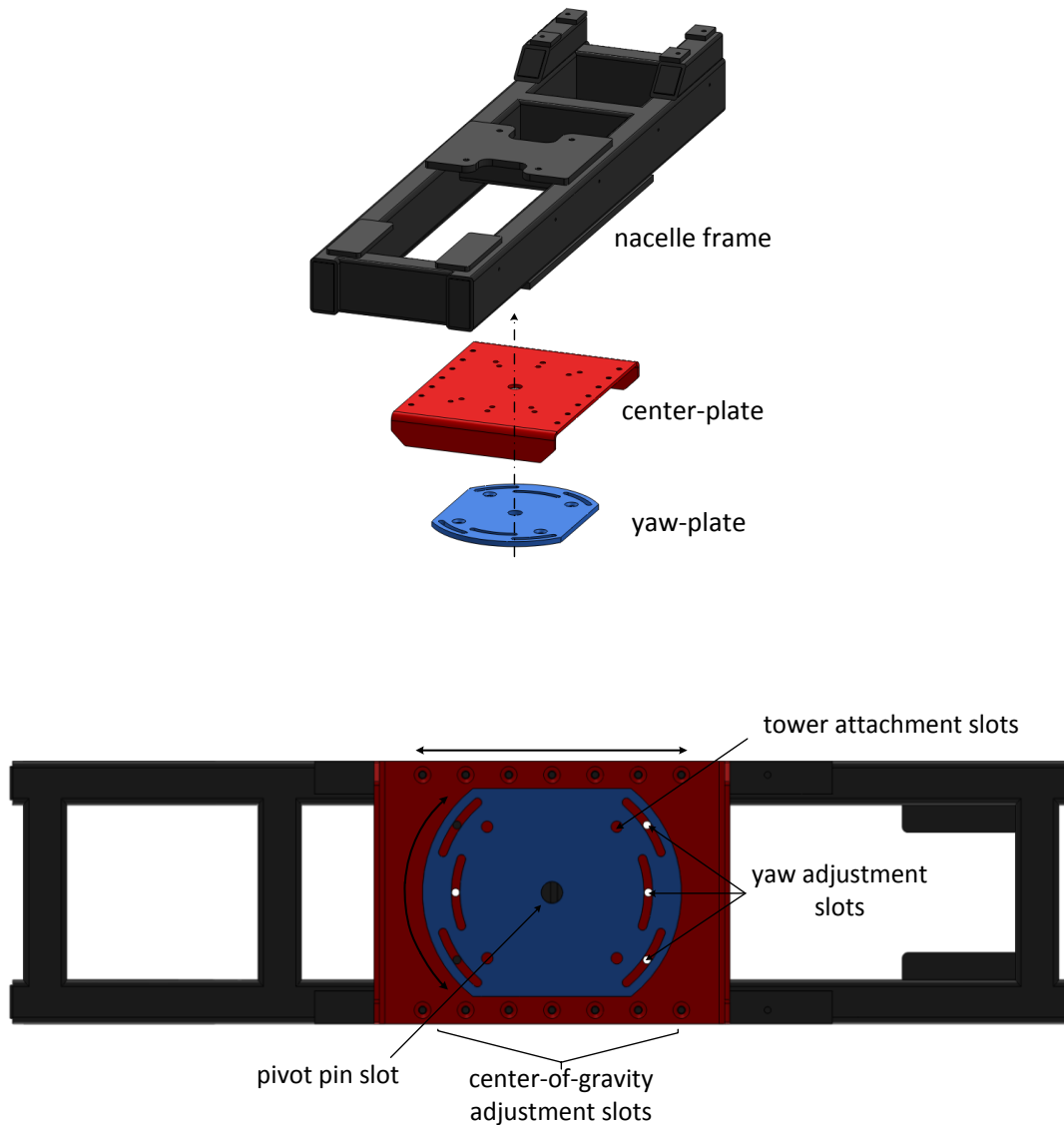
Figure 3.5 Nacelle frame and adjustment plates.

3.4.3 Drive-train alignment

Accurate alignment is key for smooth operation and prolonged life-time of the drive-train components. The full drive-train arrangement shown in Figure 3.6. The gearbox, brake and motor were rigidly coupled together through face-mounts embedded in their standard 184TC frames. This makes the three components act as a single alignment element with respect to the frame and were designated as group A. The bearings were the only other components that were attached directly to the frame. The bearings were required to be aligned with each other and with the gearbox output shaft, this will automatically align the freely rotating couplings and torque sensor in between. Attaching each bearing separately to the frame and attempting to align them simultaneously with each other and the gearbox would be a very difficult and tedious process. To overcome that, the bearings were first aligned together and rigidly attached to the bearing alignment plate. This makes them act as another single alignment element with respect to the frame, they were designated group B.
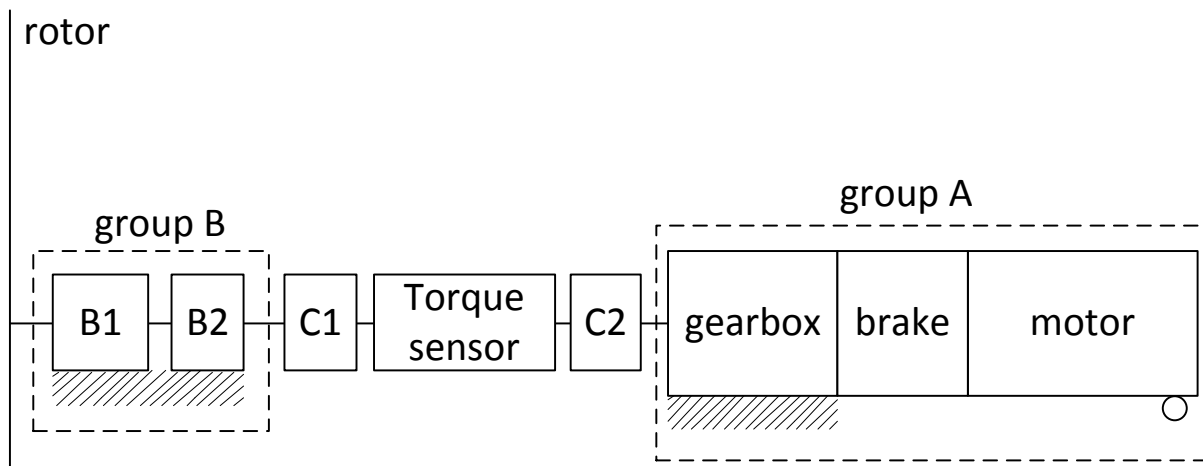
Figure 3.6 Drive-train alignment plan.

The bearings were aligned on the plate using a dial indicator and by placing very thin shims placed between the plate and the bearing footings, then they were tightly and rigidly fastened to the plate. The gearbox is then bolted to the welded and machined alignment shims on the nacelle frame. This is the only rigid connection to the frame from the group A components. Although the motor has a fastening feature that can be used to rigidly attached it to the frame, it is not used and the motor is placed on a rubber padding glued to the alignment shims labelled 'motor footing' in Figure 3.4. Rigidly fastening the motor would add unnecessary strain to the face couplings between the group A components and could affect the alignment of the gearbox on the frame. Group B components were then aligned to the gearbox output shaft using a dial indicator and by placing thin shims between the bearing plate and the nacelle frame.

Figure 3.7 shows an annotated image of the assembled drive-train and nacelle frame after alignment. A dummy shaft was used to connect the couplings during testing as the torque sensor was not yet delivered.
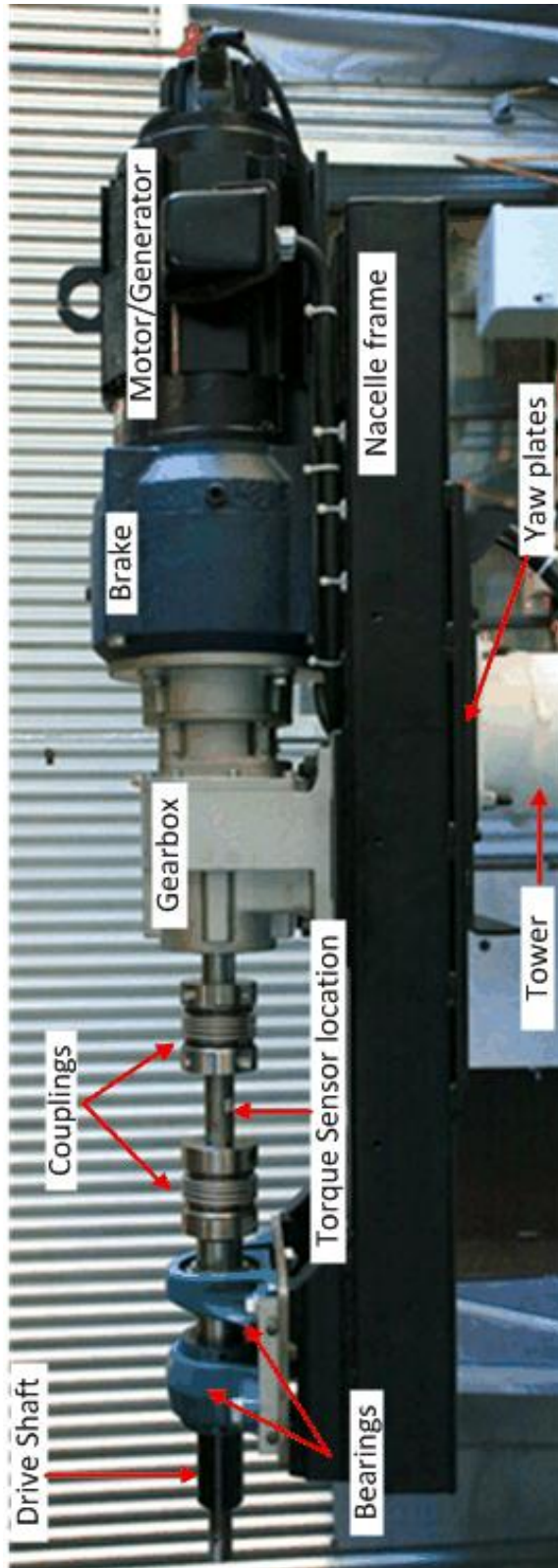
Figure 3.7 Assembled Nacelle Components (without cover)

3.4.4 Hub

The hub assembles the rotor to the end of the drive shaft. It was designed with consideration to the fact that the test rig is required to support different rotors. The hub design was made from two steel plates with a six-bolt patterns that match the drive-shaft end and a four-bolt pattern that was used as a standard for rotors used with the previous test rig. The two plates are separated by a PVC mounting spacer that is machined based on the width of the blade root. This adds flexibility to the hub requirements so that it can accommodate blades of different root thickness by machining a new PVC spacer. Rotors that require a significantly different hub connection would require a re-designed hub compatible with the drive-shaft end plate bolt pattern. Detailed dimension drawings of the hub plates and spacer are in [46].

The hub also holds a front mounted Michigan scientific S8 precision slip-ring [47]. The slip-ring is a vital component of the test rig assembly as it provides a wired connection to the rotating components creating eight communication channels. These communication channels were used to connect the measurement devices on the blade to the data acquisition systems and the pc. Figure 3.8 and Figure 3.9 shows the 3D model and images of the hub assembly, including the slip-ring.
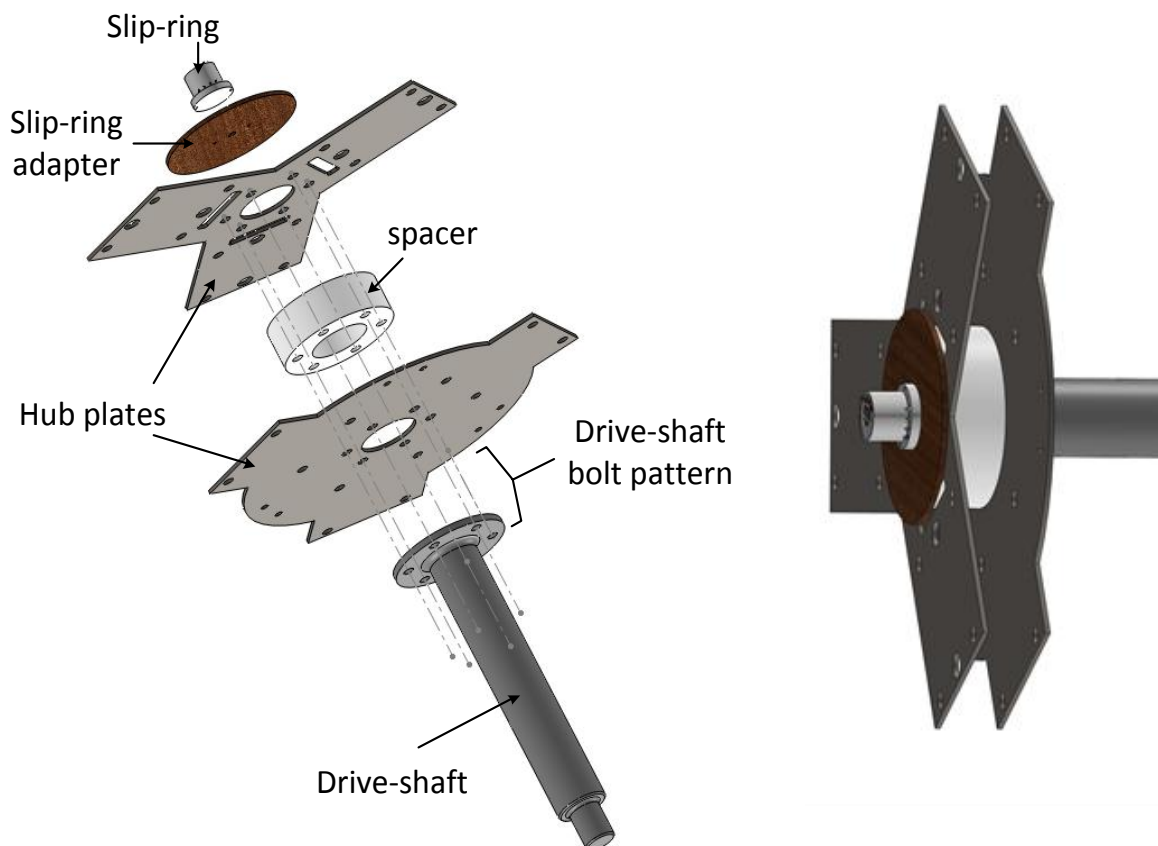
Figure 3.8 hub to drive-shaft assembly.

55
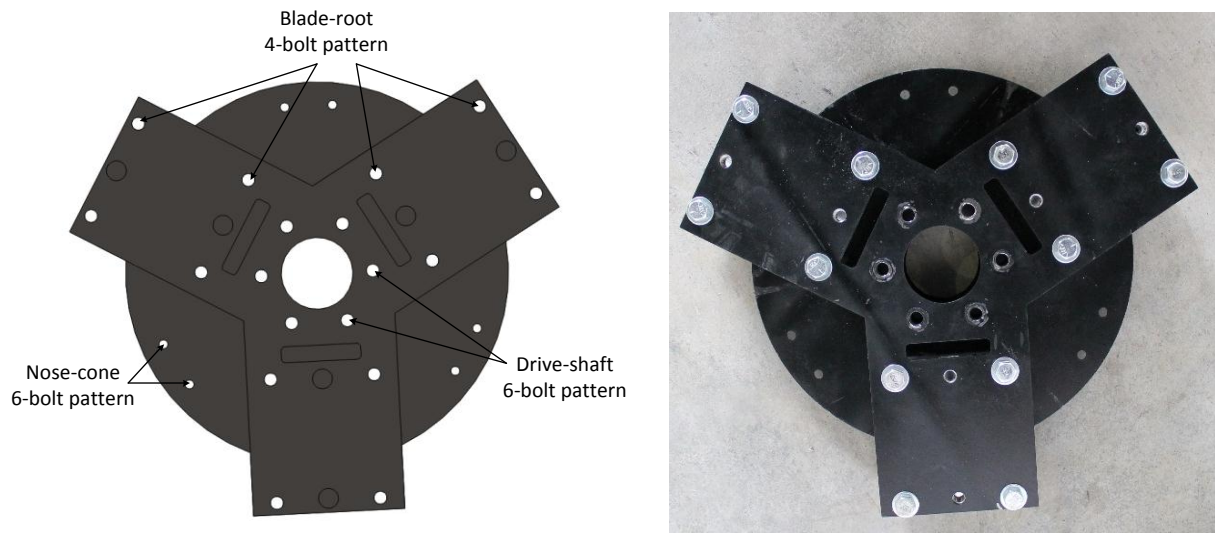
Figure 3.9 Front view 3D model and image of Hub assembly showing bolt patterns.

Figure 3.10 Image of assembled rotor using new hub design and Gertz [34] blades.

3.4.5 Nacelle cover

The nacelle cover's design depends mainly on the size of the components in the drive-train. The components were selected with reference to the geometric design constraints, as a result the final nacelle design dimensions fit well within the allowable range. Figure 3.11 shows a comparison between the nacelle size of the previous test rig and the new test rig designs. The nacelle size and blunt corners were one of the most significant disadvantages of the previous rig (as discussed in section 3.1) as they obstructed and separated the post rotor flow skewing any velocity measurements close to the nacelle. The more streamlined and significantly smaller nacelle utilized in the new rig is more representative of realistic wind turbine geometries and nacelle/flow interaction. This addresses measurement problems outlined in previous experiments done in the facility such as the experimental BEM prediction study by Johnson *et al.* [26] and others.
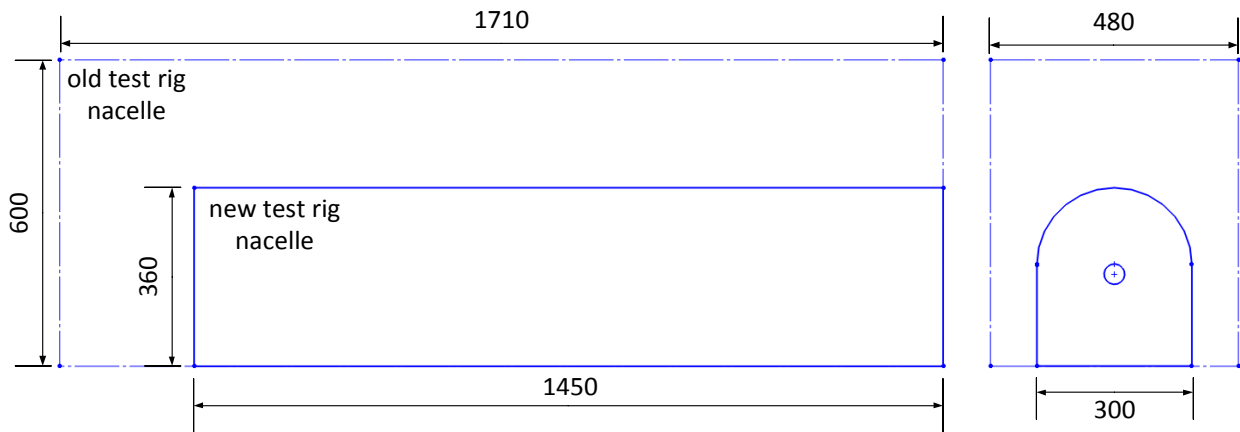
Figure 3.11 Nacelle cover side and front view comparison, all dimensions in mm.

The nacelle covers the top part of the frame while the lower part is open to the freestream wind to allow natural air cooling of the motor, additional slot and vanes were incorporated in the design to facilitate flow around the drive-train. Internal support webs, shown in Figure 3.12 were used to add support to the nacelle structure and reduce vibrations. A clear plastic section was added to show the two couplings and torque sensor can be observed during operation for visual observation of any irregularities or misalignments. Figure 3.13 shows the 3D model and image of the nacelle cover assembled to the frame.
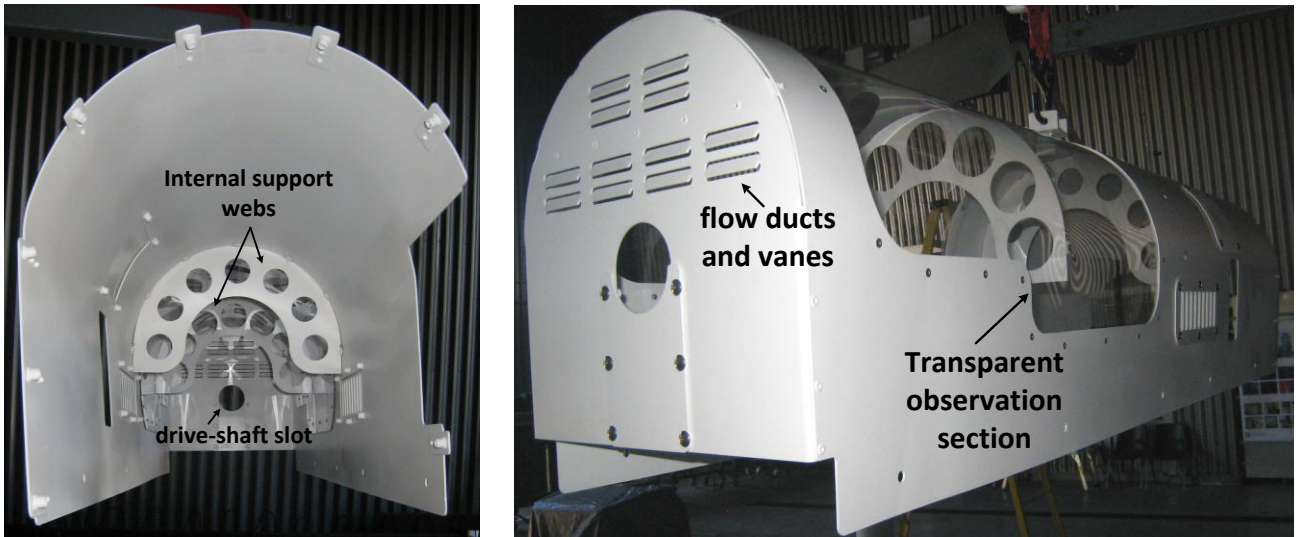
Figure 3.12 Nacelle cover images.
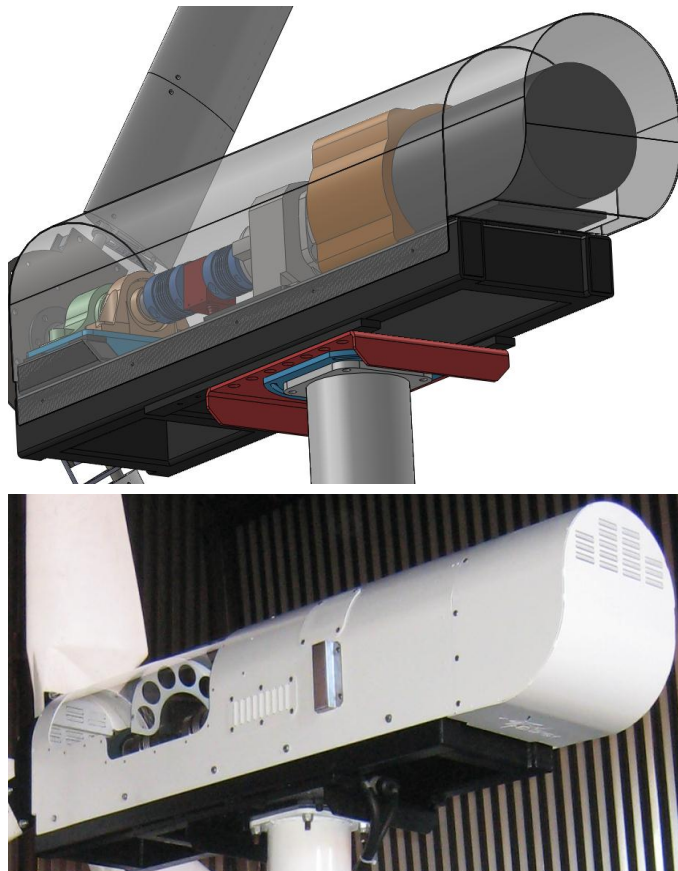
Figure 3.13 Assembled nacelle cover 3D model and image.

3.4.6 Tower

The tower is the final component to be designed after selection and design of all other test rig components. The structural design is based on the loads from the design constraints in addition to the weights of the rotor, drive-train and nacelle frame that are placed on top of the tower. There are two criteria that must be satisfied for a safe tower design. The tower must be stiff enough to withstand the maximum stress from the static loads and maintain a natural frequency safely distant from the frequencies of the dynamic loads.

The total weight of the hanging components is approximately 220 kg and their center of mass can only be adjusted in 2-inches increments which is the maximum possible distance from the neutral axis. Figure 3.14 shows a free body diagram of the static forces and reactions acting on the tower. Applying an eccentric mass to the column acting in the direction of its axis yields a maximum stress at the center of the column. The rotor axial force is derived from the design constraints in Table 3.1. There are two points of interest where the maximum total stress could be found, the center of the tower where the stress due to the eccentric nacelle weight is maximum and the bottom of the tower where the bending moment caused by the rotor axial load is maximum. The maximum stress caused by an eccentric load can be calculated using equation 3.1 [48]:

$$\sigma_{max} = \frac{F}{A}\left(1 + \frac{ec}{r^2}\sec(\sqrt{\frac{F}{EA}}\frac{L_e}{2r})\right) \qquad 3.1$$

$$r = \sqrt{\frac{I}{A}} \qquad 3.2$$

where σ_{max} is the maximum stress, c is equal to the radius of the tower, E is the modulus of elasticity of the tower material, A is the cross-sectional area, I is the area moment of inertia of the tower cross-section, e is the eccentricity of the weight (as shown in Figure 3.14), and r is the radius of gyration and is calculated using equation 3.2.

The tower is subject to constant frequency loads specified in the operational frequencies list in Table 3.2. The tower can be modelled as a uniform upright cantilever with a point mass on top [9]. The natural frequency of such a configuration can be calculated using the following standard equation [49]:

$$f_1 = \frac{1}{2\pi}\sqrt{\frac{3EI}{(0.2235m_{tower} + m_{turbine})L_e^3}} \qquad 3.3$$

where f_1 is the fundamental natural frequency, m_{tower} is the tower mass, $m_{turbine}$ is the mass of all the suspended components including the nacelle and rotor, and L_e is the effective length of the tower.
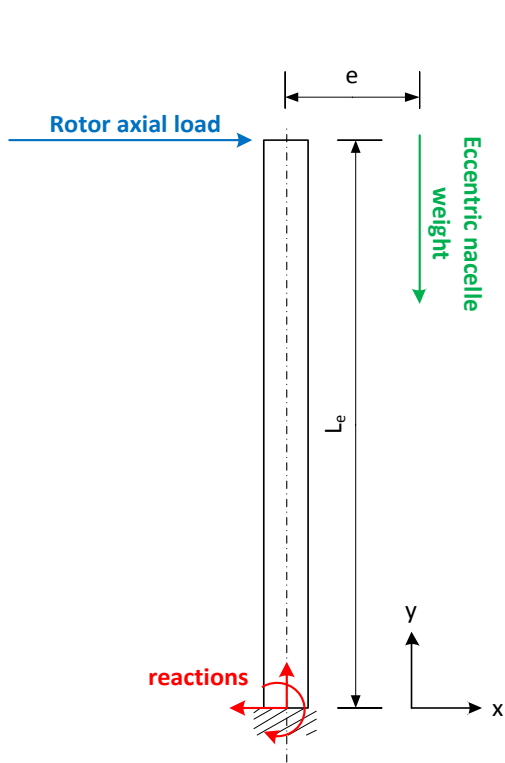
Figure 3.14 Static forces stress analysis of test rig tower.
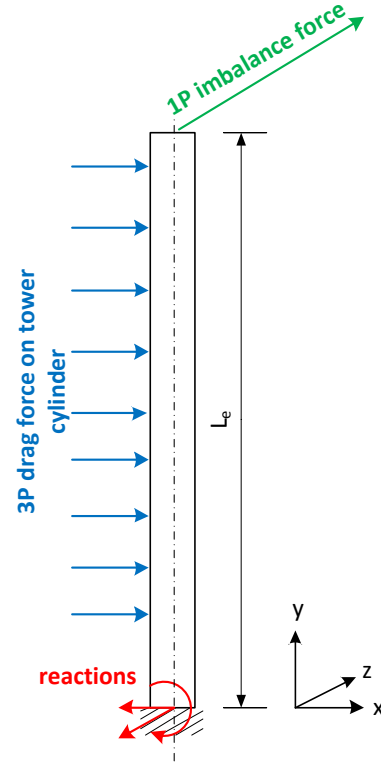
Figure 3.15 Dynamic forces for frequency analysis of test rig tower.

The main component of the tower is required to have a cylindrical cross-section to allow multi-directional strain gage instrumentation for measuring axial and lateral loads and vibrations as stated by the general design requirements. Although the required height is specified in the design constraints, triangular welded gussets are used to modify the effective length L_e of the tower used in the calculations to achieve the natural frequency target. The design variables are the effective length L_e, the pipe diameter and thickness. In addition to the main cylinder, two plates are welded at the top and bottom, with the triangular gussets supporting the attachment to the bottom plate. The top plate includes a bolt pattern that matches the yaw-plate described previously in the nacelle frame design. The bottom plate includes the bolt pattern for fastening the tower to the concrete facility floor.

The final dimensions were governed by the frequency analysis. The frequency of the 3P loads from Table 3.2 is 72.1 Hz, the tower thickness was increased and effective length was decreased well beyond the safety factor for the static load stress analysis case in order to reach a safe natural frequency equal to 1.5 times the 3P loads. The main tube was made from a 6 inch schedule 80 cold rolled pipe. The final tower specifications that successfully satisfied all the design criteria are summarized in Table 3.4. Figure 3.16shows a 3D model of the tower with an annotation for the main outer geometry and main features. Detailed design calculations are in [46]. Dimension drawings can be found in Appendix A.

Specification	Value	Unit
Height	2.78	m
Effective length L_e	2.03	m
Weight	170	kg
Natural Frequency	108	Hz
Tube thickness	110	mm
Material	Carbon Steel	-

Table 3.4 Final tower specifications
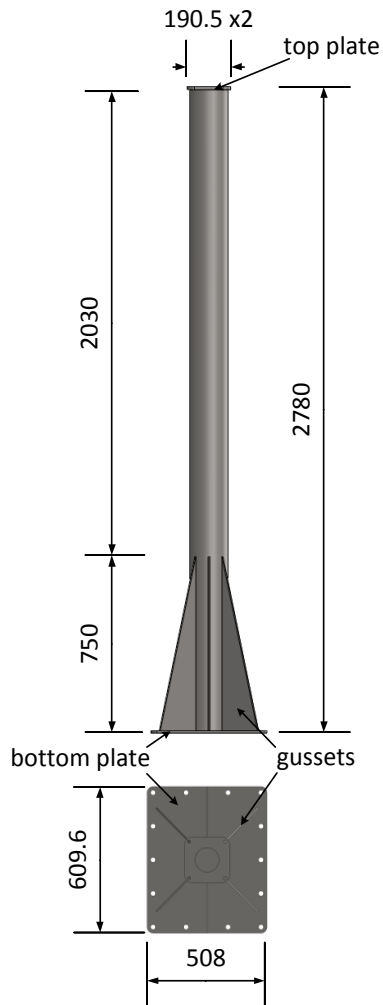
Figure 3.16 Tower main dimensions and features.

Figure 3.17 Tower image (side view).

61

3.5 Test rig Assembly

The test rig was assembled using a manually operated material lift, shown in Figure 3.18, available at the UW wind facility. The nacelle was centered onto position above the tower using the center-plate and aligned to the required direction using the yaw-plate. A laser level was used to initially align the yaw-plate along the centerline of the facility. Detailed assembly procedures are attached in [46].

The assembly/unassembled process was significantly simpler and faster compared to the previous test rig. This is a very important feature of the new system since the facility is shared with other research groups and the test area is occasionally required to be cleared for other testing. Figure 3.19 shows images of the fully assembled wind turbine test rig.

Figure 3.18 Test rig main components.

62

Figure 3.19 Fully assembled wind turbine test rig images with Gertz [34] rotor.

3.6 Connections and communications

The main panel contains the VFD and was the control center of the test rig electrical system. It communicated with the motor, brake, and secondary control panel. The connections to the components on the nacelle utilized surface cables running along the outside of the tower. The slip-ring, sub-panel and Ethernet connection cables ran through an underground access duct to the control room. All cables were designed with a rugged quick snap connectors for safe and easy connection and disconnection.

The VFD controlled the rotation speed through an analog closed feedback system that included a separate connection to the motor encoder. It also engaged/disengaged the coupler brake electronically as required during operation. The brake was engaged by default for safety. Figure 3.20 shows an outline of the communication connections between the different test rig components including the slip-ring.
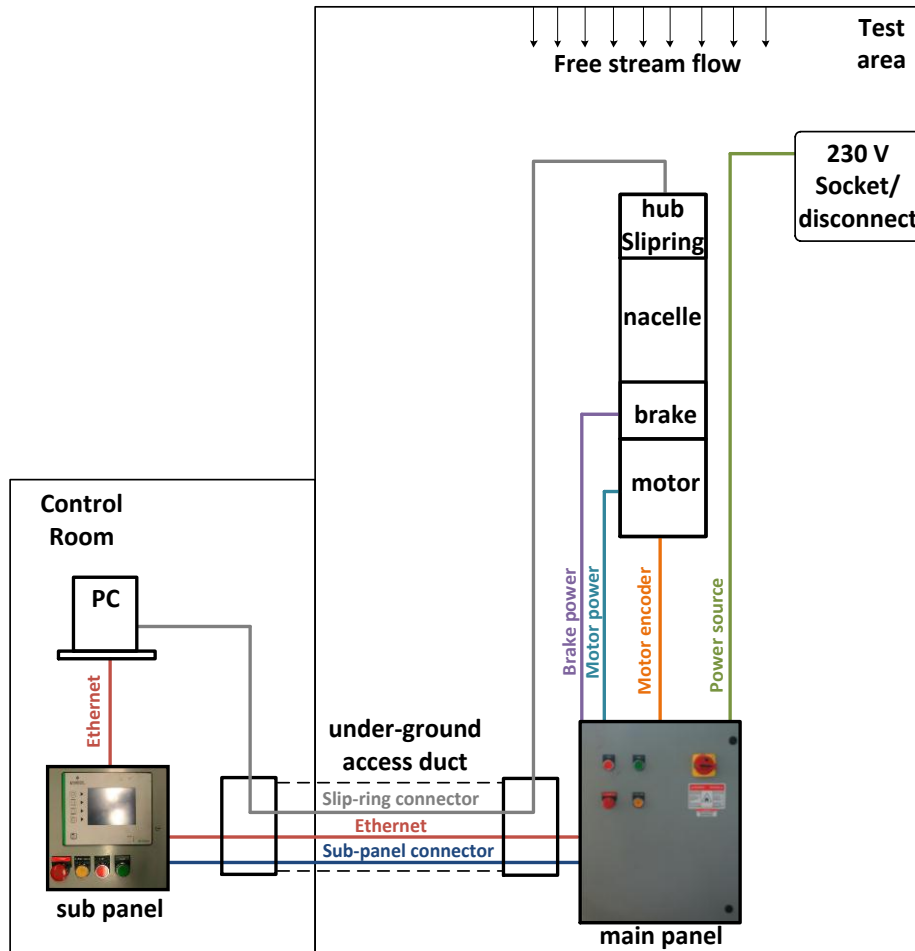
Figure 3.20 Test Rig Communications

3.7 Assembled test rig final specifications

The final assembled test rig successfully the met or exceeded the general design requirements (section 3.1) and specific design constraints (section 3.2), except for the alternative power production measurement instrument which was included in the design and acquired but not installed before the testing phase of this project. The final specifications of the assembled test rig are listed in Table 3.5.

Specification	Value/Range	Details
max dimensions	3.4 x 1.5 x 0.3	m
total weight	350	Kg
natural frequency	108	Hz
rotation speed	0-230	rpm
yaw angle	± 20	degrees
max rotor weight	80	kg
power capacity	3.7	kW
interface	touch-screen	Sub-panel
connection	Ethernet	panel to PC

Table 3.5 Final test rig specifications

Chapter 4

Modular 3D Printed Blade

This chapter outlines the aerodynamic and structural design of the rotor used in this study. The investigation required the design and fabrication of a modular blade that accommodates customizations for testing the TEF in a range of settings. The details and benefits of a novel 3D printing approach used for the fabrication of the modular blade is discussed.

4.1 General design requirements

The goal of this project was to build and test a system that could successfully be used to demonstrate the use of TEFs for active flow control applications. Although the testing for this specific study involved only static cases of different TEF parameters, the rotor was designed with consideration of the ability to accommodate active dynamic TEFs for continued work on the test rig and rotor system. The general design requirements of such a rotor are listed below:

- *Range of operation.* The rotor was required to work within in its normal range throughout the operational parameter ranges available in the UW wind facility (described in section 5.1) and the wind turbine test rig (described in Table 3.5).

- *Customizable trailing edge flap parameters.* The rotor was required to allow the modification of length, location and deflection angle changes of the TEF for different testing cases.

- *Dynamic and static flap activation.* The TEFs were required to maintain static deflection angles throughout testing, while accommodating dynamic activation for continued studies.

- *Precise non-obtrusive strain measurements.* The blade should accommodate instrumentation for precise strain measurements without interfering with the normal aerodynamic flow around the airfoil.

- *Safety and structural integrity.* The blade including its instrumentation and active components was expected to be created from a more complex assembly of components than a regular wind turbine blade. The assembled rotor was designed to function safely throughout its normal operational range.

Wind turbine blade aerodynamic designs can be more complex through utilizing different airfoils, chord lengths and twist angles along the blade span in order to maximize the blade efficiency and power production at the design operational conditions. Since the primary interest of this study was focused on the changes caused by the TEF activation, maximizing blade efficiency was not a priority, and a simpler design that meets the general design requirements more closely is preferred. Similar reported experiments from other workers applied the same design method. The atmospheric study on aerodynamic control devices [25] discussed in section 2.2.1 utilized a constant chord and twist blade using a single airfoil along the span. The closed wind tunnel experiment on a small sized HAWT designed by Hulskamp *et al* [31] used a blade with a partially varying chord and twist, however, the portion of the blade that included trailing edge flaps had constant airfoil, chord and twist. That blade was not capable of changing the flap location or length. Andersen *et al* [50] applied wind tunnel experiments on a fixed blade with a DTEF, the blade design also utilized a constant airfoil, chord and twist throughout its length. Applying such a design also makes the flap active control, parameter customization, and computer 2D and 3D simulation and comparison significantly easier.

4.2 Specific design constraints

Since the rotor was assembled to the new wind turbine test rig and operated in the UW facility, it was designed based on the ranges of operating conditions available. The test rig rotation speed is limited to 230 rpm. Although, the goal was not to maximize efficiency or make an optimal design, it was of interest to maximize power production from the rotor design to analyze the effect on power in addition to structural effects of flaps activation. In order to maximize power production, higher rotation speeds are required. The chosen rotation speed for the blade design was 200 rpm. The reason this speed was chosen rather than the maximum 230 rpm was to leave an adequate range of higher-than-design rotation speeds to possibly test the effect of operating at those conditions. This was also the design speed for the existing Gertz [34] rotor. In section 3.2 of the previous chapter it was concluded from studies done on the flow characteristics of the facility that the rotor diameter should not exceed 3.3 m. This was used as the basis for the determination of the test rig maximum power capacity so that a rotor radius at the maximum recommended range will not exceed the power or torque capacity of that rig. The design blade length was thus set to be between 1.6 and 1.7 m to account for the hub length. The maximum wind speed produced by the UW wind facility is 11 m/s (refer to section 5.1 for details). In order for the rotor to remain in its normal range of operation and avoid stall which distorts the axial load distribution on the blade, the design point is set to be between 6.5 and 8.5 m/s.

Although the standard for HAWTs is to have a three bladed rotor, for this purpose a single bladed rotor was sufficient. There are two reasons to justify that, first, the communication channels with the rotor that were provided by the slip ring (section 3.4.4) and used for measurements and control are limited so that there is not enough channels to instrument more than one blade. Second, the load patterns are symmetric on each blade but the overall efficiency of the rotor is reduced. Again, this was not of significance since the goal of this project is to study the effects on load and power augmentation of the blade with activated trailing edge flaps rather than to create an optimum rotor design. In addition, consideration is made for prototyping time and cost for the test rotor. The rotor was set to have one aerodynamic blade and two counter-weights

attached to the three-blade hub for the sole purpose of balancing the rotor in order to reduce excess vibrations and loads on the hub, bearings and the tower.

The effects of flap length, location and angle on the axial load reduction are of interest. In order to have a varying flap length, the design was required to incorporate at least two flaps that can be activated simultaneously or separately based on the experimental testing plan. In addition, the flap location was also required to be moveable along the blade length. The flap dimensions and pitch range were based on similar studies (section 2.2). Table 4.1 summarizes the design constraints applied on the rotor.

Design parameter	Range/value	Unit
Rotor radius	1.6 - 1.7	m
Rotation speed	200	rpm
Design speed	6.5 - 8.5	m/s
# aerodynamic blades	1	-
Flap width	10 - 30	%chord
Flap length	10 - 20	%radius
Flap pitch	± 15	degrees
# of Flaps	2	-

Table 4.1 Rotor design constraints

4.3 Aerodynamic design

The aerodynamic blade design was based on the design constraints from the previous section. The process involved selection of an airfoil selection and determination of the geometry defined by the chord length and pitch angle, while the blade length range was set through the design constraints. The blade design was then ran through a model to predict performance for validation against experimental results.

4.3.1 Airfoil selection

The NREL S83X [51] series were designed specifically for wind turbines of 1 to 3 m blade length. The series is made up of the S833, S834 and S835 airfoils. The airfoil performance data was corrected by Gertz [34],to account for rotational augmentation and extended to cover the operational range of angles of attack. In addition to have been designed for this scale of wind turbines by NREL, the availability and access to

the airfoil performance data is a very significant motivation for using an airfoil from within this set for the new blade design.

Since the new blade had a constant airfoil and geometry throughout its span, a single airfoil was selected from the series. Based on recommendation from the NREL report [51] Gertz placed the S835 at 40% of the blade radius, the S833 at 75% and the S834 at 95%. The regions in between were linear blends of the airfoils. The S833 was the clear choice since it was placed at the portion of the blade that contributes most to power production as expected theoretically and also proved experimentally. A study done by Johnson *et al.* [26] on the Gertz rotor concluded that the power contribution percentage of different blade segments peaks at 70% of the blade. The airfoil, shown in Figure 4.1, also has a relatively thick trailing edge compared to the maximum thickness. This would make any modifications to incorporate a hinged trailing edge flap more feasible.

NREL S833

Figure 4.1 NREL S833 airfoil [51].

4.3.2 Geometry determination

The geometry was determined by obtaining the optimum values for the chord and pitch angles for the blade. The BEM design code, PROPID [16] (section 2.1.3.6) was used. The parameters used for the BEM model were acquired from the design constraints. The blade length was set to 1.7 m to achieve maximum power and axial load on the blade. The top of the range for the design wind speed, 8.5m/s, was selected to avoid stall within the UW wind facility wind speed range since the rotor has a single-blade configuration. The chord length range was set to 150 - 200 mm based and the target was to find the values for the chord and pitch that maximize the power production at the design point. The PROPID [16] input parameters including the design point, aerodynamic models and specified blade geometry are summarized in Table 4.2.

The simulation results suggested a 178mm chord and 6º pitch angle for the blade. These details complete the airfoil aerodynamic design. The PROPID [16] code was used again to predict the off-design performance of the single bladed rotor over the range of wind speeds available. This prediction is compared to the experimental performance in the results section. The PROPID analysis input file can be found in Appendix B.

Category	Parameter	Value
Design point	Wind speed	8.5 m/s
	Rotation speed	200 rpm
Rotor geometry	Blade length	1.7 m
	Hub height	3.05 m
	Number of blades	1
	Hub cutout	0.1 R
	Chord	150 - 200 mm
	Airfoil	S833
Aerodynamic Models	Tip loss model	On
	Hub loss model	On
	Brake state model	On
	Post-stall model	Off
	Wake Swirl	On

Table 4.2 PROPID [16] input parameters.

4.4 Structural design and fabrication

The structural design of the blade was required to incorporate the moving surfaces and strain measurement sensors in addition to providing structural integrity to the blade at high rotation speeds and loads. The structural design and fabrication method are dependent on each other. The traditional fabrication method for building wind turbine blades involves creating a mold and using fiber glass or similar composite materials. Depending on the size and expected loads on the blade, longitudinal spars and cross sectional webs made usually out of wood can be added for extra support. There are several disadvantages to this method that make it incompatible or very difficult to apply in consideration of the design requirements. It was difficult to machine the fiber glass blade to modify it to include movable surfaces. The internal blade structure is not accessible for the installation or repair of instrumentation after the completion of the blade fabrication. In addition, since the composite molding process is hand-made; the accuracy of the final product is limited by the human expertise. This was reflected on an imbalance in the rotor created by Gertz [34] since each blade was not identical. Also, the minimum thickness of the trailing edge of the blade depends on the number of fiber glass sheets used for the fiber glass composite. A different method was required to fabricate the blade with the moveable surface and instrumentation requirements.

4.4.1 3D printing

The search for an alternative fabrication method led to 3D printing. 3D printing is a rapid prototyping method where successive layers of material are placed in different shapes via robotic jets guided by lasers, the layer thickness is the main determinant of the precision of the product [52]. Although 3D printing technology has been in the literature since the early 1980s, it only became widely commercially available in 2010 [53]. Access to a relatively high quality 3D printer on-campus was a motivation to examine the capabilities of such method and explore its integration in the blade structural design and fabrication plan.

The Fortus 360mc is a 3D rapid prototyping machine made by Stratasys [54] and is one of two machines available at the UW campus. The machine is a high accuracy direct digital manufacturing system, which means that all it requires is a 3D model converted to a specific format and which is then directly printed out using the specified material. The specifications of the 3D printer outlined in Table 4.3 represent its capabilities in terms of product size and precision.

Specification	Value	Notes
Build envelope	406 x 355 x 460 mm	Maximum product dimensions
Layer thickness	0.127 - 0.330 mm	
Print precision	± 0.127mm	
Materials	PC, ABS, PC-ABS	All plastics, detailed material properties in [54]

Table 4.3 3D printer specifications [54]

There are several advantages of 3D printing that are very relevant to the design requirements of the blade. The method is capable of producing structures with:

- *Virtually any level of complexity.* This is perhaps the most significant feature of 3D printing as it enables the full freedom to design a blade with the required internal structure and moving mechanisms that meet our design requirements.

- *High precision and accuracy.* 3D printing produces of consistent and high accuracy. This enables creation of repeated identical blade components with confidence in the precision of the airfoils and compatibility of assembled components. Figure 4.2 shows a comparison between a 3D model and the printed prototype.

- *High speed.* Compared to the time required for machining, creating molds, and the application of fiber glass or similar composites, 3D printing clearly has the advantage.

- *Machine-able material properties.* The printed plastic products can be safely machined to add features or adjust dimensions without risk of fractures or other damage to the structure. The surface could also be safely grinded or sanded to the required finish.

- *No mold.* The product is built instantly without a mold. The importance of this feature comes from the ease and simplicity of making changes to the component design without a waste of resources.

71

Figure 4.2 3D model vs. photo of manufactured prototype of the blade tip section.

4.4.2 Structural design

The 3D printed plastic material had suitable properties for the aerodynamic portions of the blade including the moveable surfaces but not the structural load bearing ability. The blade design was composed of an assembly of 3D printed plastic components and simple standard shaped structural material. The 3D printed components include the aerodynamic blade sections, TEFs and tip section. The structural material include the main tubular spar, hub connectors and a control rod that activates the TEF. The complete structure was designed simultaneously and fully modelled in Solidworks® for printing and structural analysis.

4.4.3 Aerodynamic blade sections

The blade aerodynamic component was made in five core sections and an additional tip section. The sections were separately printed to fit the build envelope of the 3D printer. Two of the core sections include a TEF. The five core sections are interchangeable to allow placing the TEFs at different locations along the blade length. Figure 4.3 shows the standard core section and Figure 4.4 shows the one modified to accommodate the flap. The sections assemble to a single hollow-tube spar along the full length of the blade radius through four counter-sunk screws that fit into pre-tapped holes on the spar. The design included six cross-sectional webs that provide support against surface pressure and pitching moment (section 2.1.2.2) between the leading and trailing edge. The sections allow the flap control rod to go through them and rotate freely via a slot near the trailing edge.
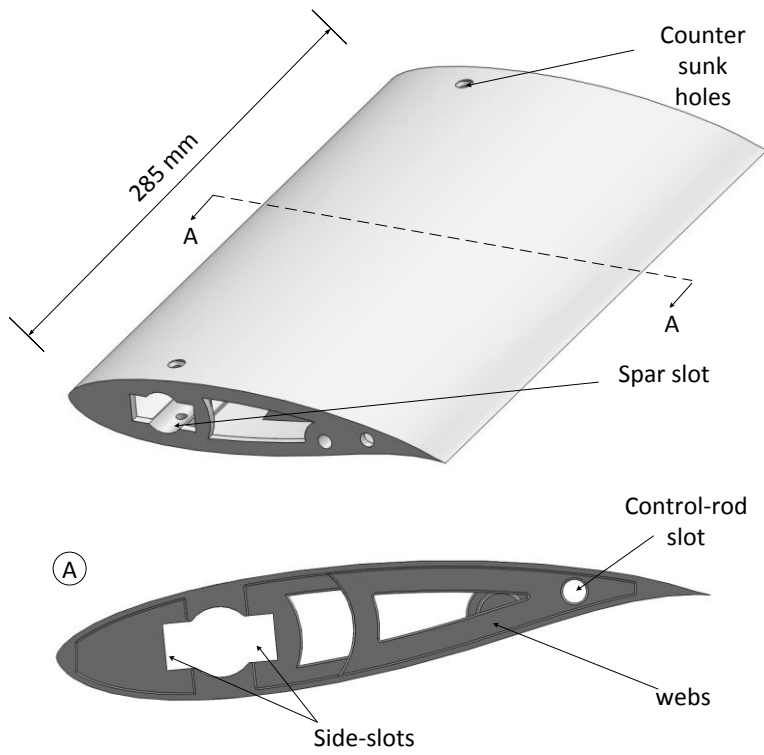
Figure 4.3 Standard blade section.
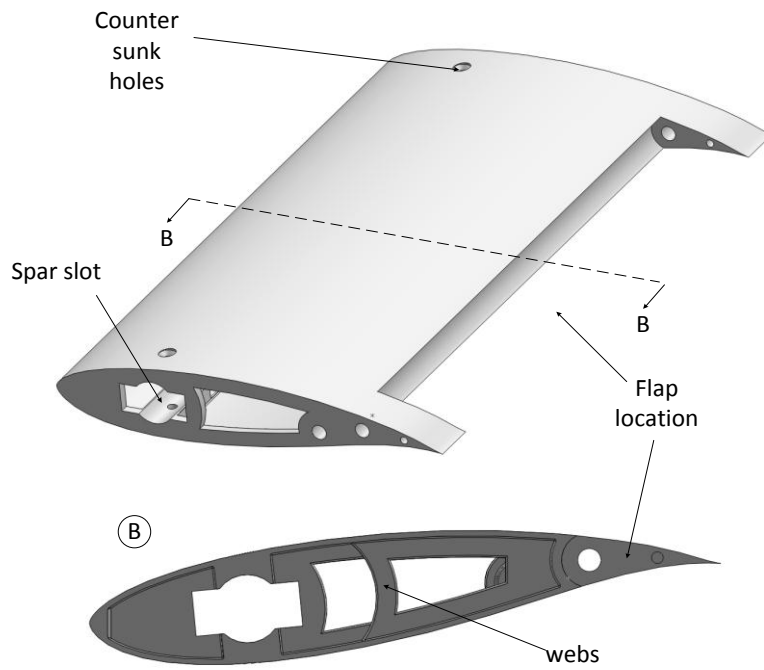
Figure 4.4 Blade flap section.

The time and cost of printing the parts were directly proportional to the volume of the material used, thus it was desirable to keep the thickness to a minimum. The main airfoil thickness was set to 1.5 mm for the outer shell, with key reinforced locations such as the webs which were set to 3 mm and the leading and trailing edges set to 5 mm. Figure 4.5 shows details of the internal design of the blade sections. Since there was no previous experience with the material or method of fabrication, a sample section was printed and manually inspected for strength and build quality before the design was approved for the full blade.
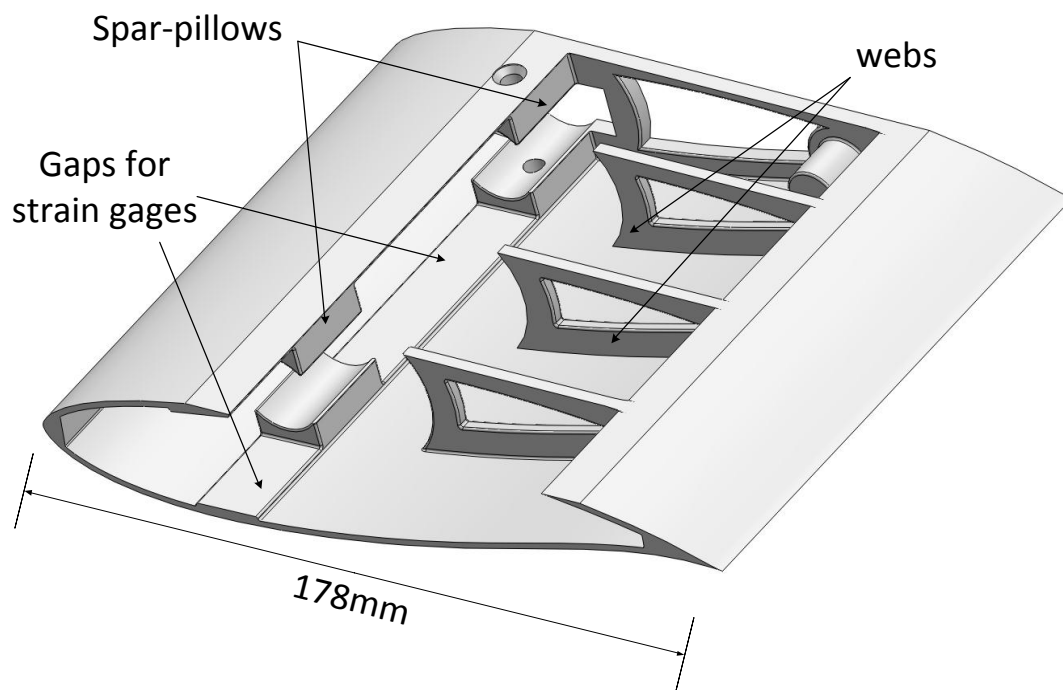
Figure 4.5 Blade section internal details.

The printed blade section attachment pillows for the spar are not continuous, they contains gaps designed for strain gages to be placed on the spar without interference from the aerodynamic components. The sides of the printed blade section where also slotted to allow swift assembly and disassembly of the components over the spar without scraping off the strain gages. This is achieved by rotating the blade section at 90° to place the side slot over the areas where the strain gages were placed and sliding them into place with the gaps above the strain gage locations, then rotating them back as illustrated in Figure 4.6. There are three possible locations for placement of strain gages safely under each of the printed sections, as shown in Figure 4.8.
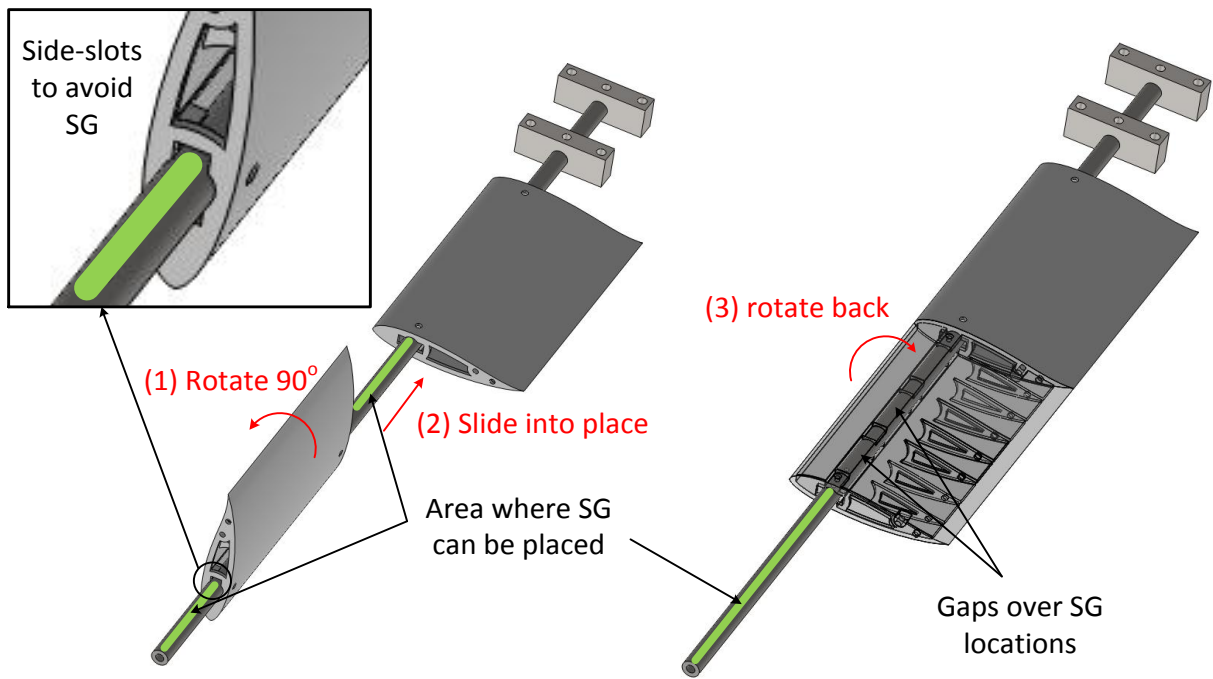
Figure 4.6 Aerodynamic blade sections assembly onto main spar.
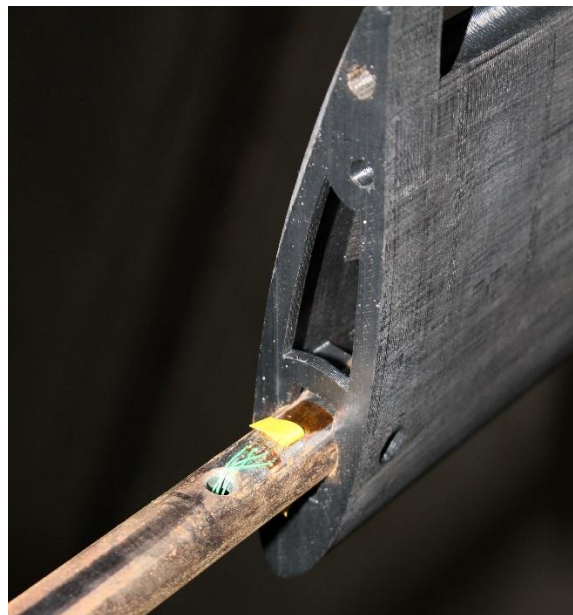
Figure 4.7 Image of blade section showing SG slots

75
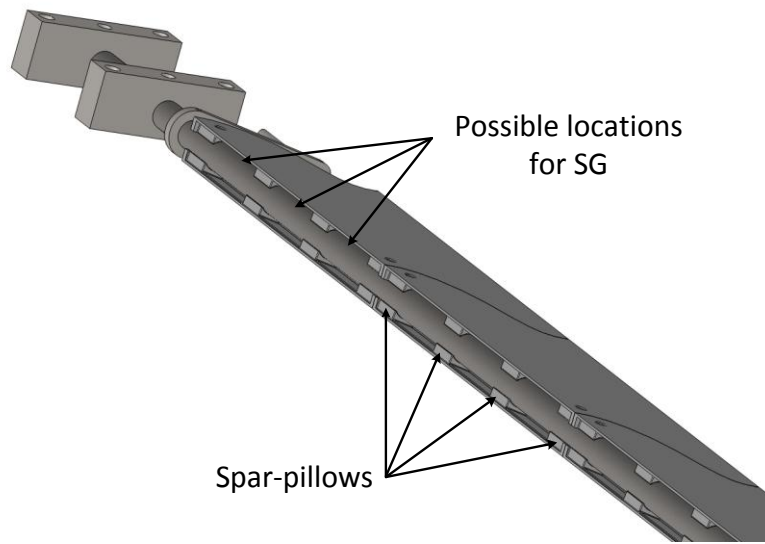
Figure 4.8 Strain gage possible locations.

4.4.4 TEFs

The TEFs were a slightly modified cut-out from the blade airfoil. They were modified to allow a wide range of rotation. The flap width covers 20% of the chord and each of the two flap lengths cover 15.5% of the blade length. The hinged trailing edge flaps are physically restricted to a deflection range of $\pm 25°$. The flaps were attached to the control rod through set screws as illustrated in Figure 4.9 and rotate along its axis. To avoid tapping the plastic, nut-inserts were designed to hold metal nuts for the set screws and are placed in slots on the trailing edge flaps.
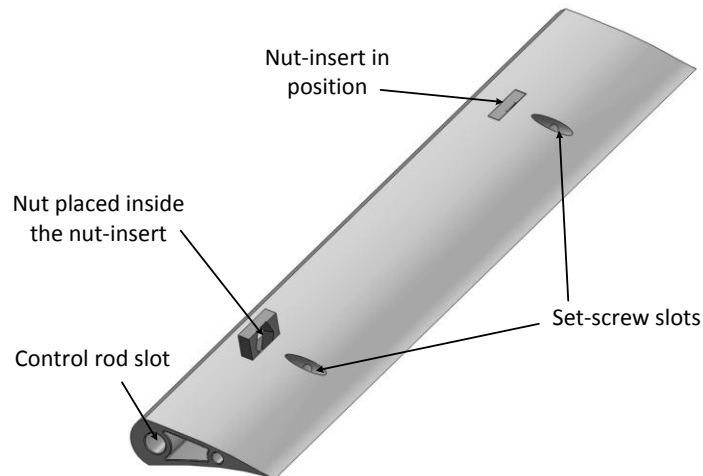
Figure 4.9 Trailing edge flap.

76

Figure 4.10 Image of printed blade flap section and trailing edge flaps.

4.4.5 Tubular Spar

The single hollow-tube spar was centered at the aerodynamic center of the airfoil (section 2.1.2), one quarter chord from the leading edge as shown in Figure 4.11. It was designed to be the only major axial load bearing component. Using a single component with a standard circular cross-section facilitates accurate instrumentation and measurement of axial load along the blade length.
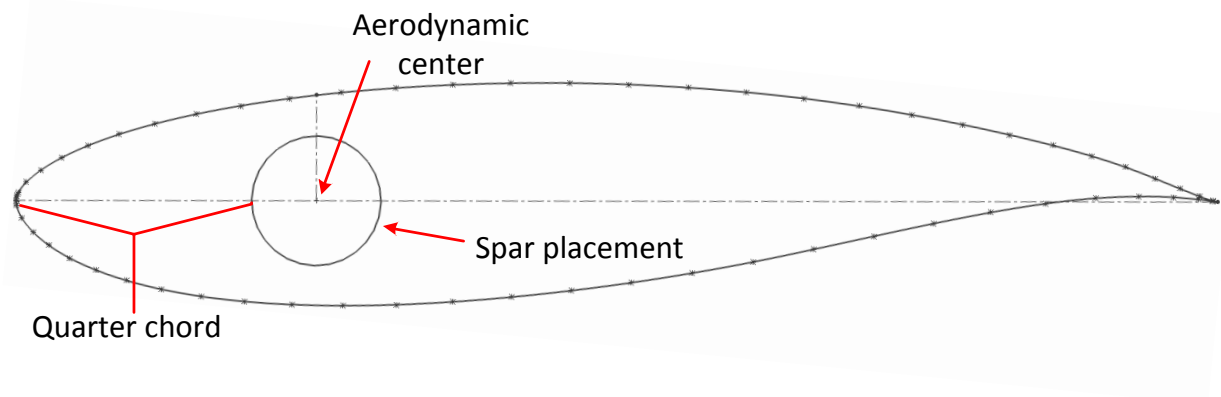
Figure 4.11 Spar cross-sectional location.

The size of the spar was restricted by the thickness of the airfoil at the aerodynamic center. Although the experiments performed in this application where steady state, the blade was designed with future dynamic testing in mind. The dynamic behavior of the rotor should reflect that of a full-scale reference wind turbine. The following equation was used for dynamic scaling [31]:

$$f_{blade} = \frac{f_{ref}\Omega_{blade}}{\Omega_{ref}}$$

4.1

where f is the first flapwise bending mode and Ω is the rotation speed. The two criteria that guided the selected spar size where the maximum load at the root and the first flapwise bending mode. The maximum deflection δ shown in Figure 4.12 was also checked to confirm that it is not excessive possibly damaging the 3D printed segments or striking the tower. The rotor axial load used for the calculations was obtained from the PROPID [16] model prediction results for the rotor performance. Since the loads were relatively low, the main factor that guided the size selection was the natural frequency. Using the Upwind 5 MW wind turbine [29] as a reference, f_{blade} was required to be 11 Hz, however, using the largest standard tube capable of fitting into the airfoil width a value of 8.5 Hz was the closest possible. The rotation speed can be reduced to acquire the ratio required in equation 4.1. A seamless tube with 19.05 mm (0.75 inch) outer diameter and 9.53 mm (0.375 inch) thickness was selected.
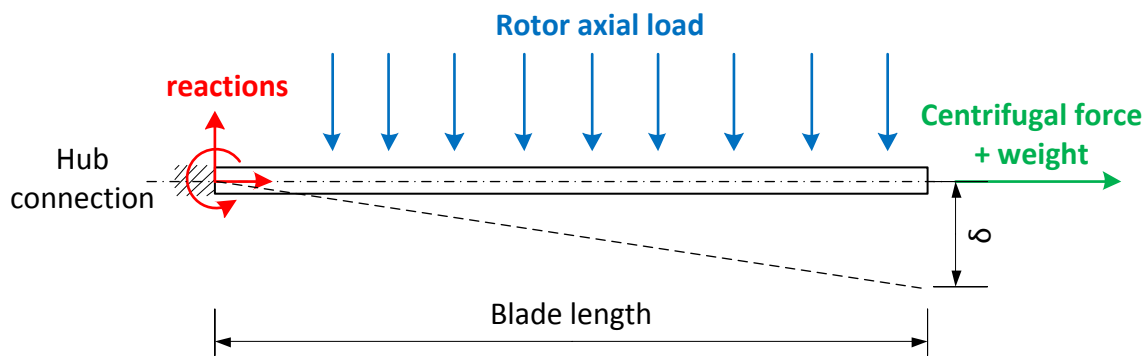
Figure 4.12 Support spar forces.

4.4.6 Hub connectors

The blade is connected to the hub via two rectangular aluminum blocks. The hub connectors are drilled with a pattern similar to the hub-plate four bolt pattern in addition to two tapped holes in the middle. The tubular spar is set to the required blade pitch and kept in position via the set-screws. A bolt is inserted into the inner end of the spar as indicated in Figure 4.13 to provide additional support against centrifugal loads.
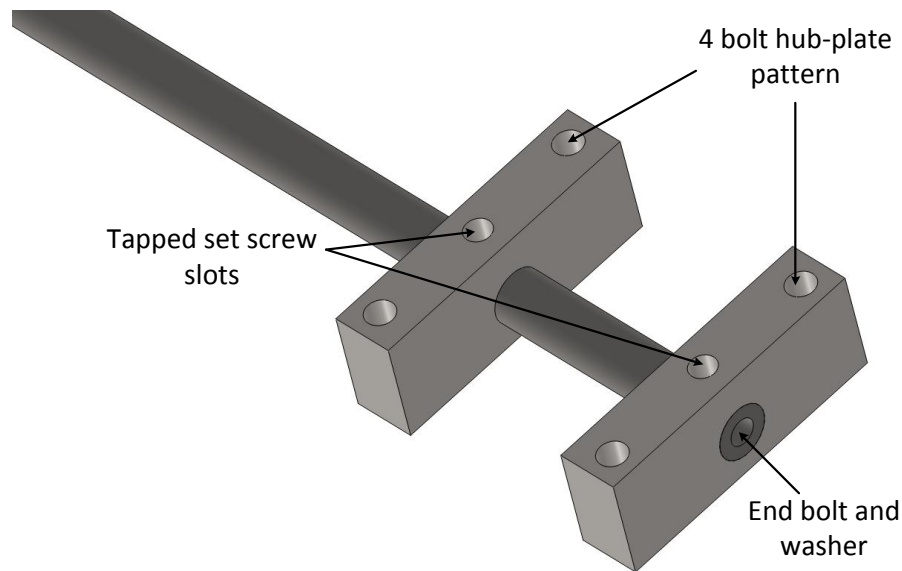
Figure 4.13 Hub attachment blocks

4.4.7 Control-rod

The flap deflection angle is modified by the control rod. For the experiments carried out in this study, the flap angle was manually set-up and held static in position by a set-screw as shown in Figure 4.14. The control rod, however, can be connected to a servo-motor for the future dynamic testing experiments. The control rod can be attached to one or both flaps at a time in order to vary the active TEF length between 15.5% and 31% of the blade length.
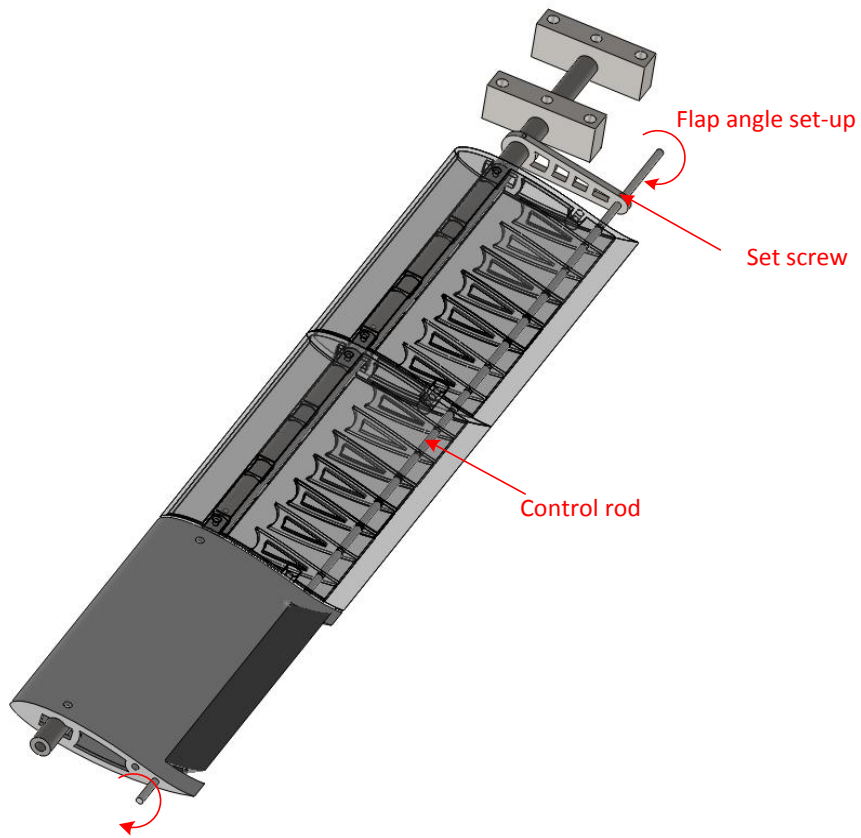
Figure 4.14 Control-rod

4.4.8 Full blade assembly

The blade design successfully met the design requirements of this study described earlier. The blade was fully assembled for this investigation by placing the segments with the TEFs in the required position based on the experimental testing plan (section 5.5). Figure 4.15 shows the fully assembled blade attached to the hub.

Michigan Scientific S8 Slip ring

High precision-low noise slip ring for data acquisition

Single Tube Spar

Single spar running through airfoil's aerodynamic center

Dynamixel® MX-64R Servo Motor

The blade design allows future attachment of a servo motor for active flap control

Blade and Tip 3D printed sections

5 interchangeable blade sections allow placement of TE flaps on different locations along blade

Trailing Edge Flaps

Simultaneously or individual activated flaps, ~ 15.5% of blade length each.

Figure 4.15. Blade and hub assembly.

4.4.9 Counter weight design and assembly

The rotor was required to be balanced to avoid excessive vibrations and loads on the hub, drive-shaft, bearings and the tower. Two cylindrical counter weights are made from the same tubular spar with a solid cylindrical weight placed at the center. They are attached to the hub to balance the rotor. The location of the center-of-mass of the fully assembled blade along its span was determined using two weigh-scales on each end. The counter weights were machined so that they have the exact same length, weight and center-of-mass location as the aerodynamic blade to have a perfectly balanced rotor. Figure 4.16 shows a comparison between the counter-weight and assembled blade.
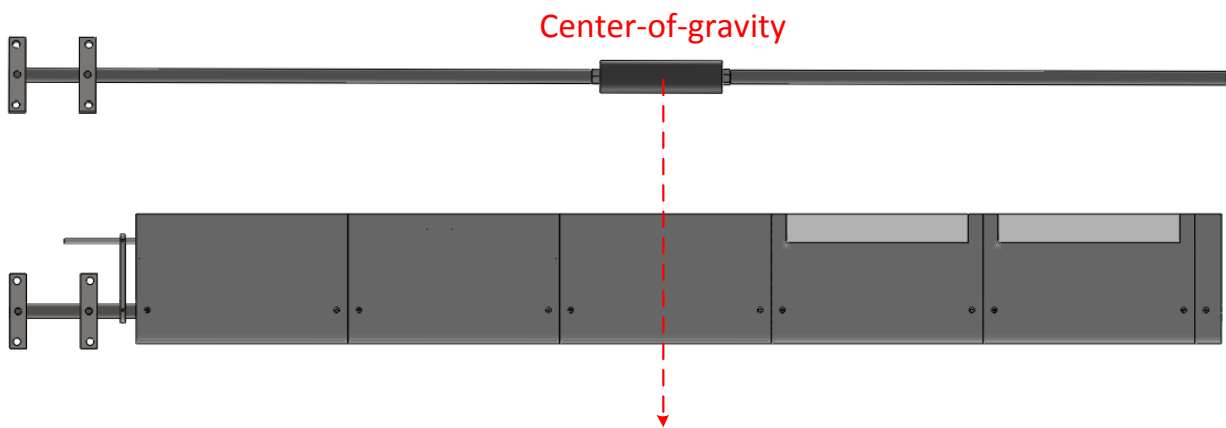
Figure 4.16 Counter-weights

4.5 Nose-cone

A nose-cone was also designed and 3D printed to stream-line the flow around the flat hub-plates. The nose-cone was designed with a removable cap to allow a cable to connect the slip-ring to the data acquisition device. Figure 4.17 shows a model of the nose-cone assembly.
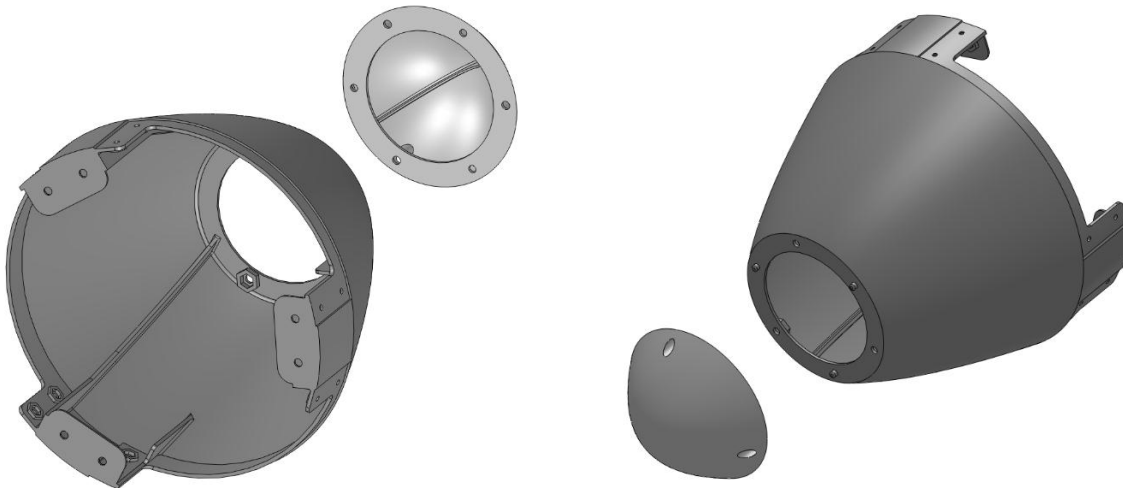
Figure 4.17 Nose-cone assembly

4.6 Final Assembled rotor specifications

The conclusion of this chapter presents the geometric specifications of the final assembled rotor along with a series of 3D models and images of the fully assembled rotor with the blade and counter-weights, and the rotor attached to the test rig. The next chapter discusses the experimental procedure.

Specification	Value	Unit
Number of blades	1 aerodynamic blade 2 counter-weights	-
Number of trailing edge flaps	2	-
Rotor radius	1.7	m
Hub cut-out	190.5	mm
Single blade (or counter-weight) mass	4967	g
Total weight (including hub)	19	kg

Table 4.4 Assembled rotor geometric specifications
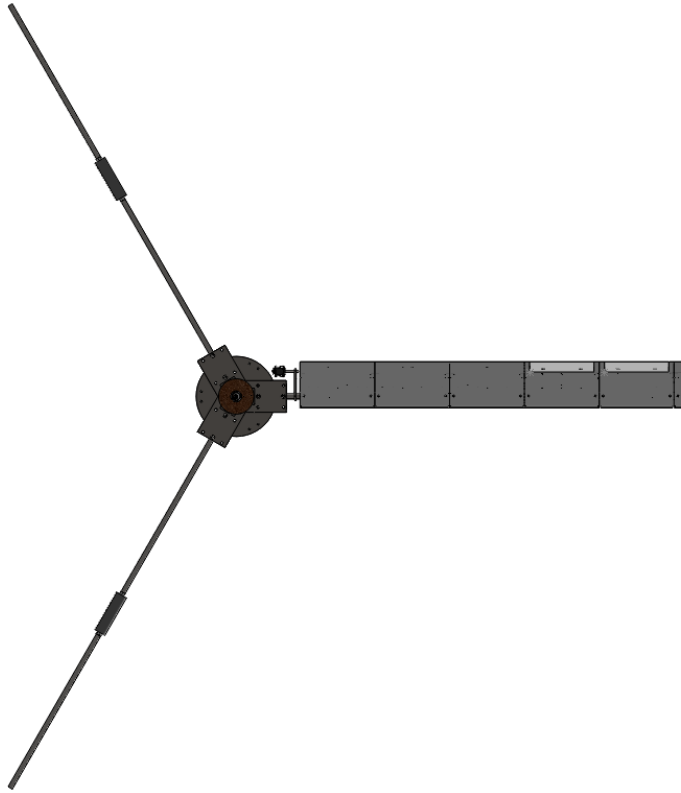
Figure 4.18 3D model and image of assembled rotor.

Figure 4.19 3D model of assembled test rig and rotor

Figure 4.20 Image of assembled test rig and rotor

Chapter 5

Experimental Procedure

This chapter describes the facility apparatus used in the experiment in addition to the test rig and rotor. It also discusses the details about instrumentation, control parameters and measurements applied in the test. Finally, the measurement points and the definitions of variables used for generating the result plots are indicated along with their sources and equations.

5.1 Facility

The UW Fire Testing wind facility was used for the experiment. The facility is an open circuit wind tunnel with a relatively large plenum, and the flow is driven by a set of six fans with limited flow conditioning. This creates an advantage since the flow has relatively high turbulence and a low blockage ratio can be obtained for test subjects. In comparison to other wind tunnels, this is a better resemblance to realistic flow conditions for wind turbines. However, the stable jet region is reduced and the flow temperature is equal to the ambient temperature and can't be controlled. Details about the facility fan specifications are in Table 5.1 and geometry details are in Table 5.2.

Specification	Value	Details
Type	Van axial fans	Howden-Buffalo Model 78-26 Series 1000 [37]
Size	1.98 m	Diameter
Number (arrangement)	6 (3×2)	-
Volume Flow rate	78.7 m^3 /s	Maximum
Pressure	413.5 Pa	At maximum flow rate
Control	VFD	Individual operation

Table 5.1 UW Facility fan specifications [37].

Area	Geometry details
Fan discharge plenum	8.23 m long, 8.54 m wide, 5.9 m high
Plenum exit plane	Rectangular 8.0 m wide, 5.9 m high
Flow Conditioning	Two settling screens and a seven across by five high array of steel flow-straightening ducts in the discharge plenum (see Figure 5.1)
Test area	15.4 m wide, 19.5 m long, 7.8 m high at the sides and 13 m high at the peak
Flow exit	Squared, 7.9 m wide, 7.9 m high

Table 5.2 UW wind facility geometry details [37].

Further details of the geometry and flow analysis of this facility may be found in Devaud *et al*. [37] and Gaunt [55]. This facility in its current configuration is capable of producing nominal wind speeds between 0 and 11.5 m/s with turbulence intensities in the range of 5.9% to 6.2% as reported by Gertz [34], representative of environmental conditions.
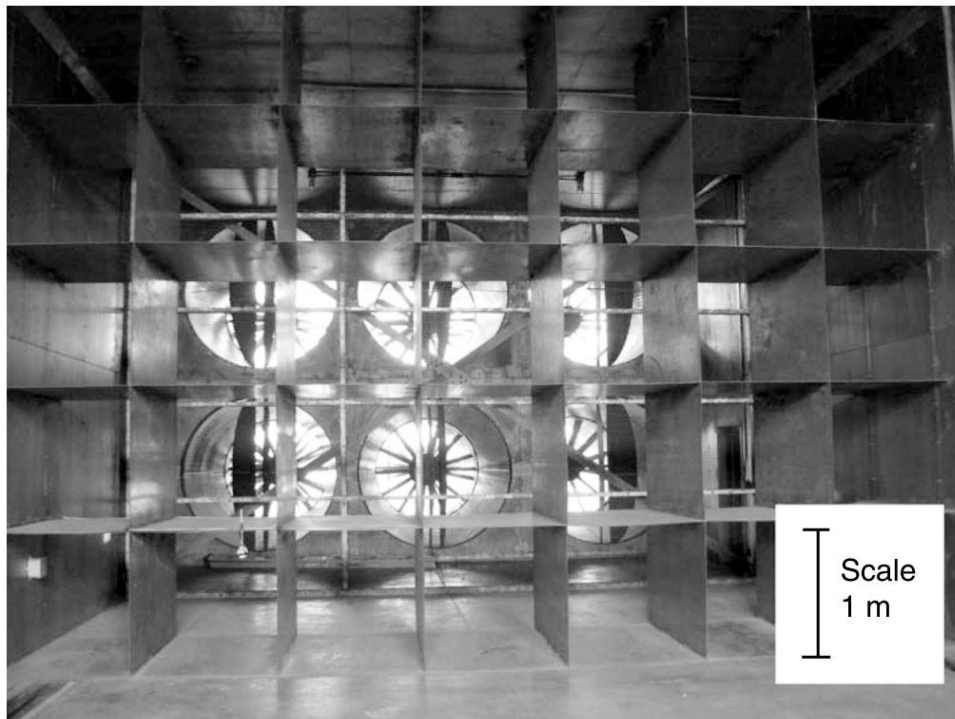
Figure 5.1 Fan discharge plenum showing conditioning screens and exit plane.
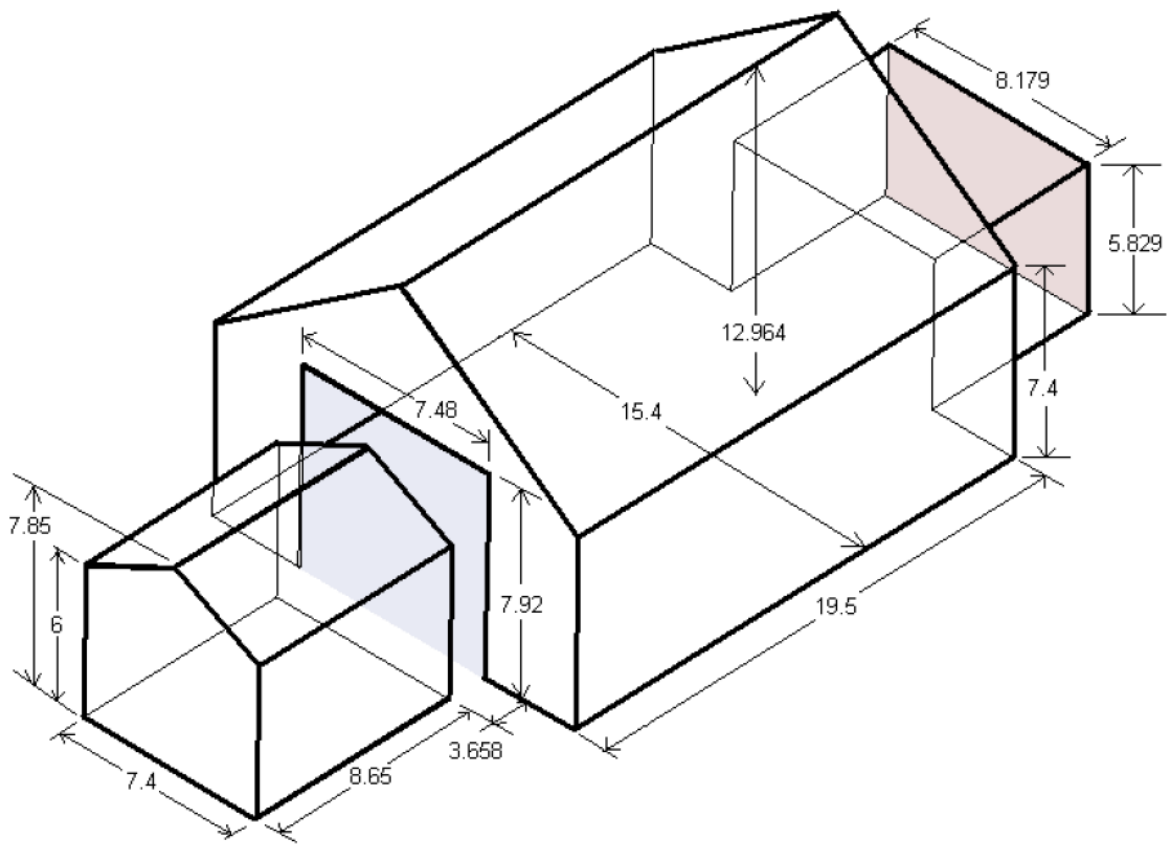
Figure 5.2 Facility geometry [38].

5.1.1 Facility Velocity Measurements.

Three measured components of velocity were obtained at the wind turbine location but in the absence of the turbine for a previous study by Johnson *et al.* [26] in the same facility. The results are shown in Table 5.3 with each velocity data set typically comprised of more than 6000 samples. Here, since the turbine is absent a Cartesian coordinate system is utilized (x, y, and z). $\overline{U}$ represents the time averaged velocity while σ represents the standard deviation (as a percentage of the mean). This table also shows that the measured standard deviation was on the same order of magnitude during all tests. Complete velocity measurements in the facility can be found in Devaud *et al.* [37] and Gaunt and Johnson [55].

Freq (Hz)	$\overline{U_x}(m/s)$	$\overline{U_y}(m/s)$	$\overline{U_z}(m/s)$	$\sigma_{U_x}(\%)$	$\sigma_{U_y}(\%)$	$\sigma_{U_z}(\%)$
30	5.59	0.19	0.07	6.38	5.21	4.70
45	8.35	0.05	0.09	6.59	5.14	4.47
60	11.13	0.06	0.13	6.66	5.31	4.33

Table 5.3 Velocity measurements over a range of fan settings obtained with the sonic anemometer.

5.2 Apparatus and Control Parameters

The apparatus consists of the wind turbine test rig and 3D printed blade described the previous two chapters and were used to set control parameters for the experiments. The wind turbine test rig's VFD provided automatic control for the rotor rotation speed to keep it constant at the 200rpm value used for all experiments in this study. It also provided the power readings through voltage and current measurements. The 3D printed blade was used to set the flap deflection angle η angle and flap formation. It was also instrumented to provide strain measurements. Table 5.4 shows a summary of the different control parameters and their properties. Measurements are discussed in more detail in the following section.

Control Parameter	Apparatus	Label	Available Range	Unit
Fan speed	Facility VFD	F_s	0-60	Hz
Rotation speed	Rig VFD	Ω	0-230	rpm
Flap deflection angle	Blade	η	0-25	Degrees
Flap center location* relative to radius	Blade	rel_f	See Table 3.1	-
Flap formation	Blade	FXX	See Figure 5.9	-

Table 5.4 Control parameters. *average center location for two flaps.*

5.3 Instrumentation and Measurements

5.3.1 Strain Measurement

The blade was instrumented with three strain gage groups along its length. The strain gages were placed directly on the steel spar using special adhesive. Each strain gauge group was made up of four strain gages wired in a full-bridge configuration and placed in on each side of the spar, Figure 5.3, to measure out of plane (flap-wise) bending moment. The strain gages used are the SGD-7/1000-DY11 precision strain gages (Omega) [56], they have a resistance of 1000 Ohms and a tolerance of ±0.35%. They were fully encapsulated and fabricated in dual packages.
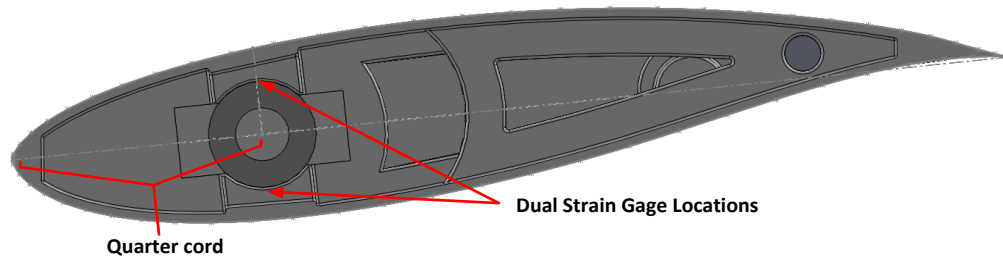
Figure 5.3 Strain gage placement on steel spar.

The first strain gage group, SG1 is placed right at the blade root 245 mm from the center of the rotor. The blade root in the rest of this report refers to the location of this first strain gage, not the center of the rotor. SG2 and SG3 are placed 770 mm and 1195 mm from the rotor center, located under section 2 and section 4 of the modular blade respectively. SG2 and SG3 were placed as close as possible to one-third and two-thirds of the length of the blade beyond SG1, limited by the availability of slots in the 3D printed sections. Figure 5.4 shows their locations relative to the 3D printed blade segments and the distance from the hub center. Wires from SG2 and SG3 run inside the hollow tube spar and exit at the hub. The data signal from the strain gages and the excitation are connected to the data acquisition system using the front mounted slip-ring. The instrumented blade was calibrated using known point loads applied at different locations along the blade, calibration is discussed in section 5.4.
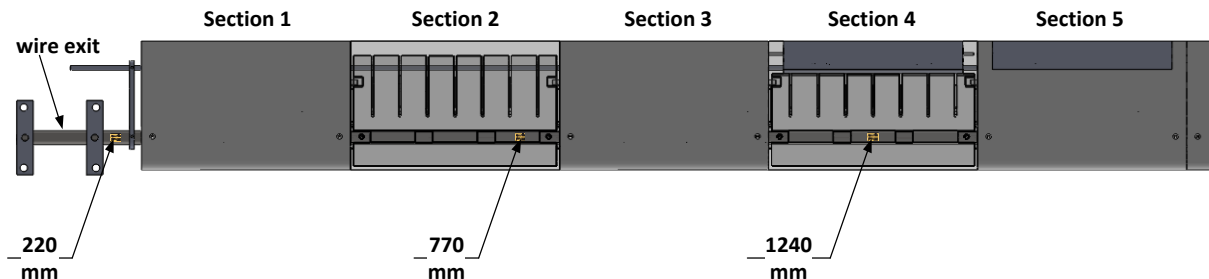
Figure 5.4 Strain gage group locations (distance indicated from center of the rotor)

91
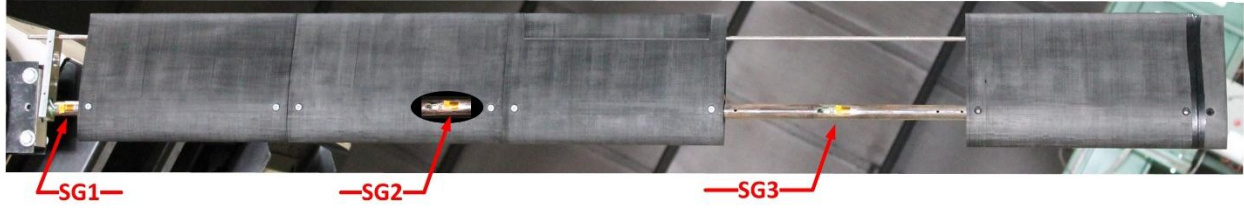
Figure 5.5. Image showing strain gage group locations.
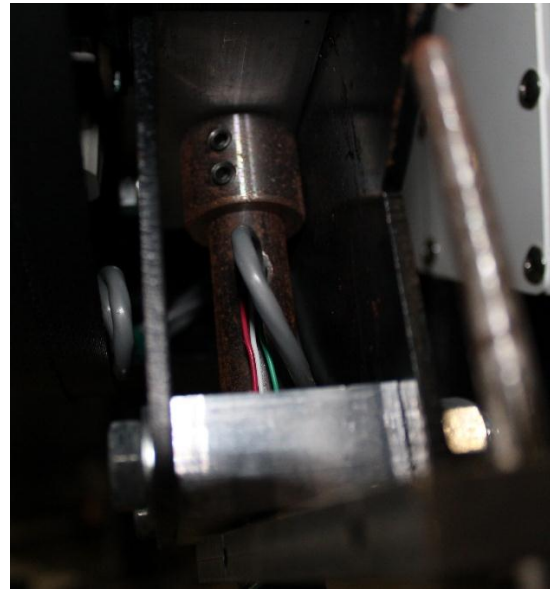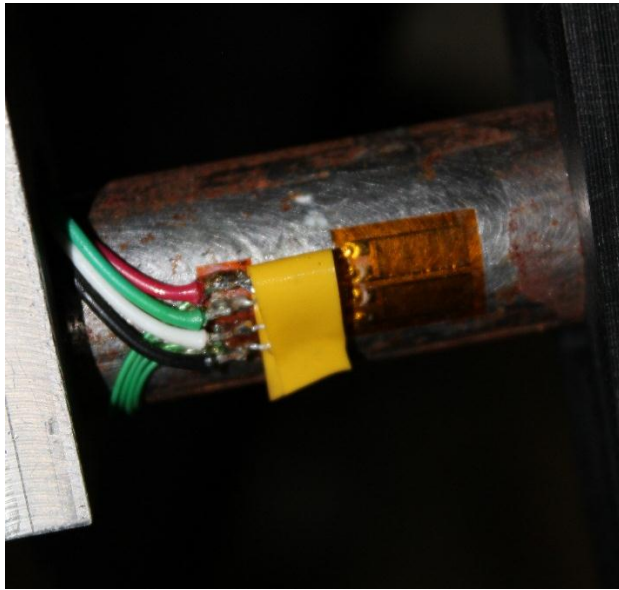
Figure 5.6. Images of the strain gage setup and wiring on the blade spar.

5.3.2 Power Measurement

Power production is measured using current and voltage measurements across the dynamic brake resistor attached to the main panel with the VFD. This is done automatically by the vector drive that controls the rotation speed at the motor. This method of measuring power production has been used in the past but is not consistent due to the varying losses along the drive-train, especially at the gearbox and motor, during operation. The losses are transient and change with temperature and operating conditions. In order to produce power measurements, testing required a great amount of repetition and averaging which consumed a significant amount of time. So, power measurements were not calculated for all measurement points. The installation of a rotary toque sensor behind the rotor, location show in Figure 3.7, is a work in progress. Using a high precision rotary torque sensor is a faster and more accurate way of measuring power production as discussed in Future section.

5.3.3 Wind Measurement

Wind speed was measurements were obtained using the CSAT-3 sonic anemometer [57] mounted on a 3m high tripod (at hub height). The CSAT-3has an offset error $<\pm 8$ cm/s and a 1 mm/s rms resolution.

10 fan frequencies were nominally chosen as measurement points for the experiments. They produced between 1.5 and 10.5 m/s wind speeds. Temperature measurements were also obtained through the sonic anemometer to ensure all experiments were carried out at the same ambient temperature. Table 5.5 shows the summary of the measurements and their properties.

Measurement	Device	Label	Unit	Sample Rate
Strain	Strain gage	σ	mV/V	1 kHz
Power	Rig VFD	P	W	1 kHz
Wind Speed	Sonic Anemometer	W	m/s	20 Hz
Temperature	Sonic Anemometer	T	^{O}C	20 Hz

Table 5.5 Measurements Summary

5.4 Calibration Procedure

The strain gages were calibrated using known loads applied at specified locations. The completed blade was fastened to a clamp at the location where the hub attachment would be during operation. Three sets of calibration tests were performed using loads from 454 to 1814 g (1 to 40 lbs.), Table 5.6 shows the distance between each strain gage group and the applied load for each calibration test.
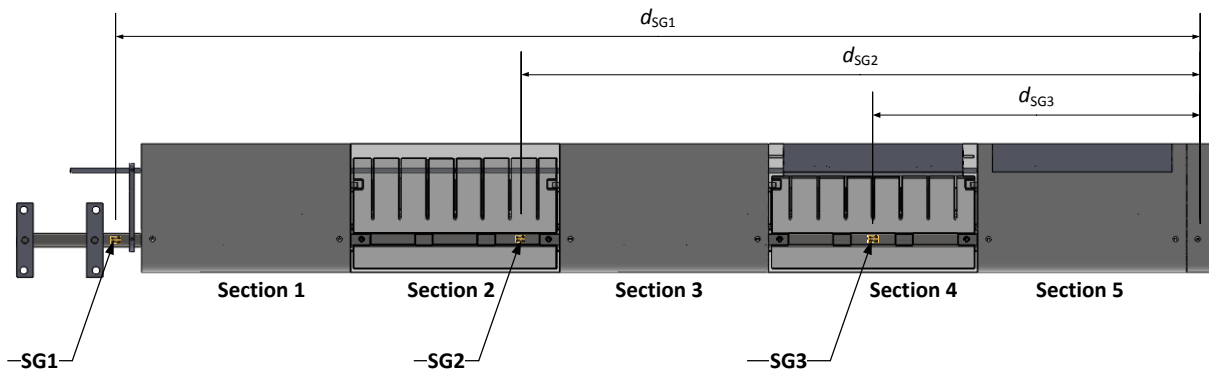
Calibration Test	d_{SG1} (mm)	d_{SG2} (mm)	d_{SG3} (mm)
1	1440	901	417
2	940	400	-
3	470	-	-

Table 5.6 Calibration test load locations

The strain gage reading is directly proportional to the stress at the surface of the spar where the measurements they are placed. The strain gage reading can be represented as:

$$R_{SG} \propto \sigma_\beta \qquad\qquad 5.1$$

$$R_{SG} = C_{SG}\sigma_\beta \qquad\qquad 5.2$$

where R_{SG} is the strain gage reading and C_{SG} is the strain gage constant. Recalling equation 2.42 (5.3 below), stress on the surface is a function of the moment at that spanwise location M_β, the spar outer radius c and the area moment of inertia of the cross section I_b. Combining equations 5.2 and 5.3 yields an equation that relates the strain gage reading to the moment at the strain gage location:

$$\sigma_\beta = M_\beta c / I_b \qquad\qquad 5.3$$

$$R_{SG} = C_{SG} M_\beta c / I_b \qquad\qquad 5.4$$

Since the spar cross-section is constant along the span for all strain gage groups, c/I_b can be combined with C_{SG} into one constant K, so that:

$$R_{SG} = KM_\beta \qquad\qquad 5.5$$

where K is a constant equal to $C_{SG}c/I_b$. The calibration test was performed to calculate the constant K using the known loads and locations, then using regression analysis to fit a linear trend such that:

$$R_{SG} = KM_\beta + b_k \qquad\qquad 5.6$$

where b_k is the bias error from the strain gage group. K was expected to be similar for all strain gage locations. It was then used to calculate the measured moment from the strain gage readings by rearranging equation 5.5:

$$M_\beta = \frac{R_{SG}}{K} \qquad\qquad 5.7$$

The calibration outcome is reported in the following Results and Discussion section.

5.5 Experimental Procedure

The experimental procedure involved three stages, warm-up, setup and measurement. The warm-up step was significant since the experiment was performed in winter months. Detailed steps of each stage are outlined below.

1] **Warm-up.** The first stage involved an initial warm-up by increasing the rotational speed of the rotor up gradually towards the 200 rpm required value and keeping it running constant for 20 mins. The facility fan speed was then increased to the maximum 60 Hz. The warm-up was repeated between experimental setups for 5 mins.

2] **Setup.** The second stage involved setting the required flap parameters.

   - The blade segments were slid onto the spar (as described in section 4.4.3) in the order required by flap formation, Figure 5.7 shows an image of a blade section sliding into position.

   - The length of the blade flap to be modified was set using set screws that connect the TEF to the control rod as

   - The flap deflection angle η was set using a digital protractor measuring the angle through the turning of the control rod, Figure 5.8 shows an image of flap with a negative η.

   - The rotation speed Ω was set to 200 rpm on the control panel.

3] **Measurement.** The final stage involved recording the strain gage readings, power measurements and wind speed measurements using a pc. The facility fan speed F_s was increased by 5 Hz increments, starting at 10 Hz and ending at 60Hz while the rotor was running constantly.

Stage 2 and 3 were repeated for different combinations of flap length, location and angle. Figure 5.9 shows the different flap formations applied in this study and gives each a code that will be referred to in the results section. Table 5.7 shows the different measurement points for the flap formations. All tests were performed in an ambient temperature of -10°. A negative flap pitch angle is towards the suction side (see section 2.1.7).

Figure 5.7. Image showing flap section sliding into position.
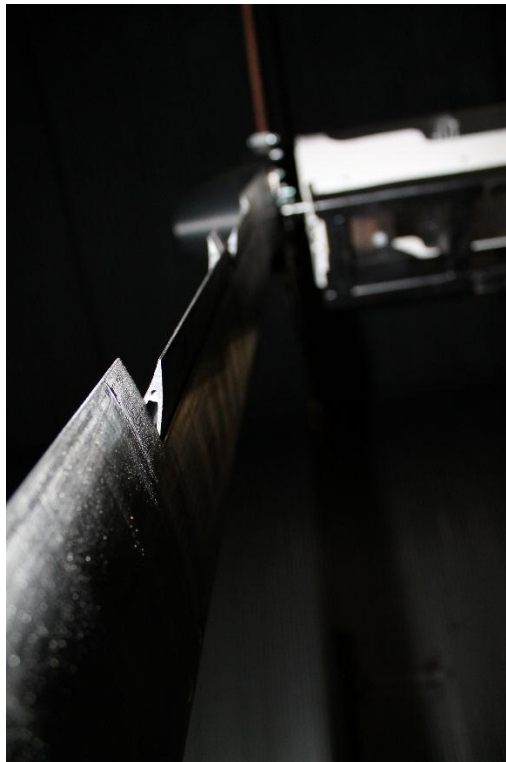
Figure 5.8. Image showing flap at a negative deflection angle.

The different flap formations were coded to simplify identification. Starting with 'F' followed by the number *1* or *2* and one of the letters *A*, *B*, or *C*. The number indicates the number of flaps activated hence the effective length of the flap. F1*X* indicates 15.5% while F2*X* indicates 31%. The letter indicates the distance of the flap from the hub (or the average distance if two flaps are activated). *A* being the furthest away and *C* being the closest to the hub. The coding scheme and equivalent formations are illustrated by the schematic in Figure 5.9. It also shows the approximate locations of the three strain gage groups, SG1, SG2 and SG3. The exact locations are shown in Table 5.9.
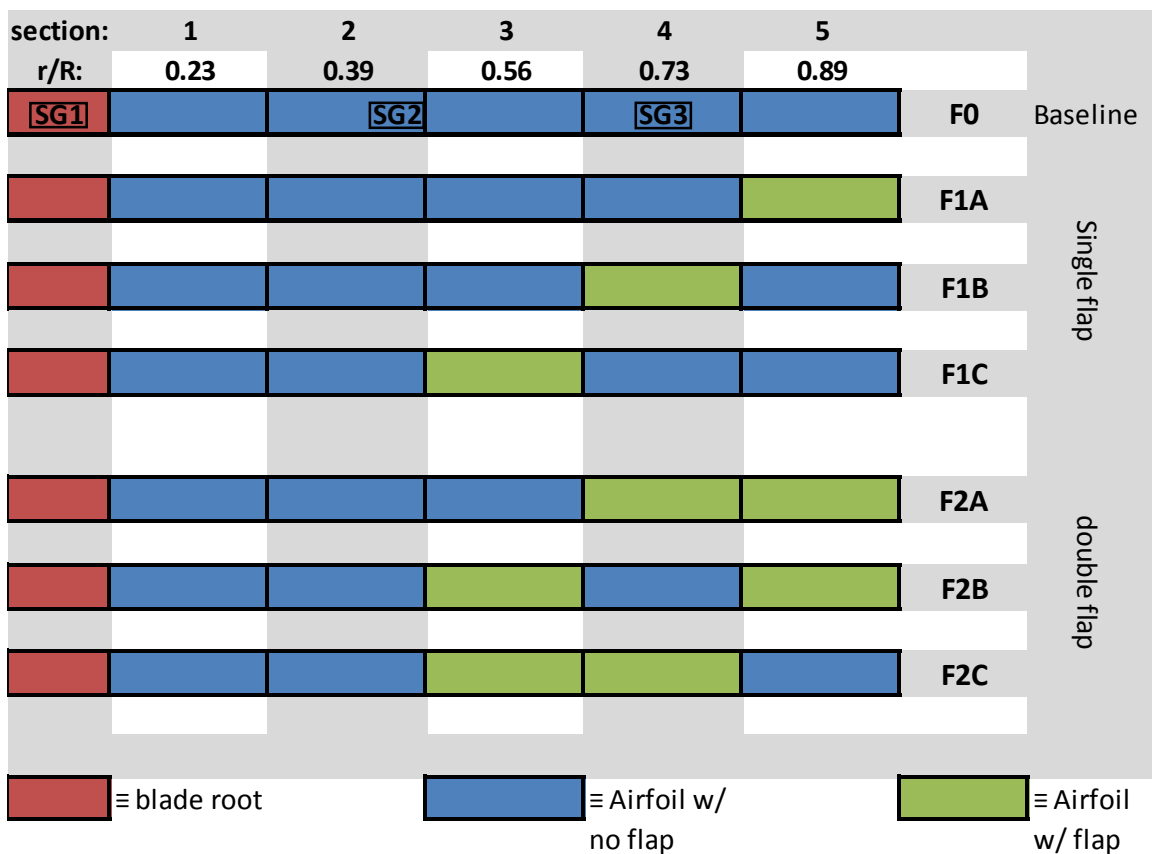
Figure 5.9. Schematic identifying different flap formations (Fxx) and strain gage group (SGx) locations.

Each section length = 285mm.

Flap formation	Flap angle η	Flap relative location rel_f	Fan speed F_s (Hz)
F0* (baseline)	0	-	10 – 60 (increments of 5 for all cases)
F1Aψ	-15	0.89	10 – 60
F1Bψ	-15	0.73	10 – 60
F1Cψ	-15	0.56	10 – 60
F2Aψ	-15,-10,-5, 5,10,15	0.81	10 – 60
F2Bψ	-15	0.73	10 – 60
F2Cψ	-15	0.65	10 – 60

Table 5.7 Measurement Points, *power included for all velocities, ψpower only at design velocity.

5.5.1 Data Recording and Processing

Strain, power and wind speed data were collected by the same computer using separate software for each reading. The recording process was manually triggered and runs for a 20 s period. The data recording was not synchronized due to the manual triggering. This did not affect this study since all the measurements were time-averaged. Table 5.8 summarizes the properties of the acquired data sets.

Raw strain data was collected by an NI-9237 data acquisition card (National Instruments) [58] and converted from analog into digital readings. It was then compiled into a single file from all three strain gage group in a tab-delimited format with each column representing one of the groups. The data was time-average to produce a single value from each set then a subtraction/addition process was performed to offset the zero error. Power data was time-averaged and repeated due to the variable error caused by the drive-train losses discussed in section 5.3.2. The values produced were averaged again.

The freestream wind velocities in the axial, radial and vertical directions respectively were measured periodically during the experiments for each fan frequency set. The wind speeds were collected in 30 sec periods with a 20 Hz sample rate and averaged. The wind speed data was also time-averaged and repeated for the same conditions, and then the data set values were averaged again.

Data	Acquisition Software	Format	Processing*
Strain	Labview® (National Instruments)	3 column, tab delimited, text file	time-average, zero-offset
Power	CT-Scope (Control Techniques)	1 column, text file	time-average, data set average
Wind Speed	CSAT32 (Campbell Scientific)	3 column, text file	time-average, data set average

Table 5.8 Recorded Data Format and Processing. *processing was done using MATLAB® software.*

5.5.2 Data plotting

Some of the operational parameters and measurements were modified for producing comparable and meaningful plots. Each strain gage group measured the moment along the blade span at the position of the group center (using equation 5.7 in section 5.4), the radial and normalized locations of the strain gage groups are in Table 5.9.

The moment M_r was plotted with reference to the location of the measurement. To show the moment distribution within the blade at different flap and operation parameters the moment was normalized relative to the root value (measured by SG1) for the same case and labelled R_{M_r}. To quantify the moment reduction or increase compared to the baseline case $\%M_r$ and ΔM_r were used to represent the percentage change and increment change respectively. Table 5.10 summarizes the mentioned and all other parameters (both modified and unmodified) used in the plots reported in the following chapter and equations used for the modifications.

Strain gage group reference	Radial location r	Normalized Radial location r/R
SG1	0.220 m	0.13
SG2	0.770 m	0.45
SG3	1.240 m	0.73

Table 5.9 Measurement radial locations.

Symbol	Representation	Unit	Equation	Details
M_r	Moment measured at radial position r	Nm	$M_r = M_\beta$	$r_{SG1} = 0.22m$ (blade root) $r_{SG2} = 0.77m$ $r_{SG3} = 1.24m$
R_{M_r}	Normalized moment relative to root value for the same formation	ratio	$\dfrac{M_r}{M_{r_{SG1}}\ (root)}$	Used for showing changes in moment distribution
ΔM_r	Value change in M_r from the baseline case F0	Nm	$M_r - M_{r\ (baseline)}$	
r/R	Normalized radial position	ratio	$\dfrac{r}{R}$	
rel_f	Flap center location relative to the blade length	ratio	(unmodified)	
η	Flap deflection angle	degrees	(unmodified)	
Power	Power generated	W	(unmodified)	
W	Freestream wind speed in the axial direction	m/s	(unmodified)	

Table 5.10 Measurement parameters naming and equations.

Chapter 6

Results and Discussion

This section outlines the qualitative and quantitative results of the calibration and experimental work. The baseline performance of the blade is compared to the BEM prediction to validate the blade design. Measurements for the various TEF parameters (location, length, and angle) described in the previous section are presented and compared to the baseline case. The significance, implications and possible improvements of the results are discussed.

6.1 Qualitative Results

6.1.1 Rig Performance

The performance of the newly designed and assembled rig is an important finding of this study that is not necessarily reflected in the data sets. The performance was measured against qualitative references that were set as design requirements.

Geometry and Instrumentation

The nacelle components and frame size made it possible to build an aerodynamic nacelle cover that did not extend beyond the average non-aerodynamic hub portion of the blade length. This is an important feature that makes it feasible to perform more accurate local wind speed measurements behind the rotor plane that were previously altered by interference from the large nacelle. Johnson *et al.* [26] discusses the negative effects of the large nacelle on such readings. Also, the monopole tower configuration for the turbine support is similar to modern turbines. It allows the utilization of strain gages at the root of the support to measure loads on the full turbine.

Speed Control

The rotation speed feedback from the motor encoder displayed the actual rotor speed consistently within ±1m/s from the input speed throughout the range of operation. The VFD controller effectively kept the speed constant as the freestream wind velocity was changed for the complete range of possible wind speeds. This is critical for experiments that study the dynamic response of the wind turbine system or any of its

components to changes in the operating conditions and was one of the requirements of this system that was successfully met.

Power Measurement

The power measurement for this experiment depended on voltage and current measurements over the dynamic brake resistor where the power is dissipated. This method is affected by the losses in the drive-train which have proven to be transient and change with temperature and duration. Power readings in this study have been repeated and averaged several times to minimize the transient effect of the drive-train loss, while the system was run with no rotor attached to calculate the mean losses. This method has similar disadvantages to the previous rig as described in section 3.1, however, assembling a torque sensor right behind the blade in the location shown in Figure 3.7 is a work in progress, as discussed in Future work section.

6.1.2 3D Printed blade structural integrity

The modular blade created from a single spar bearing the majority of the structural load and coupled with 3D printed plastic aerodynamic sections was a novel way to build a test blade. It had significant advantages in terms of the possibilities of customization and instrumentation. Although the blade involved several smaller assembled components and moving parts, it proved to be strong enough to withstand the operational conditions during the initial testing and all components remained intact at the highest rotation speed. This was very important to the success of the rest of the study. The control rod system was also successful in keeping the flap angle constant at the high rotation speeds during the experiment.

6.2 Strain gage calibration results

All three strain gage groups showed a linear response to the known loads with consistent and similar gradients for all trials within the full range, as expected. The strain gage constant K (see equation 5.6 in section 5.4) was calculated for all sets using a linear fit. The bias error was very low indicating that the strain gage application was accurate and the measurements they produced were repeatable (uncertainty calculations in Appendix E). The results for three sets of calibration tests are shown in Table 6.1. The full data sets are in Appendix C.

F_i (N)	R_{SG1} (mV/V)	$M_{\beta 1}$ (Nm)	R_{SG2} (mV/V)	$M_{\beta 2}$ (Nm)	R_{SG3} (mV/V)	$M_{\beta 3}$ (Nm)
4.5	0.049	6.408	0.030	4.0095	0.014	1.8557
8.9	0.095	12.816	0.060	8.0189	0.027	3.7113
13.4	0.144	19.224	0.090	12.0284	0.040	5.5670
17.8	0.193	25.632	0.120	16.0378	0.053	7.4226
22.3	0.238	32.04	0.148	20.0473	0.066	9.2783
31.2	0.334	44.856	0.207	28.0662	0.092	12.9896
40.1	0.430	57.672	0.268	36.0851	0.118	16.7009
44.5	0.480	64.08	0.300	40.0945	0.132	18.5565
62.3	0.674	89.712	0.419	56.1323	0.185	25.9791
75.7	0.810	108.936	0.505	68.1607	0.224	31.5461
89.0	0.960	128.16	0.595	80.1890	0.264	37.1130
106.8	1.150	153.792	0.715	96.2268	0.315	44.5356
115.7	1.195	166.608	0.745	104.2457	0.327	48.2469
124.6	1.293	179.424	0.800	112.2646	0.353	51.9582
133.5	1.439	192.24	0.893	120.2835	0.392	55.6695
142.4	1.533	205.056	0.952	128.3024	0.418	59.3808
160.2	1.675	230.688	1.040	144.3402	0.456	66.8034
169.1	1.800	243.504	1.120	152.3591	0.495	70.5147
Linear analysis	$R_{SG} =$ $0.0073 M_{\beta 1} + 0.0038$		$R_{SG} =$ $0.0073 M_{\beta 2} + 0.0054$		$R_{SG} =$ $0.0069 M_{\beta 3} + 0.0022$	

Table 6.1 Calibration results for tip applied load, $*d_1 = 1.44$m, $d_2 = 0.901$m, $d_3 = 0.417$m

6.3 Wind Speed Measurements

The fan frequencies were initially set up as a control parameter since the wind speed could not be directly controlled. Wind speed measurements converted the fan frequencies to enable plotting meaningful results. The wind speed was logged in three-dimensions using the sonic anemometer. The wind speed of interest was the axial freestream wind speed W. The time-averaged values for each set are reported in Table 6.2 as W_i, where i indicates the data set number. W is the average of the values from each data set and was used in all the following plots. The facility operated at its maximum 60 Hz fan speed produced irregular and inconsistent wind speeds reflected in the high standard deviation and these results were discarded from the reported results.

Fan Frequency (Hz)	W_1 (m/s)	W_2 (m/s)	W_3 (m/s)	W (m/s)	σ_W (m/s)
0	0.00	0.00	0.00	**0.00**	0.00
10	1.77	1.74	1.55	**1.69**	0.08
15	2.78	2.70	2.72	**2.73**	0.03
20	3.81	3.67	3.61	**3.70**	0.07
25	4.54	4.58	4.62	**4.58**	0.03
30	5.52	5.68	5.60	**5.60**	0.06
35	6.38	6.41	6.57	**6.46**	0.07
40	7.46	7.35	7.42	**7.41**	0.04
45	8.53	8.55	8.60	**8.56**	0.03
50	9.48	9.42	9.48	**9.46**	0.02
55	10.44	10.48	10.42	**10.45**	0.02
60	11.61	11.33	11.73	**11.56**	0.15

Table 6.2 Test Wind Speeds

6.4 Baseline Blade Performance

The baseline case represents the operation of the blade with no TEFs activated. It is used as a reference for comparison for the effects of modifying the flap parameters.

6.4.1 Power Readings

The baseline performance was first compared to the prediction by the PROPID [16] (section 4.3) in Figure 6.1. The experimental measurements show slightly higher values than the model at the lower half of the wind speed range and the prediction seems to be increasingly higher beyond 7 m/s. The BEM prediction is only an approximation for the performance of the wind turbine blade.
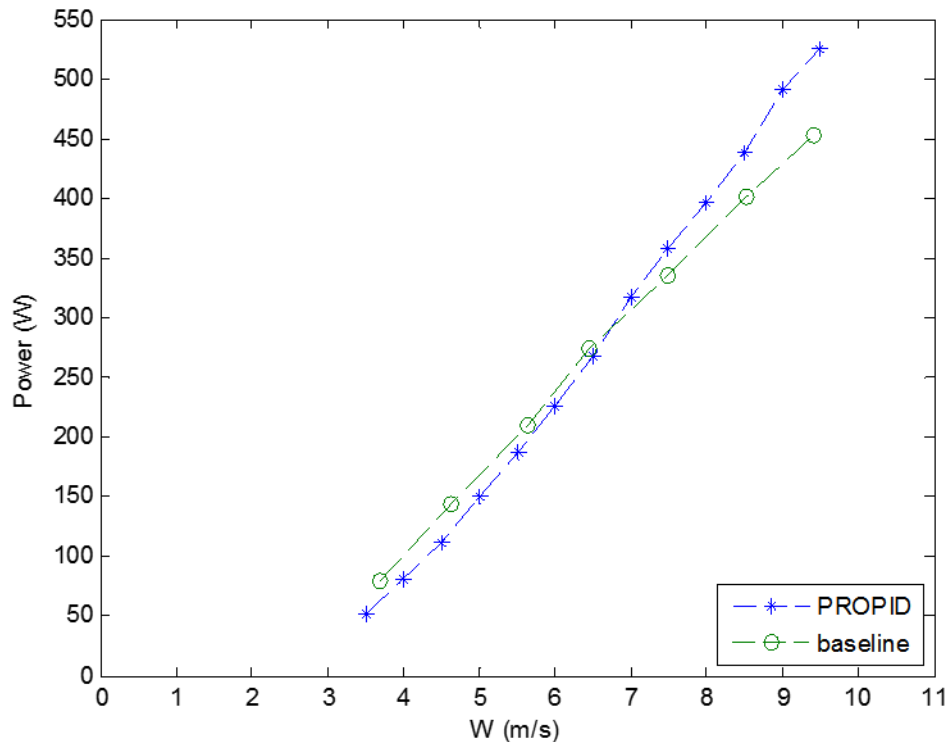
Figure 6.1. Power vs. Wind speed (W) for the baseline case compared to

PROPID [16] predictions.

The differences, although relatively small, can possibly be attributed to the existence of a radial velocity component creating an interaction between blade segments contrasting one of the BEM assumptions (see section 2.1.3.1). Also, the PROPID [16] input defines a single bladed rotor to simulate the blade performance and does not account for the effects of the cylindrical counter-weights which are part of the experimental rotor. However, the difference between the model and experiment was relatively low and not unusual, and Johnson *et al.* [26] reported similar differences between the experimental performance

measured through two completely different approaches and the model predictions for a full three-bladed rotor and noted similar variations. The 3D printed aerodynamic segment of the blade was accurate to ±0.0125 inch according the 3D printer specifications (as discussed in section 4.4.1) and validated through physical measurement. Hence, for the rest of the results, the aerodynamic effects of the cylindrical counter weight were assumed to be negligible and the airfoil geometry was assumed to be of high precision.

The α distribution showed relatively high angles near the blade root, as shown in Figure 6.2, due to the lack of twist in the blade aerodynamic design. The first 30% of the rotor was probably stalled for winds speeds of 6.5 m/s and above. The contribution to power production and blade load due to lift from this section is not considered significant for wind turbine blades in general.
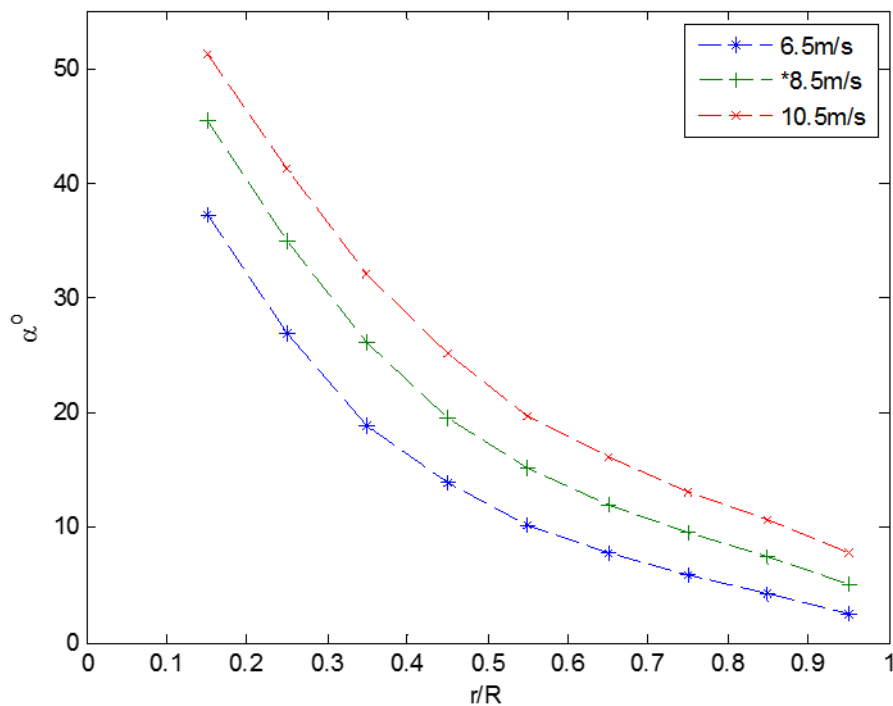
Figure 6.2. PROPID angle of attack distribution. *design speed*.

6.4.2 Strain Gage Readings

Since the blade support configuration is similar to that of a cantilever, the reading by each strain gage group (SGX) represents the moment caused by the cumulative differential thrust forces acting on the blade elements between the measurement point and the blade tip. Differential force contribution to moment was discussed in section 2.1.5.2 and is shown for SG3 as an example in Figure 6.3. Hence, changes to the airfoil characteristics, or flow conditions for the elements between the measurement point and blade tip were expected to affect the moment value.
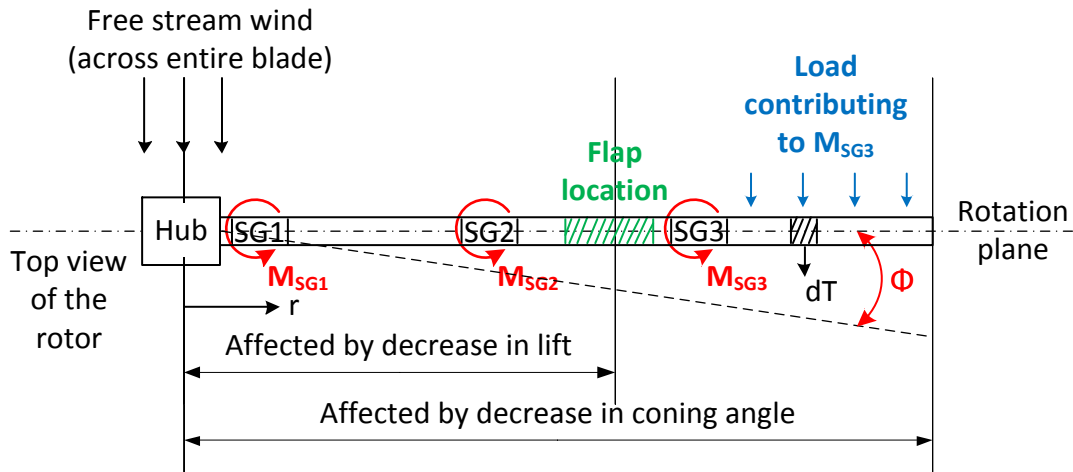
Figure 6.3. Force contributing to moment reading at SG3.

Moments were used rather than forces to represent load distribution on the blade. The fluctuation in moment at the root of the blade (near the hub) is the quantity commonly used in literature as discussed in section 2.2 to calculate the reduction in damage equivalent loading for both simulation and experimental studies on TEF. The quantities listed and described in Table 5.10 in section 5.5.2 were used to represent the data sets.

Figure 6.4 shows the change in moment values with respect to the wind velocity. The trends were very similar to the bending moment measurements performed at two radial locations (r/R=0.2 and r/R=0.65) on the MOD-2 wind turbine [21] shown in Figure 2.15. This trend is clearly the result of more blade segments contributing to the moments measured closer to the hub (lower r/R values). Also, the axial force is distributed along the blade usually increasingly towards the end of the blade radius as shown in the modelled load distribution in Figure 2.12 in section 2.1.5. The bending moment was also shown to be continuously increasing with wind speed and it is apparent that it does not reach the point where the majority of the blade stalls within the wind speed range. The error was not significant based on the large size of the population and the small strain gage bias error, thus it was not shown on these plots. Appendix E shows the calculations of uncertainty for the derived parameters and an error bar plot for the data in Figure 6.4.

The plot shows a negative moment for the initial range of wind speeds. This indicates that the axial force was acting in the opposite direction. This agrees with the C_l trend where a negative lift is initially experienced for cambered airfoils at negative α. The initial negative α is the result of the 6° blade pitch and rotation of the rotor. Figure 6.5 shows α at the mid-span of the blade throughout the wind speed range calculated using equation 2.22 in section 2.1.3 without the effect of the induction factors. Measuring the induction factors was beyond the scope of this study.
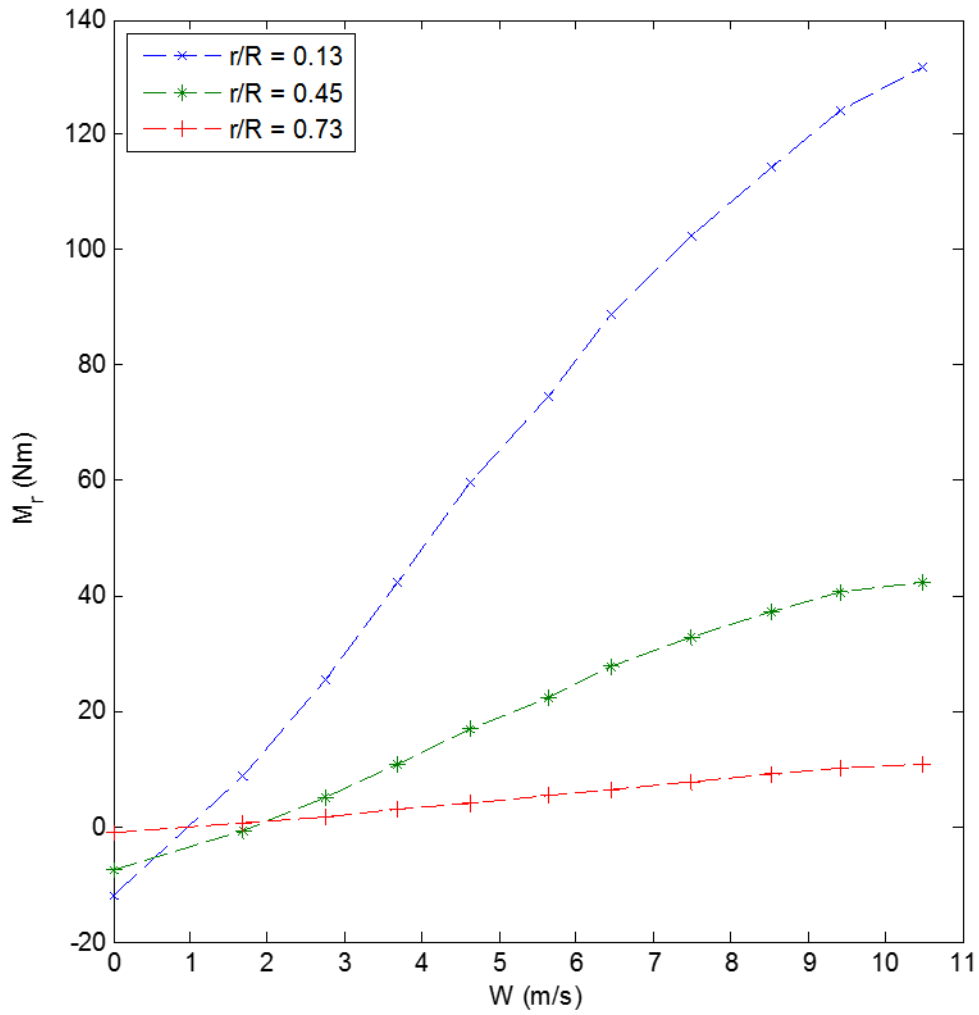
Figure 6.4. Moment (M_r) vs. Wind speed (W) measured at each radial position for the baseline case.
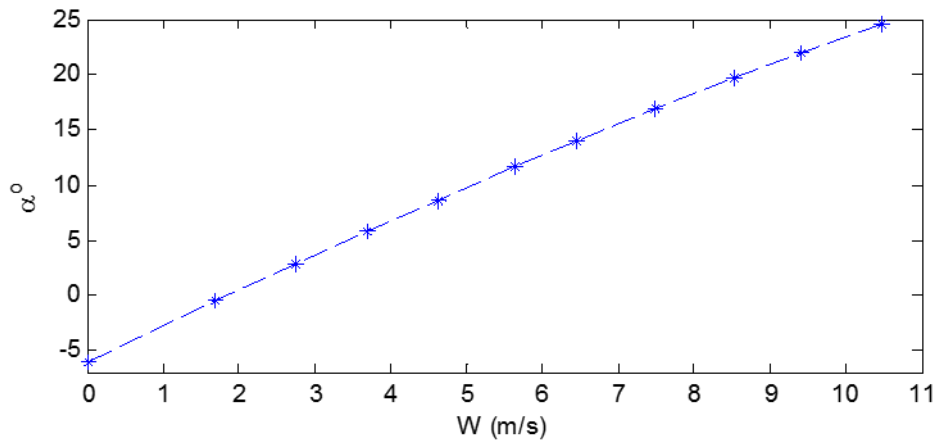
Figure 6.5. Angle of attack (α) vs. Wind speed (W) at mid-span.

108

The moment distribution along the blade is shown in Figure 6.6. The moment at lower r values is higher as expected due to the reasons discussed earlier. However, when the moment is normalized with the root value for each wind speed (beyond the initial negative moment range), interestingly all the curves collapse into a single distribution as seen in Figure 6.7. The normalized moment distribution is also very similar to the trends shown by the MOD-2 measurements [21] and the T40 blade model [6] in Figure 2.16 in section 2.1.5.2. The similar distribution for all wind speeds is a result of the constant chord and twist aerodynamic design of the blade since α is changing uniformly both along the blade and through the wind speed range as shown in Figure 6.2 and Figure 6.5.

The trend between the measurement points is not linear, the lines are for visual aid only. This applies to all the plots in this thesis. A non-linear fit would be a more suitable way to fit the distribution as in Figure 2.16.
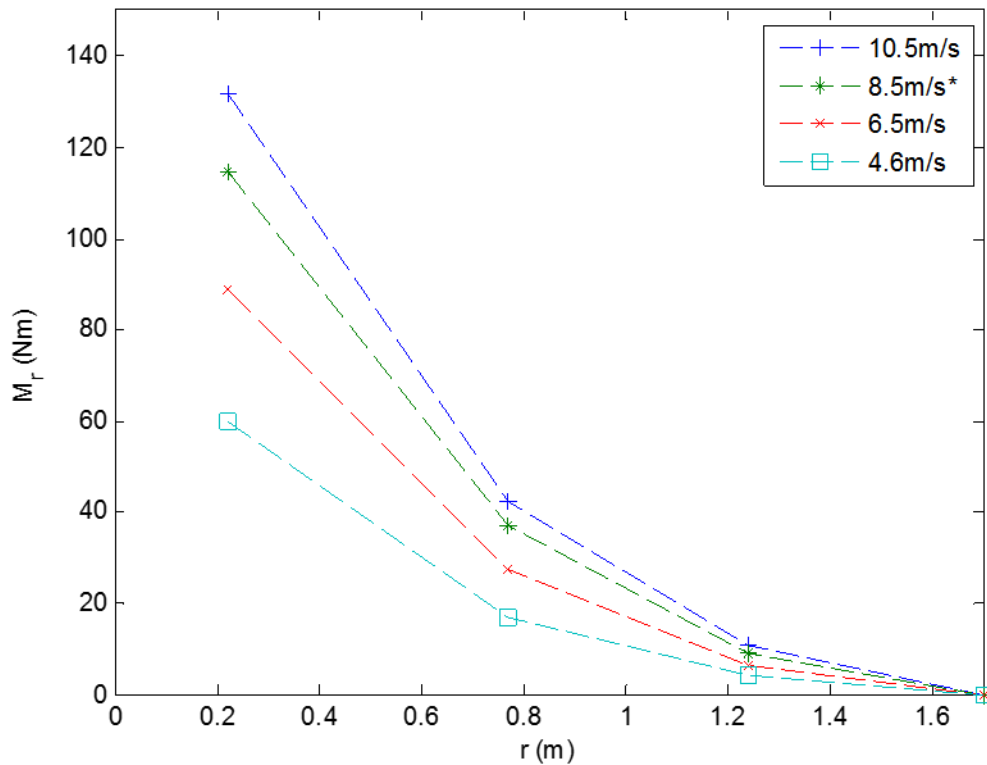
Figure 6.6. Moment (M_r) vs. radial position (r) for select wind speeds for the baseline case. *design wind speed*.

109
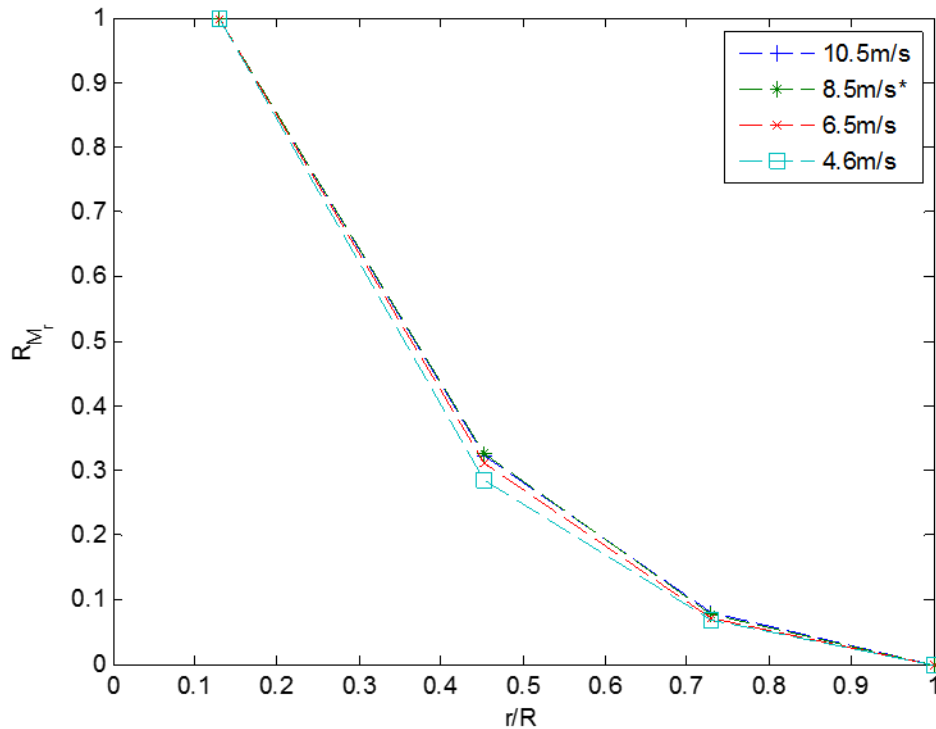
Figure 6.7. Normalized moment (R_{M_r}) vs. normalized radial position. *design wind speed*.

6.5 Effect of changing the flap angle

6.5.1 Moment vs. wind speed

The first comparison targets the effect of changing the deflection angle of the TEFs on the flapwise bending moment while keeping the location and length constant. The F2A formation with sections 4 and 5 is used to measure the effect of changing the angle. Positive angles represent a deflection towards the pressure side of the airfoil while negative angles represent a deflection towards the suction side.

  Figure 6.8 shows the moment measured at each strain gage location with the flap activated at 5° and -5°. Figure 6.9 shows magnified plots for moment measurements for all the deflections angles separately for each measurement location. The trends were consistent and showed a similar pattern for the measurements taken at each strain gage group. Positive deflection angles increase the C_l of the airfoil section while negative angles decrease the C_l as shown in Figure 2.18 and discussed in section 2.1.7. The increase in C_l increases the differential thrust force produced by the flapped airfoil. Since the flap was located following all the measurement points along the blade span, the higher force increased the moment measured at all locations. The flap positive deflection angles also cause stall to occur at a lower α as shown in Figure 2.18. The plots, however, showed no indication of stall occurring even at higher deflection angles. This is due to the blade operating at lower α towards the tip since the chord and twist were not optimized along the span for this specific blade.
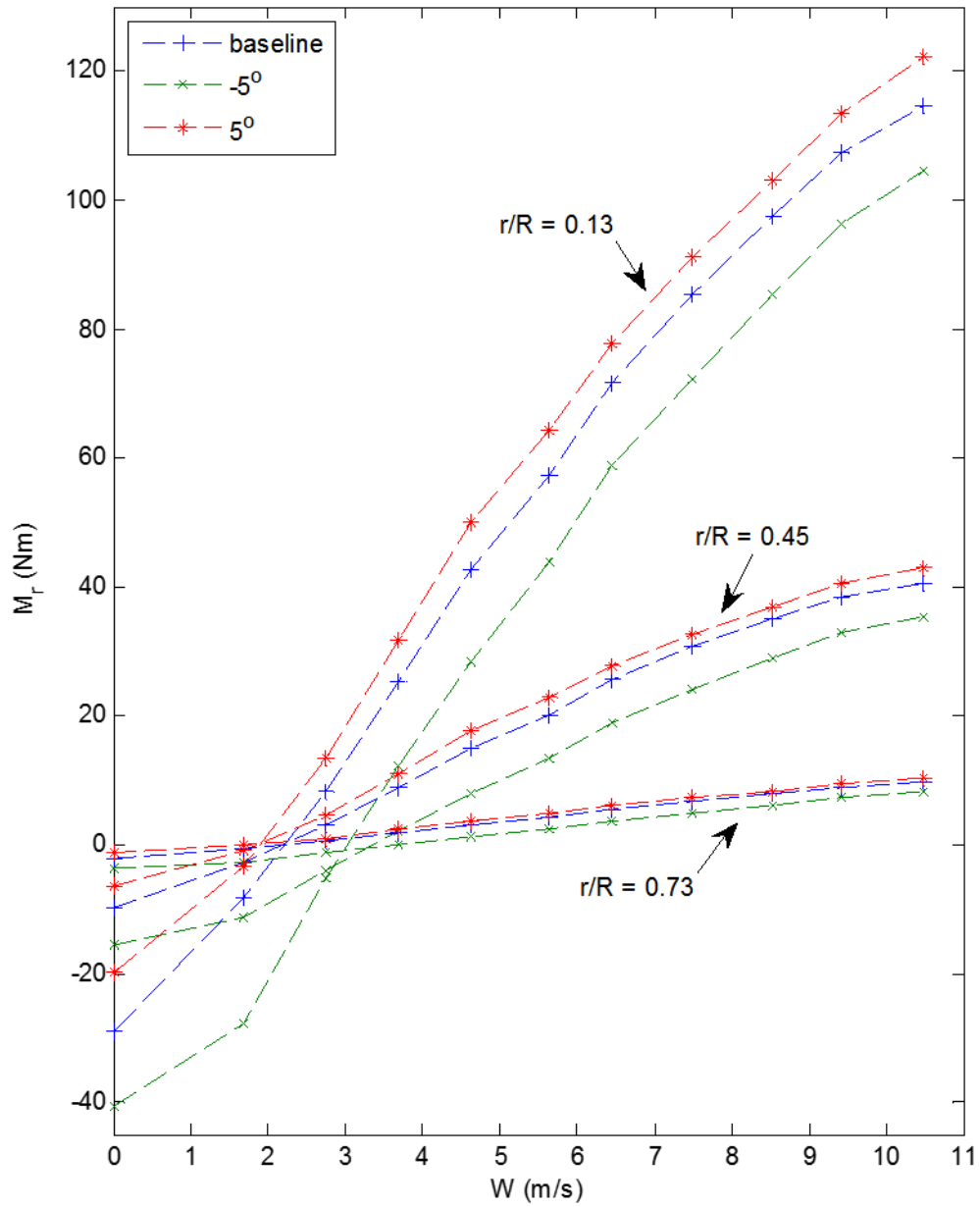
Figure 6.8. Moment (M_r) vs. Wind speed (W) with the F2A activated at -5° and 5° measured at each radial location.
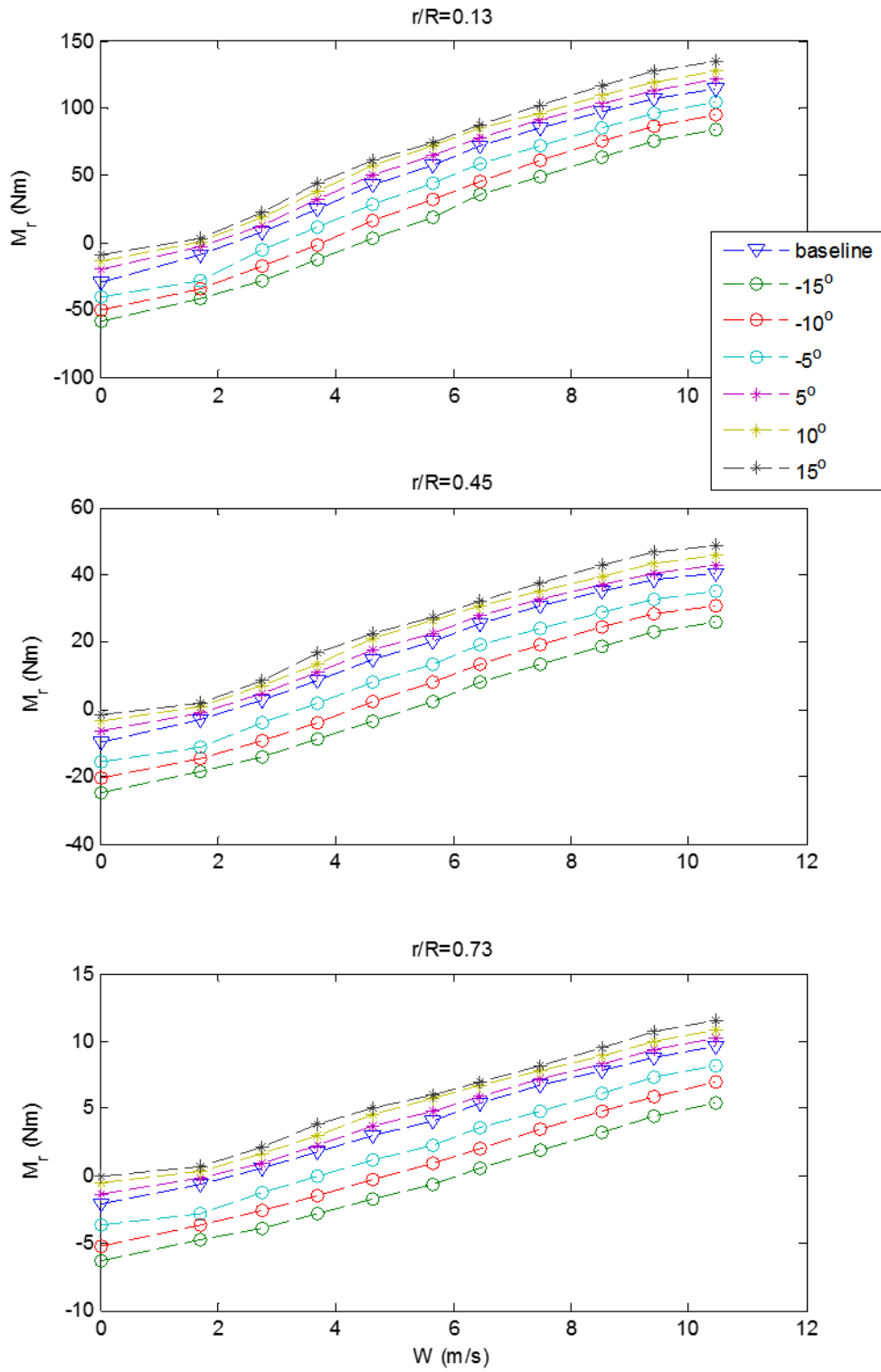
Figure 6.9. Moment (M_r) vs. Wind speed (W) with the F2A activated at each η measured at each radial location.

6.5.2 Moment vs. radial location

The increment moment change (ΔM_r) for each angle compared to the baseline case are plotted for each strain gage group in Figure 6.10. These plots represent the general trend for the loading distribution changes within the blade as the flap angles change. It is clear that the load changes are significantly higher near the blade root. Also, negative deflection angles cause a higher change than positive angles with the same value. This suggests that the change in the lift of the flapped section is not the only phenomena that reduces the forces on the blade. The flapped angle could be influencing other segments of the blade as will be discussed later in this chapter.
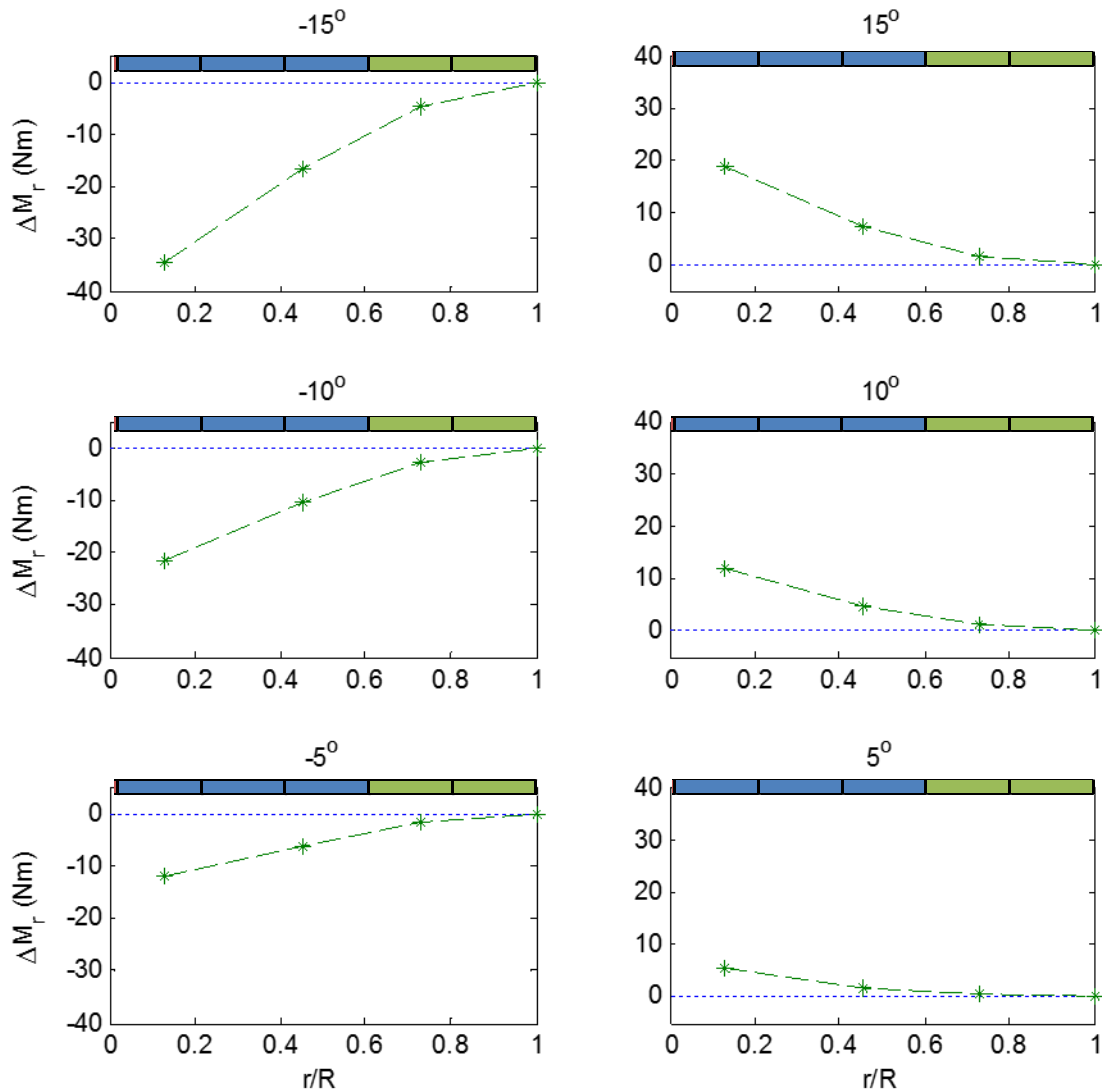
Figure 6.10. The increment change in flapwise bending moment measured at each η for the 8.5* m/s design wind speed.

113

6.5.3 Moment and power change vs. flap deflection angle

Figure 6.11 shows a comparison of the percentage change of power and moment for the F2A formation at the design speed and for the full range of flap angles. Moment at SG1 (blade root) was selected to represent the total change for the full-blade. The plot shows an increase in power with positive deflection angles. According to the differential torque equation 2.25 in section 2.1.3.4 the increase is an indication that a higher C_l was achieved. A higher C_l was possible without leading to stall as result of the blade twist not being optimized. Positive power augmentation can be useful for wind turbines in low wind conditions allowing operation at higher efficiency by increasing C_l. The increase in power was accompanied with an increase in the bending moment at a higher rate.
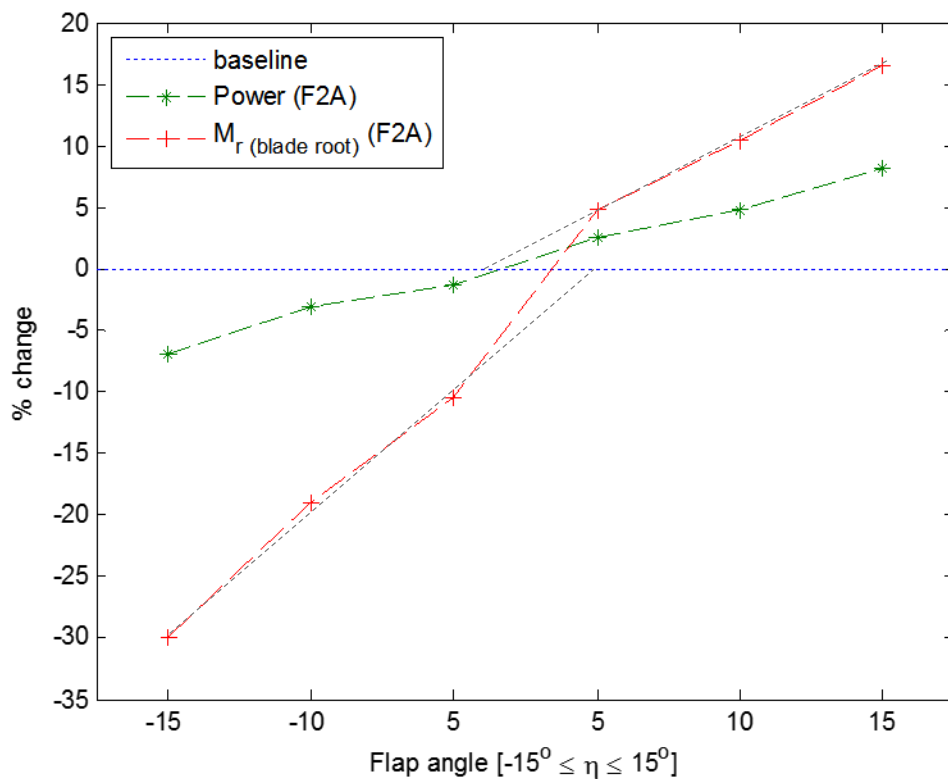
Figure 6.11. A comparison between the power and root moment reduction for the
F2A formation at design speed of 8.5 m/s.

It is evident that the change in moment and power are almost linear. This was expected as indicated by equation 2.49 derived from thin airfoil theory in section 2.1.7.2. The equation indicates a linear relationship between C_l and η. A linear trend was also observed on wind tunnel experiments for an airfoil with a hinged TEF in Figure 2.20 and Figure 2.21. However there is a discontinuity in the gradient between positive and negative deflection angles. This reflects the suggestion that the change in blade loading could be affected

114

by other phenomena in addition to the change in the flapped section's C_l. In all cases, the gradient for power change is lower than that of the strain with respect to the flap angle.

Another phenomena that could be theoretically causing the decrease in the moment is the formation of strong shed vortices at the newly formed tips as shown in Figure 6.12. This effect was also noted in [25]. The vortices are similar to the tip vortex created at the end of the blade that induces an α decrease on the inboard (towards hub) segments of the blade. The tip loss factor correction discussed in section 2.1.3.5 was developed to account for the effect of the tip shed vortex on the tip and inboard sections of the blade. The development of a shed vortex at the newly formed tip where the flap separates from the blade implies that the inboard segments of the blade experience a decrease in lift regardless of whether the flap angle is positive or negative. The decrease in lift for the inboard segments could explain the lower rate for the increase of the flapwise bending moment measured for positive deflection angles. The extent of this effect can't be accurately identified until it is measured. This can be done using a setup similar to the one in [26] and is discussed in the Future work section.
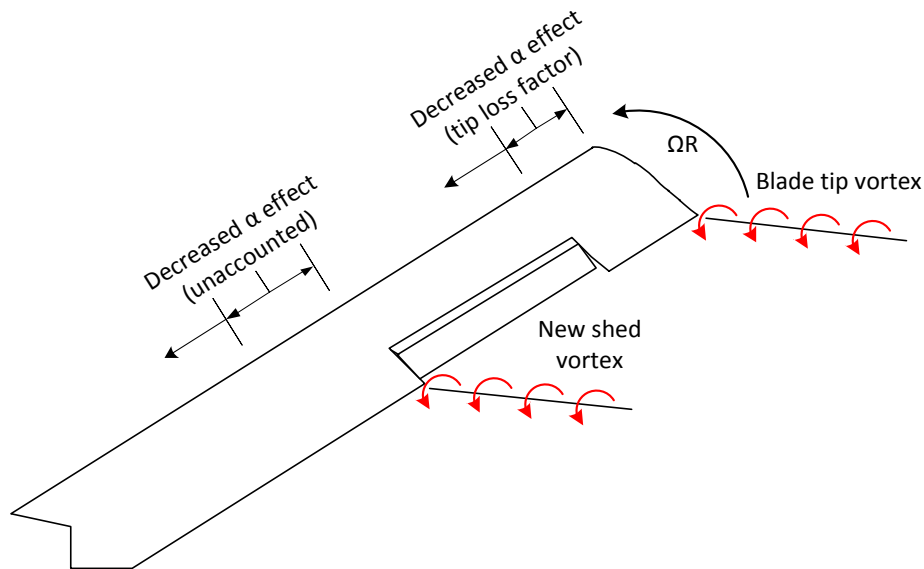
Figure 6.12. Shed vortex effect.

6.6 Effect of changing length and location of flaps

6.6.1 Moment vs. wind speed

The second comparison targets the effect of changing the effective length and location of the TEFs on the flapwise bending moment while keeping the flap deflection angle constant. Figure 6.13 shows the moments plotted against different wind speeds for all single section (half length) formations (as illustrated in Figure 5.9) and measured at each strain gage location. Figure 6.14 shows magnified plots for moment measurements for all the flap formations (single and double flaps) at each measurement location. The deflection angle was set to -15° in all cases. The reduction in moment compared to the baseline case is greatest when the flap closest to the tip is activated (F1A). The reduction is caused by a decrease in C_l at

the flap location as discussed earlier. The moment reduction is decreased as the flap location moves closer to the hub. This indicates that the furthest blade segments contribute the most to the bending moment which is expected from equation 2.44 that represents bending on the blade by coupling the aerodynamic load and cantilever equations, and the conclusions of section 2.1.5.2.

Activating the flap in the section closest to the hub (F1C) caused a slight increase in the moment measured by SG3 (at r/R=0.73) which accounts for the load changes at the tip section. When the two closest flaps to the hub are activated (F2C) as shown in Figure 6.14 this increase is more evident. This increase in moment occurs despite the fact that the flaps in both cases only affecting sections that are not contributing to the moment measured by SG3.
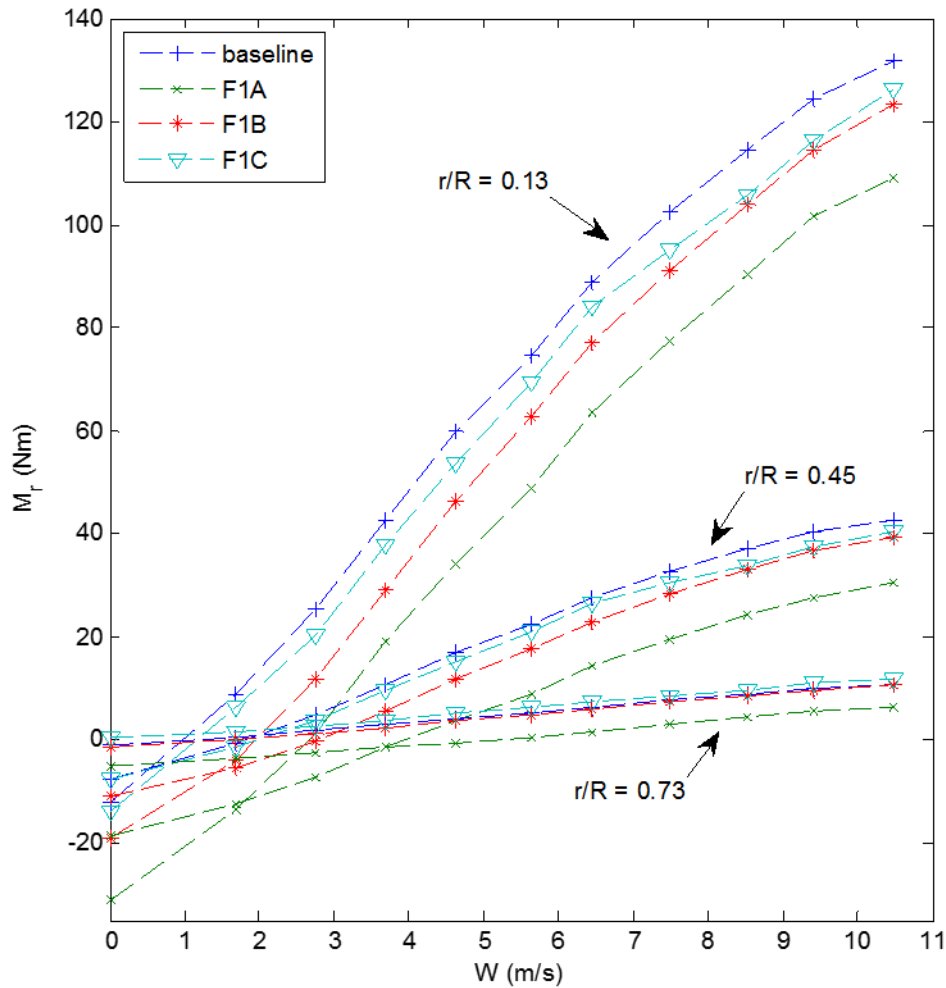
Figure 6.13. Moment (M_r) vs. Wind speed (W) with the single flap formations (F1X) activated at -15º measured at each radial location.

Figure 6.14. Moment (M_r) vs. Wind speed (W) for all formations activated at -15°
measured at each radial location.

This unexpected increase in moment at the tip can possibly be related to the effect of the coning angle Φ. As the flap is activated the reduction in lift directly affects the moment on all the points on the blade span between the flap and the hub. The decrease in the overall lift of the blade represented by the moment measured at the blade root indicates that Φ is reduced. The reduction of Φ as indicated by equation 2.41 and discussed in section 2.1.5.1 increases the differential thrust force of the blade segments. SG1 and SG2 measure an overall reduction in moment as they are affected by the decrease in C_l of the flapped section and t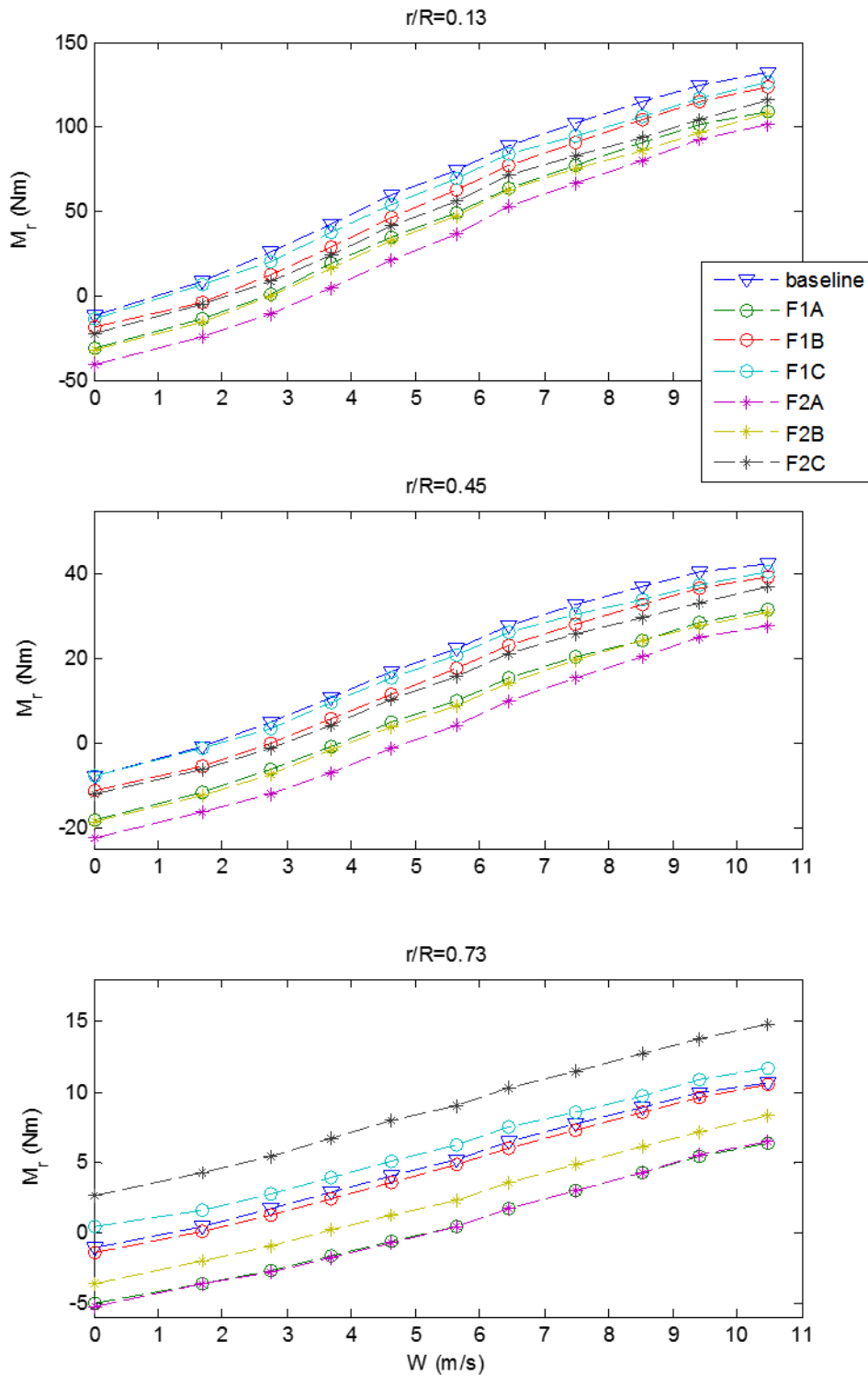he decrease in Φ while the effect of the latter is significantly weaker. SG3, however, is only affected by the decrease in the coning angle as shown in Figure 6.13. This leads to the slight increase in moment measured at the tip section. The increase in moment is, however, quantitatively trivial compared to the total change in moment of the blade.
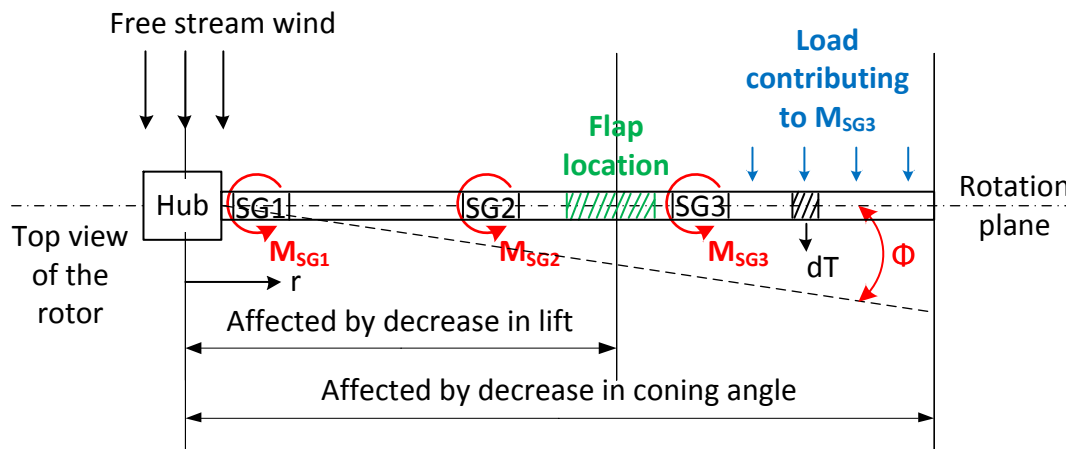
Figure 6.15. Coning angle effect.

On the other hand, the F1A formation is the only case with a single section (half length) activated flap that shows a higher reduction in bending moment than a full length formation, F2C, which has double sections with activated flaps. Referring to the formation schematic in Figure 5.9 this indicates that activating the last section of the blade alone causes a higher reduction in bending moment than activating both the third and fourth sections together. This observation can be identified in the first plot in Figure 6.14. The formation of a shed vortex at the newly formed tip at the flapped section could possibly explain the significant advantage in load reduction of the shorter F1A formation over the F2C one. When the outermost flap is activated, the shed vortex would affect the whole outer sections of the blade in addition to the flapped one which contribute the most to the blade load, multiplying the lift reduction effect. When the two inner sections are activated, the vortices would affect the segments of the blade closer to the hub which would have a weaker effect on the load change.

6.6.2 Moment distributions along blade span

Figure 6.16 shows the moment distributions for each flap formation at the design wind speed. The distributions are clearly not following a consistent pattern similar to the one seen in Figure 6.6. When the moment curves are normalized they don't collapse into a single distribution as shown in Figure 6.17. The non-uniform trends were expected since the aerodynamic character of the full blade is discretely modified

118

as the flaps are activated in different formations. The lift reduction mechanisms could also not be limited to the airfoil geometry change as described earlier causing non-uniform load distribution changes even for flaps with the same span placed at different locations.
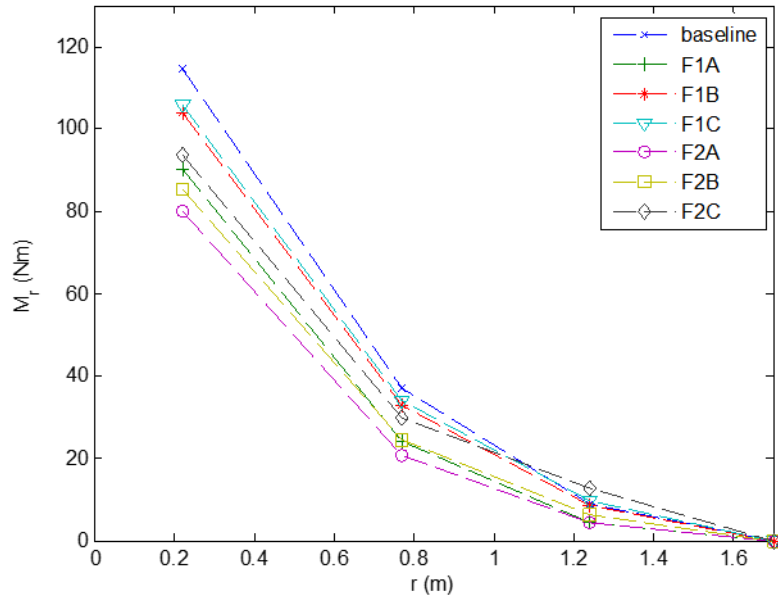
Figure 6.16. Moment (M_r) vs. radial position (r) for each formation activated at -15°

at the 8 m/s design wind speed.
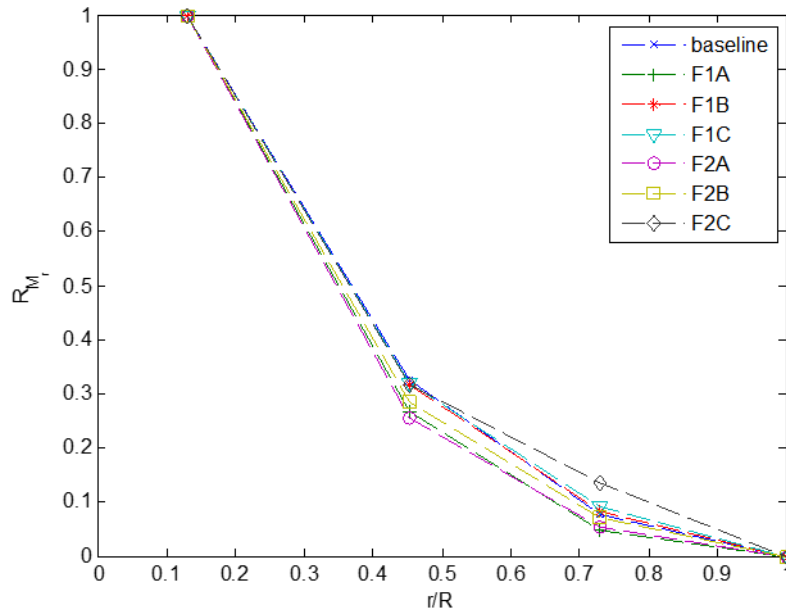
Figure 6.17. Normalized moment (R_{M_r}) vs. radial position (r/R) for each formation

activated at -15° at the 8 m/s design wind speed.

6.6.3 Moment vs. radial location

The increment moment change for each formation compared to the baseline case are plotted for each strain gage group in Figure 6.18. The design speed is chosen to represent this change. These plots represent the general trend in the load distribution within the blade as the flap locations change. The moment reduction for the tip portion of the blade decreases as the flap location gets closer to the hub until it eventually becomes an increase. This re-iterates the observation made in Figure 6.14 and is theoretically attributed to the effect of coning.
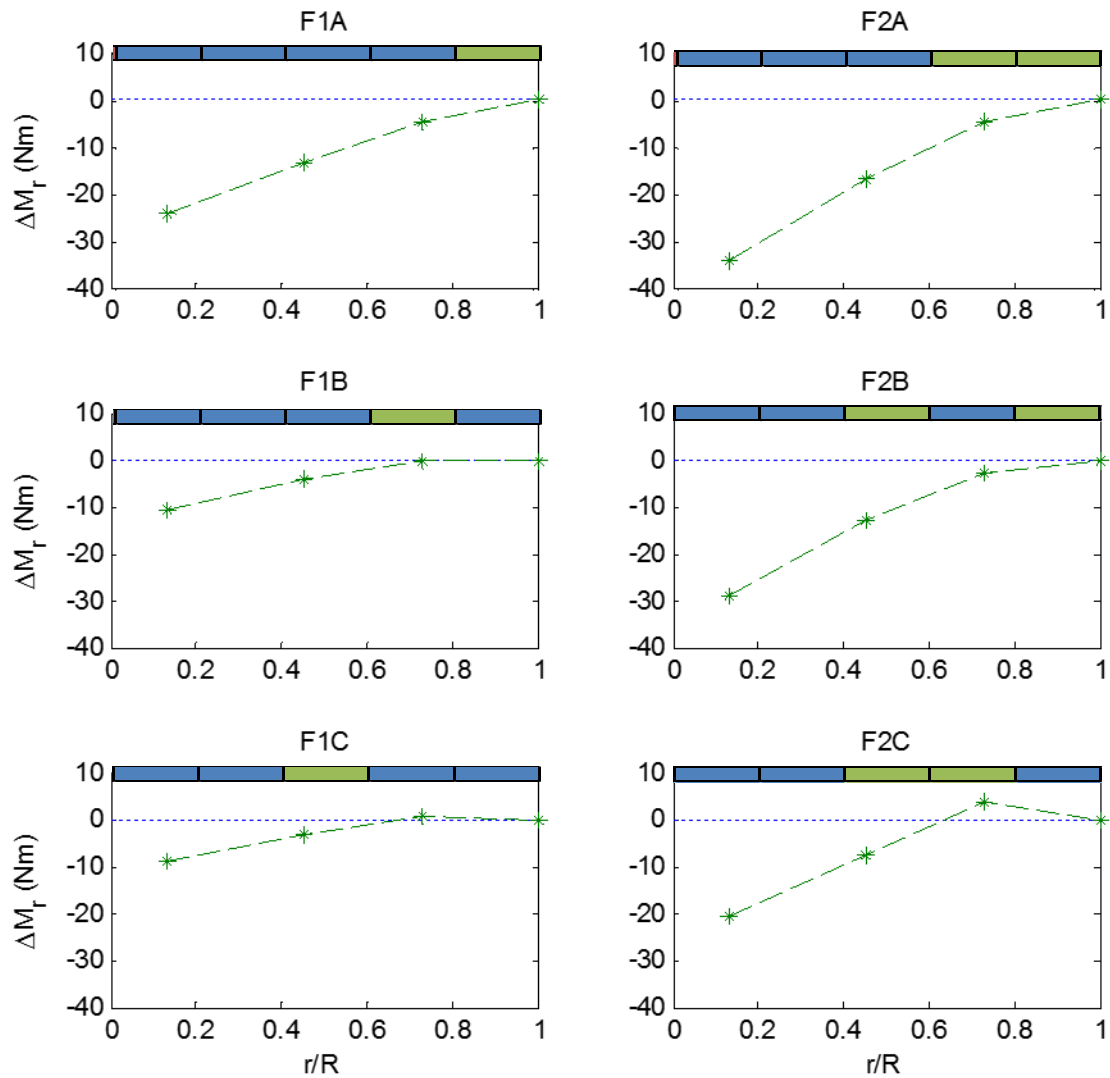
Figure 6.18. The value change in moment (ΔM_r) for each flap formation along the blade length for the 8.5 m/s design wind speed.

6.6.4 Moment change vs. relative flap location

The percentage change in root moment (M_r) as an effect of the relative flap location activated at -15º is shown in Figure 6.19. It is clear that the percentage change is not linearly changing with the distance of the flap from the hub. Activating section 1 (F1A) causes significantly higher moment reduction than the following two sections. A possible explanation to the significant difference in moment reduction is the inboard effects of the flap explained earlier. The outermost flap would reduce the C_l of the sections preceding it affecting the sections that contribute most to the moment and power production. This result is similar to the conclusion in Joncas *et al.* [27] where it was determined that a flap placed between 75% of the span and the root tip contributed to 50% of the load alleviation using a simulation (details can be found in section 2.2.2).
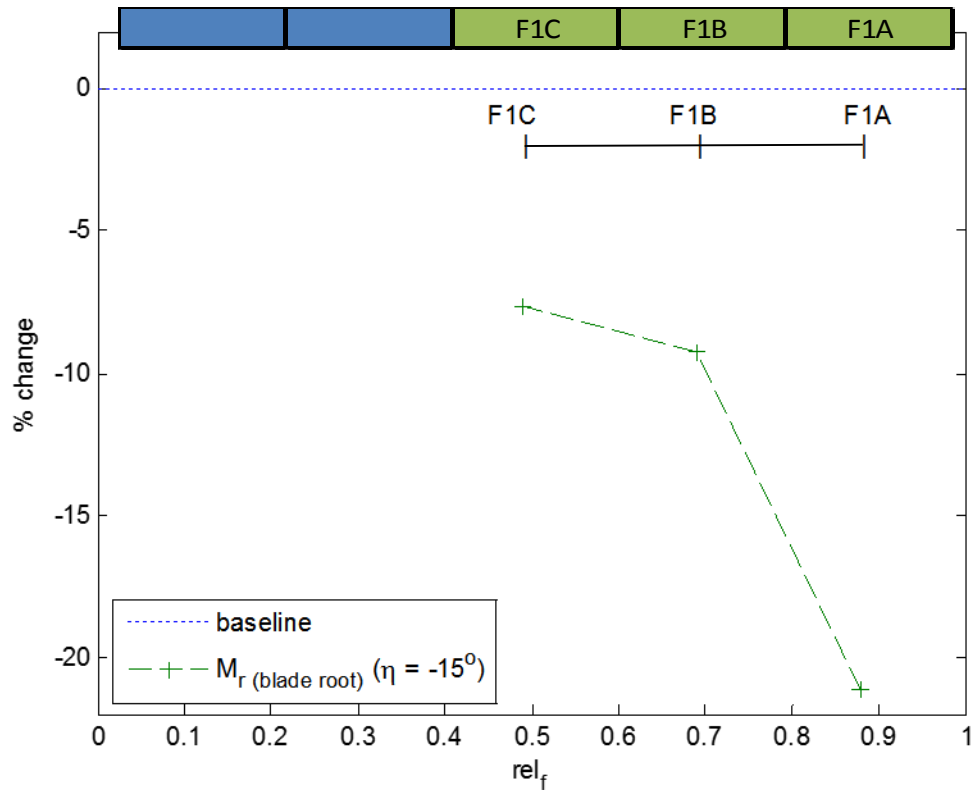
Figure 6.19. Percentage moment change for single flap formations at -15º and design speed, 8.5m/s.

121

Chapter 7

Conclusion

There were two primary objectives of this thesis. First, to develop a medium scale wind turbine test rig and customizable blade that enable accurate measurement of the effect of TEFs on the performance and structural loading of wind turbines rotors. Second, to demonstrate the capability of the developed system through a steady state study of the effect of stationary hinged TEFs on blade load and power production. The objectives were successfully met by the completion of the design, fabrication and assembly of the test rig and blade system and the results of the experimental testing proving the ability of this setup to accurately measure the response to changes in the flap parameters. This chapter outlines the conclusions from the findings of the experiment performed and recommendations for future work.

7.1 Test turbine rig

The test turbine rig achieved the design goals of precise rotation speed control while limiting the size of the nacelle. The rig is a valuable addition to experimental apparatus at the UW wind facility. It enabled safer testing of the currently available rotors at higher rpms and velocities without the risk caused by uncontrolled vibrations and free-wheeling experienced by the previous rotors. That in addition to automatic compensation and speed control, widened the scope of future research that can be performed using the facility and apparatus in the field of experimental wind turbine testing. The smaller and more aerodynamic nacelle size solves post rotor flow issues caused by the previous test rig's much larger nacelle. The significant nacelle size reduction addresses measurement problems outlined in previous experiments done in the facility such as the experimental BEM prediction study by Johnson *et al.* [26] and unpublished experiments predicting freestream velocities based on correlation with nacelle mounted anemometers.

7.1.1 Improvements to the setup

The power measurement method used in this study could be improved by using a torque sensor at the designated location along the driveshaft according the test rig design (see section 3.3.5). The placement of a torque sensor at that location will provide the most precise and consistent reading of the rotor performance without being affected by the rest of the drive-train losses. It will also allow us to accurate estimation of real-time drive-train losses by calculating the difference between the power calculated using the dynamic

brake resistor parameters and the power calculated from the torque sensor output. In addition, a purpose-built program using Labview® should be used to trigger recording and simultaneously log data from the torque sensor, strain gages and any additional instrumentation. The synchronized data can relate load patterns with blade location and other operational conditions. This would be a requirement for any dynamic testing.

7.2 Blade fabrication

The novel 3D printing and modular blade design utilizing a single accessible structural element proved successful in both precision and structural integrity for testing at high rotation speeds. This success paves the way for easy and quick prototyping of more complex and precise airfoil patterns and other fixed aerodynamic surfaces such as Gurney flaps and vortex generators [59] and other active aerodynamic surfaces such as microtabs [22]. Different technologies that require modification of the airfoil geometry can be directly incorporated to the available design by modifying the available 3D models and re-printing only the segments that were changed. In addition, the hollow accessible core of the blade allows additional instrumentation to be added to the assembly. As an example, instrumenting the blade with a series of pressure transducers is currently an ongoing project in the research group that required only one blade segment design to be modified and re-printed. The design also facilitated the instrumentation of the blade with minimal or no interference or obtrusion to normal operation such as the placement of the strain gages on the internal support spar with the wires running inside the structure. These features combined with the accessibility to 3D printing facilities render the scope of new rotor research possibilities virtually limitless.

7.3 Instrumentation and data acquisition

The strain measurement and data transfer methods were precise and highly responsive. The full bridge configuration using high resistance strain gages produced repeatable and sensitive measurements. The front mounted slip ring transferred the data successfully with minimal noise. The power measurements suffered similar disadvantages to the method used by the previous rig where voltage and current over the dissipation system is used as a primary source for the quantities. An improved method to measure the torque or power produced by rotors attached to the test turbine rig has been included in the design and the reassembly of a torque sensor into the system is a work in progress. It will be used for more precise power measurements in all future testing.

7.4 Trailing edge flap effects

The primary experiment was designed to measure the changes in axial loading and power production of a blade as a function of different trailing edge parameters. The flapwise bending moment was measured by three groups of strain gages placed along the blade. The baseline power measurements of the rotor showed good correlation with PROPID [16] and for all three locations the bending moment increased with wind speed as expected. The bending moment along the blade showed a reduction when the flaps where pitched in negatives angles (toward suction side) and an increase with positive angles (towards pressure side). The measured moment distribution along the blade was similar to previous experiments and aligned well with theory.

For a fixed TEF position, positive deflection angles showed an increase in moment in general, while a negative deflection showed a decrease in moment as expected. The rate of moment change as a function of the deflection angle was linear as expected from theory and airfoil wind tunnel experiments, however, it was lower for positive deflection. Strong shed vortices created at the new tips formed where the flap separates from the blade was suggested as an additional reason that modifies the blade aerodynamics when the flap is activated, leading to a reduction in lift for both positive and negative deflections. Detailed wind speed measurement along the rotor are required to quantify the effect of the shed vortex.

For a fixed TEF deflection angle of -15º and a single flap section (15% of the blade span), the moment reduction was significantly higher at outermost flap section compared to the second and third ones. The reduction reached up to 22.5% for the outermost section, compared to 10% and 7.5% for the second and third sections respectively. A slight increase in moment was observed at the furthest location from the hub when a flap preceding it was activated. This effect was attributed to the reduction in coning angle that is induced when the overall axial force on the blade is reduced. The final station measured the forces by the segment of the blade that was influenced by the reduction in coning angle but not the reduction in lift of the flapped section. The reduction in coning angle results in a slight increase in thrust according to theory. It is unknown whether the shed vortex produced by the newly formed tip could have a different effect outboard (towards tip) of the blade and possibility contribute to this observation, however it should be investigated.

Negative deflection angles caused less reduction in the power production of the blade compared to moment reduction. The reduction in moment reached 30% for the maximum η of -15º compared to 6.5% reduction in power for the same angle utilizing the flaps in the last two sections (approximately between 65% and 95% of the blade span). This observation can prove beneficial when designing the optimum location for the placement of TEFs to maximize the effect on axial blade loads or on power reduction.

Overall, the experimental setup proved to be effective in measuring small changes in flapwise bending moment within the wind turbine blade.

7.5 Future work

The relative success of the static angle testing of the blade and the proven ability of the system to measure moment changes within the blade with high precision and sensitivity paves the way for numerous possibilities for further research.

Stationary Flap Testing

The experimental setup can utilize a previously developed experimental BEM analysis method in Johnson *et al.* [26] for more detailed analysis of the aerodynamic changes along the blade caused by TEFs. This method measures the wind velocity in 3D with a relative high sampling rate. Such measurements would enable accurate identification of the effects of hypothesized phenomena such as the effect of shed vortices created by the TEF configuration. It will also allow the determination of the induction factors for correct computation of α. This method can only be applied for stationary flaps. However, it would prove useful for possibly measuring more accurate changes in C_l and C_d of flapped airfoils if implemented alongside an experimental procedure similar to the one applied for the atmospheric TEF investigation discussed in section 2.2.1.

On the other hand, a redesigned blade that stalls within the wind speed range of the facility can be used to test the ability of TEF to regulate power production above rated condition. The flaps at their current configuration showed significant potential for power augmentation reaching a reduction up to 20% for the largest deflection angles.

Dynamic Flap Testing

Experimental dynamic testing of TEFs in an active flow control setting can be achieved with a few modifications to the current setup. Similar dynamic studies reported great potential for fatigue load reduction using TEFs as discussed in section 2.2.3. The goal of such a study would be to limit the transformation of wind fluctuations in the freestream into load fluctuations within the blade structure in order to reduce the fatigue load. This would require the addition of a controller and actuator to the testing system and has been taken into consideration in the design of the blade used in this experiment as indicated in 4.4.2. The arrangement allows the addition of a servomotor that can control flap angle adjustment. The Dynamixel MX-64R from ROBOTIS [60] is a high-performance networked actuator fully integrated with a driver and a controller in one relatively small sized device and is recommended for such a study. The specific capabilities and specifications of the device need to be studied in more detail, but it seems as the most suitable option based on a rudimentary comparison of available actuators and controllers. Coupling the servomotor and the strain gauges will create a closed feedback system for an active 'smart' blade. Torque sensor data and strain gages placed on the monopole tower would provide valuable insight of the effect of the reduction of fluctuating loads on the tower and drive shafts of the wind turbine test rig.

A dynamic study of the fatigue reduction capabilities on the scale provided by the facility and apparatus made available by the work on this project is expected to be a unique and highly valuable contribution to research on wind turbine control and analysis.

Bibliography

[1]   T. K. Barlas and G. A. M. van Kuik, "Review of state of the art in smart rotor control research for wind turbines," *Prog. Aerosp. Sci.*, vol. 46, no. 1, pp. 1–27, Jan. 2010.

[2]   J. W. van Wingerden, a. W. Hulskamp, T. Barlas, B. Marrant, G. A. M. van Kuik, D.-P. Molenaar, and M. Verhaegen, "On the Proof of Concept of a 'Smart' Wind Turbine Rotor Blade for Load Alleviation," *Wind Energy*, vol. 11, no. 3, pp. 265–280, May 2008.

[3]   I. H. Abbott and A. E. von Doenhoff, *Theory of Wing Sections - Including a Summary of Airfoil Data*. Dover Publications, 1959.

[4]   M. Liserre, T. Sauter, and J. Y. Hung, "Future energy systems: Integrating renewable energy sources into the smart power grid through industrial electronics," *Industrial Electronics Magazine, IEEE*, vol. 4, no. 1, pp. 18–37, 2010.

[5]   N. Fichaux, J. Beurskens, P. H. Jensen, J. Wilkes, S. Frandsen, J. D. Sorensen, P. Eecen, and E. Al., "UpWind: Design limits and solutions for very large wind turbines," Sixth Framework Programme, 2011.

[6]   T. Burton, D. Sharpe, N. Jenkins, and E. Bossanyi, *Wind Energy Handbook*. John Wiley & Sons, 2001.

[7]   E. A. Bossanyi, "Further load reductions with individual pitch control," *Wind Energy*, vol. 8, no. 4, pp. 481–485, Oct. 2005.

[8]   T. J. Larsen, H. a. Madsen, and K. Thomsen, "Active load reduction using individual pitch, based on local blade flow measurements," *Wind Energy*, vol. 8, no. 1, pp. 67–80, Jan. 2005.

[9]   J. F. Manwell, J. G. McGowan, and A. L. Rogers, *Wind Energy Explained*, 2nd ed. John Wiley & Sons, 2009.

[10]   L. A. Viterna and D. F. Ancona III, "Commercial Wind Turbine Systems and Applications," in *Wind Turbine Aerodynamics Part A: Basic Principles Wind Turbine Technology: Fundamental Concepts of Wind Turbine Engineering*, 2nd ed., D. A. Spera, Ed. New York: ASME Press, 2009, pp. 203–280.

[11]   J. D. J. Anderson, *Fundamentals of Aerodynamics*, 5th ed. New York: McGraw-Hill, 2011.

[12]   E. L. Houghton and P. W. Carpenter, *Aerodynamics for Engineering Students*, 4th. ed. New York: Wiley & Sons, 1993.

[13]   M. O. L. Hansen, *Aerodynamics of Wind Turbines*, 2nd ed. London: Earthscan, 2008.

[14]   E. Hau, *Wind Turbines: Fundamentals, Technologies, Application, Economics*, 2nd ed. Berlin: Springer-Verlag, 2006.

[15]   R. E. Wilson, "Wind Turbine Aerodynamics Part A: Basic Principles," in *Wind Turbine Technology: Fundamental Concepts of Wind Turbine Engineering*, 5th ed., D. A. Spera, Ed. New York: ASME Press, 2009, pp. 281–350.

[16]   UIUC Applied Aerodynamics Group, "PROPID." [Online]. Available: http://aerospace.illinois.edu/m-selig/propid.html.

[17]   M. S. Selig and J. L. Tangier, "Development and Application of a Multipoint Inverse Design Method for Horizontal Axis Wind Turbines," *Wind Eng.*, vol. 19, no. 2, 1995.

[18]   M. S. Selig, "PROPID User Manual," UIUC Applied Aerodynamics Group, 2012.

[19]   J. L. Tangler, "A Horizontal Axis Wind Turbine Performance Prediction Code for Personal Computers," User's Guide, Solar Energy Research Institute, 1987.

[20]   B. Hibbs and R. L. Radkey, "Small Wind Energy Conversion Systems (SWECS) Rotor Performance Model Comparison Study," Technical report, Aerovironment, Inc., prepared for Rockwell International Corporation, 1981.

[21]   "MOD-2 Wind Turbine System Develpoment, Final Report," CR 168007, NASA, 1982.

[22]   S. J. Johnson, J. P. Baker, C. P. van Dam, and D. Berg, "An overview of active load control techniques for wind turbines with an emphasis on microtabs," *Wind Energy*, vol. 13, no. August 2009, pp. 239–253, 2010.

[23]   J. R. Zayas, C. P. van Dam, R. Chow, J. P. Baker, and E. A. Mayda, "Active Aerodynamic Load Control for Wind Turbine," in *European Wind Energy Conference*, 2006.

[24]   M. Drela, "XFOIL: An Analysis and Design System for Low Reynolds Number Airfoils," in *Low Reynolds Number Aerodynamics*, T. J. Mueller, Ed. Berlin: Springer-Verlag, 1989, pp. 1–12.

[25]   S. L. Miller, G. A. Quandt, and S. Huang, "Atmospheric Tests of Trailing-Edge Aerodynamic Devices," NREL/SR-500-22350, National Renewable Energy Laboratory, 1998.

[26]   D. A. Johnson, A. Abdelrahman, and D. Gertz, "Experimental Indirect Determination of Wind Turbine Performance and Blade Element Theory Parameters in Controlled Conditions," *Wind Eng.*, vol. 36, no. 6, pp. 716–737, 2012.

[27]   S. Joncas, O. Bergsma, and A. Beukers, "Power regulation and optimization of offshore wind turbines through trailing edge flap control," in *Proceedings of the 43th AIAA Aerospace Science Meeting and Exhibit*, 2005, pp. 10–13.

[28]   M. A. Lackner and G. van Kuik, "A comparison of smart rotor control approaches using trailing edge flaps and individual pitch control," *Wind Energy*, vol. 13, no. 1, pp. 117–134, 2009.

[29]   J. Jonkman, S. Butterfield, and W. Musial, "Definition of a 5-MW Reference Wind Turbine for Offshore System Development," National Renewable Energy Laboratory, 2009.

[30]   P. B. Andersen, L. Henriksen, M. Gaunaa, C. Bak, and T. Buhl, "Deformable trailing edge flaps for modern megawatt wind turbine controllers using strain gauge sensors," *Wind Energy*, vol. 13, no. December, pp. 193–206, 2010.

[31]   A. W. Hulskamp, J. W. van Wingerden, T. Barlas, H. Champliaud, G. A. M. van Kuik, H. E. N. Bersee, and M. Verhaegen, "Design of a scaled wind turbine with a smart rotor for dynamic load control experiments," *Wind Energy*, vol. 14, no. 3, pp. 339–354, 2011.

[32]   D. Castaignet, T. Barlas, T. Buhl, N. K. Poulsen, J. J. Wedel-Heinen, N. A. Olesen, C. Bak, and T. Kim, "Full-scale test of trailing edge flaps on a Vestas V27 wind turbine : active load reduction and system identification," *Wind Energy*, 2013.

[33]   D. Castaignet, "Results from the first full scale wind turbine equipped with trailing edge flaps," *28th AIAA Appl. Aerodyn. Conf.*, vol. 28, no. July, pp. 1–9, 2010.

[34]   D. Gertz, "An Evaluation Testbed for Alternative Wind Turbine Blade Tip Designs," Master Thesis, University of Waterloo, 2011.

[35]   Keithley Instruments Inc, "Model 2700 Digital Multimeter Data Acquisition and Datalogging System w/ 2 Slots GPIB/RS232," 2014. [Online]. Available: http://www.keithley.com/products/data/datalogger/?mn=2700.

[36]   B. Gaunt, "Power Generation and Blade Flow Measurements of a Full Scale Wind Turbine," Master Thesis, University of Waterloo, 2009.

[37]   C. B. Devaud, J. Weisinger, D. A. Johnson, and E. J. Weckman, "Experimental and numerical characterization of the flowfield in the large-scale UW live fire research facility," *Int. J. Numer. Meth. Fluids*, vol. 60, pp. 539–564, 2009.

[38]   M. K. Mcwilliam, "Development of a Wind Tunnel Test Apparatus for Horizontal Axis Wind Turbine Rotor Testing by," Master Thesis, University of Waterloo, 2008.

[39]   Marathon Electric, "Motor Model Details," 2014. [Online]. Available: http://www.marathonelectric.com/MMPS/details.jsp?item=184THTL17038.

[40]   NORD Drivesystems, "NORDBLOC.1 Gearbox with NEMA Motor Adapter," 2014. [Online].
       Available: http://www5.nord.com/cms/media/documents/bw/G1012_PL_CZ_GB_2210.pdf.

[41]   Emerson Electric Co, "Unidrive SP Panel Mount - High performance universal AC drive range,"
       2014. [Online]. Available: http://www.emersonindustrial.com/en-
       US/controltechniques/products/acdrives/unidrivesppanelmount/Pages/default.aspx.

[42]   C.-C. Yu, *Autotuning of PID controllers*. London: Springer-Verlag, 2006.

[43]   Baldor Electric Company, "Bearing Engineering Catalog," 2014. [Online]. Available:
       http://www.baldor.com/support/CA3000catalog.asp.

[44]   FUTEK Advanced Sensor Technology Inc, "Rotary Torque Sensor - Non contact shaft to shaft
       with Encoder," 2014. [Online]. Available: http://www.futek.com/product.aspx?stock=FSH02059.

[45]   R+W, "BKL Bellows Coupling with clamping hub." [Online]. Available: http://www.rw-
       america.com/products/bellows_couplings/bk/bkl/.

[46]   A. Abdelrahman and C. Knischewsky, "UW Wind Turbine Test Rig: Design, Installation and
       Operation," Technical Report, Univeristy of Waterloo, 2014.

[47]   Michigan Scientific Corporation, "S-Series Slip Ring Assembly," 2005. [Online]. Available:
       http://www.michsci.com/Products/sliprings/eos/s_series.htm.

[48]   A. C. Ugural and S. K. Fenster, *Advanced Strength and Applied Elasticity*, 4th. ed. Prentice Hall,
       2003, p. 560.

[49]   W. F. Stokey, "Vibration of systems having distributed mass and elasticity," in *Harris' shock and
       vibration handbook*, 5th. ed., C. M. Harris, Ed. New York: McGraw-Hill, 2002.

[50]   P. B. Andersen, "Advanced Load Alleviation for Wind Turbines using Adaptive Trailing Edge
       Flaps : Sensing and Control," PhD Thesis, Technical University of Denmark, 2010.

[51]   D. M. Somers, "The S833, S834 and S835 Airfoils," Technical Report NREL/SR- 500-36340,
       National Renewable Energy Laboratory, 2005.

[52]   D. T. Pham and R. S. Gault, "A comparison of rapid prototyping technologies," *Int. J. Mach.
       Tools Manuacture*, vol. 38, pp. 1257–1287, 1998.

[53]   S. Bradshaw, A. Bowyer, and H. P., "The Intellectual Property implications of low-cost 3D
       printing," *ScriptEd*, vol. 7, no. 1, pp. 5–31, 2010.

[54]   Stratasys Ltd., "Fortus 360mc Versatile machine. Durable parts.," 2014. [Online]. Available:
       http://www.stratasys.com/3d-printers/production-series/fortus-360mc#content-slider-1.

[55]   B. Gaunt and D. A. Johnson, "Wind turbine performance in controlled conditions: Experimental results," *Int. J. Green Energy*, 2012.

[56]   OMEGA Engineering Inc., "Precision Strain Gages Dual-Grid for Bending Strains," 2014. [Online]. Available: http://www.omega.com/pptst/SGD_DUAL-GRID.html.

[57]   Campbell Scientific Inc, "CSAT3 3-D Sonic Anemometer," 2014. [Online]. Available: http://www.campbellsci.ca/csat3.

[58]   National Instruments Corporation, "NI 9237 - National Instruments," 2014. [Online]. Available: http://sine.ni.com/nips/cds/view/p/lang/en/nid/208791.

[59]   W. A. Timmer and R. van Rooij, "Summary of the Delft University Wind Turbine Dedicated Airfoils," *J. Sol. Energy Eng.*, vol. 125, no. 4, pp. 488–496, 2003.

[60]   ROBOTIS, "MX64-T/MX64-R ROBOTIS e-manual," 2010. [Online]. Available: http://support.robotis.com/en/.

[61]   A. J. Wheeler and A. R. Ganji, *Introduction to Engineering Experimentation*, 2nd. ed. New Jersey: Pearson Prentice Hall, 2004.

[62]   S. Tavoularis, *Measurement in Fluid Mechanics*, 1st. ed. New York: Cambridge Univeristy Press, 2005.

Appendix A   Dimension Drawings

Tower:
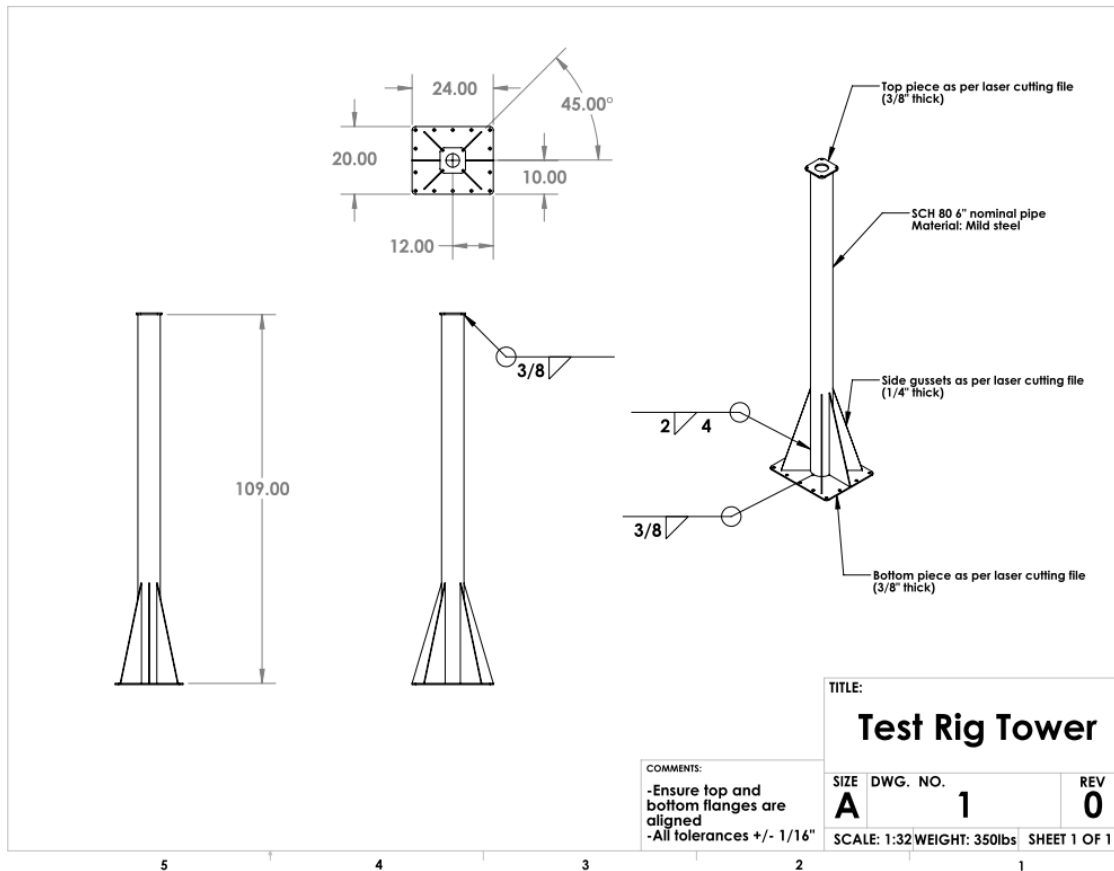
Figure A.1. Tower dimensions drawing, inches.

Nacelle frame:
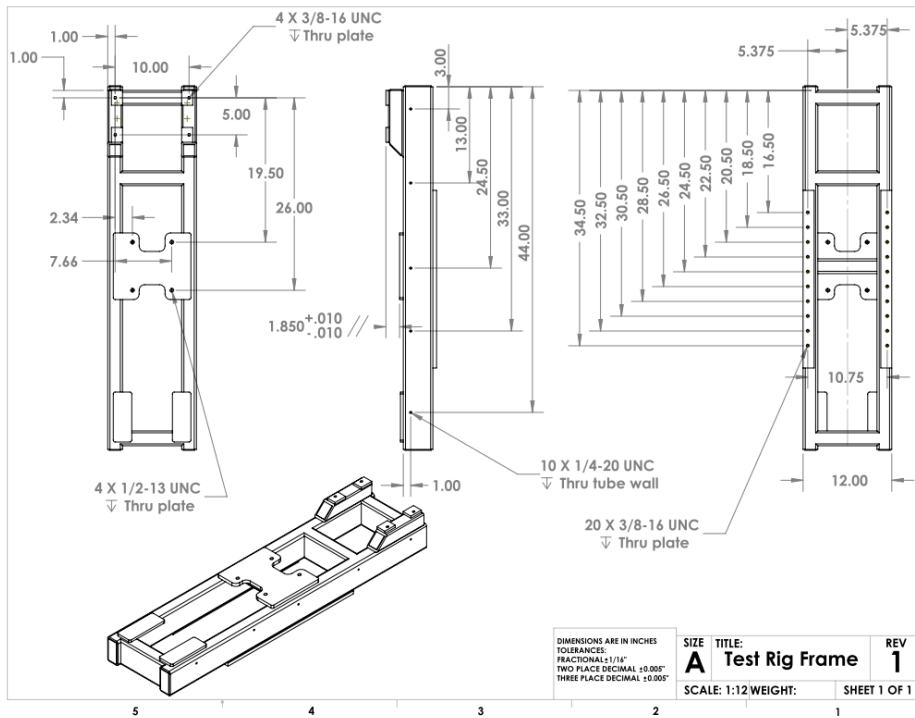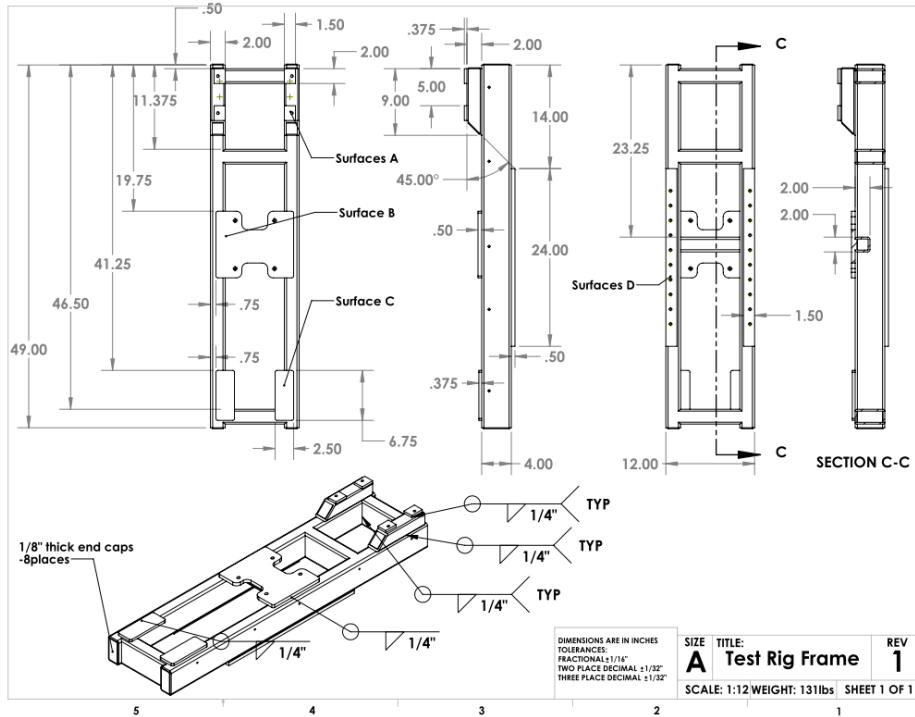
Figure A.2 Nacelle frame dimensions drawings, inches.

Nacelle cover:
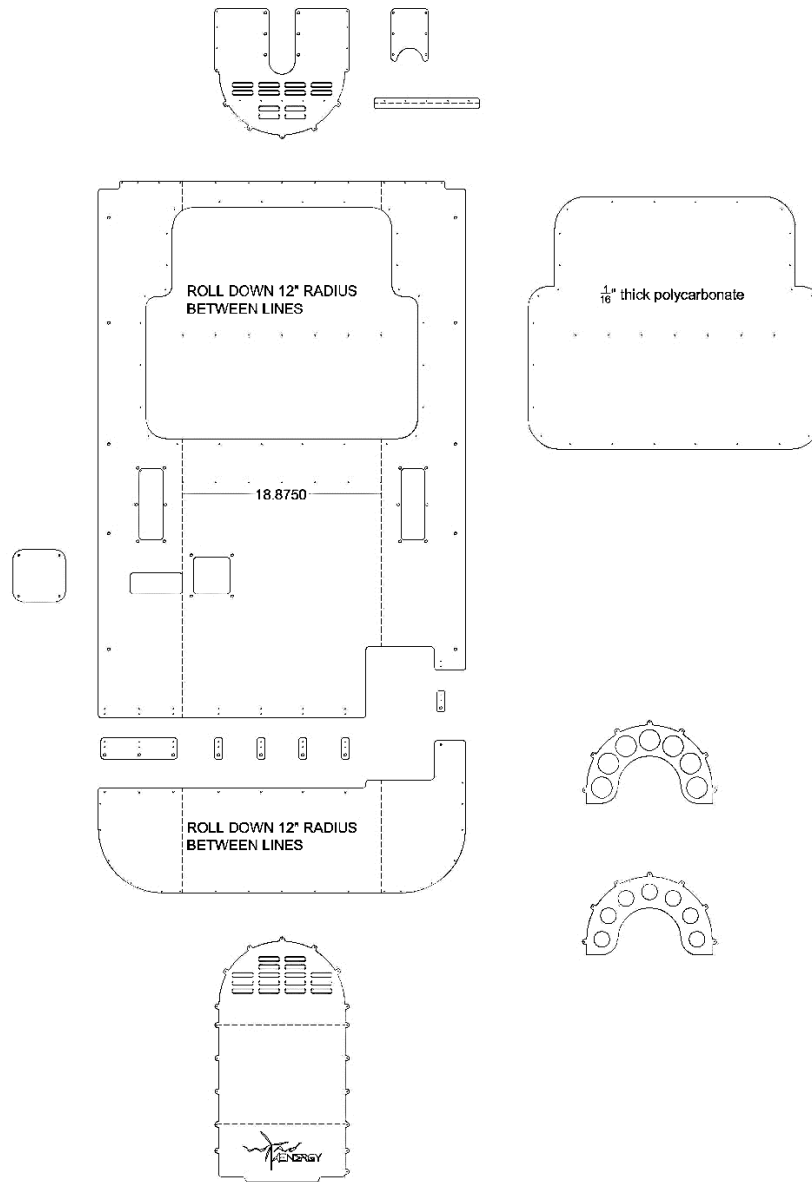
Figure A.3 Nacelle cover sheet metal parts.

The nacelle cover was first 3D modelled to fit the drive-train components while being as small and streamlined as possible. The design was converted to flat sheet metal drawings to be laser cut and rolled. Two internal webs add support to the nacelle structure and maintain the correct curvature. The final nacelle is assembled from two components, the main hull and the back cover.

Drive Shaft:
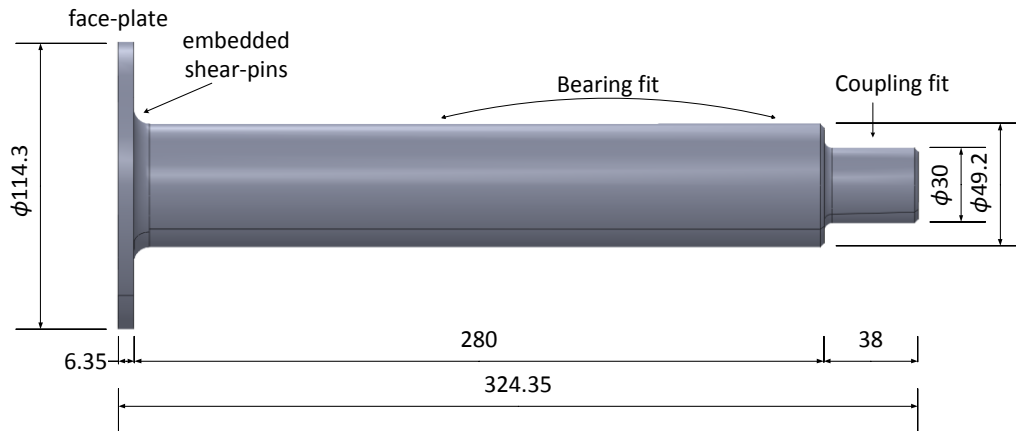
Figure A.4. Shaft dimensions in mm.

Appendix B   PROPID

PROPID Analysis input file:

Constant Chord/Twist Blade S833 Aerofoil

Basic input
MODE 1.0   # wind turbine
INCV 0.0   # wind turbine mode
LTIP 1.0   # use tip loss model
LHUB 1.0   # use hub loss model
IBR 1.0   # use brake state model
ISTL 1.0   # use viterna stall model
USEAP 1.0   # use swirl suppression
WEXP 0.0   # boundary layer wind exponent
NS_NSEC 10.0 1.0   # number of blade elements/number of sectors
IS1   1.0   # first segment used in analysis
IS2 10.0   # last segment used in analysis
BE_DATA 1   # printout blade element data
SH 0.0   # shaft tilt effects
RHO 0.0023769   # air density (slug/ft^3)

Geometry
HUB 0.11   # normalized hub cutout
HH 1.938   # normalized hub height
BN 1   # blade number
CONE 0.0   # cone angle of rotor (deg)
RD 5.578   # radius (ft)
CH_TW   # Normalized chord and twist distribution
  0.1041   6
  0.1041   6
  0.1041   6
  0.1041   6
  0.1041   6
  0.1041   6
  0.1041   6
  0.1041   6
  0.1041   6
  0.1041   6

```
# No stall models used
# CORRIGAN_EXPN 1

# Corrigan inputs are present but not used since stall model is off
AIRFOIL_MODE    4
2
S833_3D_trans_free.pd
.18  90  0  1.700  6  0  0  0
S833_3D_trans_free.pd
.18  90  0  1.700  6  0  0  0


# airfoil family 1 with 4 airfoils
# r/R-location and airfoil index
AIRFOIL_FAMILY    2
   .0000 1
   1.0000 2

# use the first airfoil family (the one above)
USE_AIRFOIL_FAMILY   1

# Enforce tip loss model to always be on
TIPON
# Use the Prandtl tip loss model,
# not the original modified model.
TIPMODE  2

# Design point: dsgnptnum, 200 rpm, 6 deg pitch, TSR 5 (8.5 m/s)
DP 1 200 6.00 8.5 1

# Initiate design (does some required preliminary work before analysis)
IDES

# Determine the rotor power, Cp, and thrust curves (2D_SWEEP)
#
# use rpm from design point (DP) 1 [200 rpm]
RPM_DP 1
# sweep pitch setting from 0% to 10% in increments of 1%
PITCH_FIXED 0
# sweep the wind from 0.5 to 10.5 m/s in increments of 0.5 m/s
WIND_SWEEP  0.5  10.5  0.5  1
# perform the sweep
2D_SWEEP
# write out data to files
# 40 - power curve (kW) vs wind speed (mph)
# 45 - Cp vs TSR
# 51 - rotor thrust curve
```

136

```
# 50 - rotor thrust vs TSR
WRITE_FILES  40 45 51 50

# Compute the gross annual energy production
# Output the data to file: gaep.dat
#
# Initial avg wind speed - 14 mph
# Final   avg wind speed - 18 mph
# Step              -  2 mph
# Cutout            - 45 mph
#
# 100% efficiency
GAEP  14 18 2 45
#
# 15 mph only, 85% efficiency
# GAEP  15 15 1 45 .85

# Obtain aero distributions along the blade (1D_SWEEP)
#
RPM_DP 1
PITCH_SWEEP 0 1 1
WIND_SWEEP  0.5  10.5  0.5  1
1D_SWEEP
# write out
# 75 - blade l/d  dist
# 76 - blade Re   dist
# 80 - blade alfa dist
# 85 - blade cl   dist
# 90 - blade a    dist
WRITE_FILES 75 76 80 85 90

# Write out
# 95 - chord dist (ft-ft)
# 99 - twist  dist (ft-deg)
WRITE_FILES 95 99

# Write out the rotor design parameters to file ftn021.dat
DUMP_PROPID
*
```

Appendix C   Calibration data

F_i (N)	R_{SG1} (mV/V)	$M_{\beta 1}$ (Nm)	R_{SG2} (mV/V)	$M_{\beta 2}$ (Nm)	F_i (N)	R_{SG1} (mV/V)	$M_{\beta 1}$ (Nm)
4.5	0.033	4.183	0.014	1.78	4.45	0.016	2.0915
8.9	0.064	8.366	0.027	3.56	8.9	0.032	4.183
13.4	0.095	12.549	0.040	5.34	13.35	0.048	6.2745
17.8	0.127	16.732	0.053	7.12	17.8	0.063	8.366
22.3	0.158	20.915	0.067	8.9	22.25	0.079	10.4575
31.2	0.220	29.281	0.092	12.46	31.15	0.109	14.6405
40.1	0.280	37.647	0.118	16.02	44.5	0.158	20.915
44.5	0.315	41.83	0.133	17.8	53.4	0.189	25.098
62.3	0.440	58.562	0.186	24.92	71.2	0.252	33.464
75.7	0.532	71.111	0.225	30.26	89	0.319	41.83
89.0	0.629	83.66	0.265	35.6	97.9	0.350	46.013
106.8	0.690	92.026	0.292	39.16	115.7	0.413	54.379
115.7	0.815	108.758	0.344	46.28	133.5	0.473	62.745
124.6	0.940	125.49	0.397	53.4	142.4	0.511	66.928
133.5	1.005	133.856	0.424	56.96	160.2	0.572	75.294
142.4	1.125	150.588	0.476	64.08	178	0.635	83.66
160.2	1.253	167.32	0.530	71.2	195.8	0.695	92.026
169.1	1.375	184.052	0.583	78.32	213.6	0.761	100.392
Linear analysis	$R_{SG} =$ $0.0075 M_{\beta 1} + 0.0012$		$R_{SG} =$ $0.0074 M_{\beta 1} + 0.00006$			$R_{SG} =$ $0.0076 M_{\beta 1} - 0.0004$	

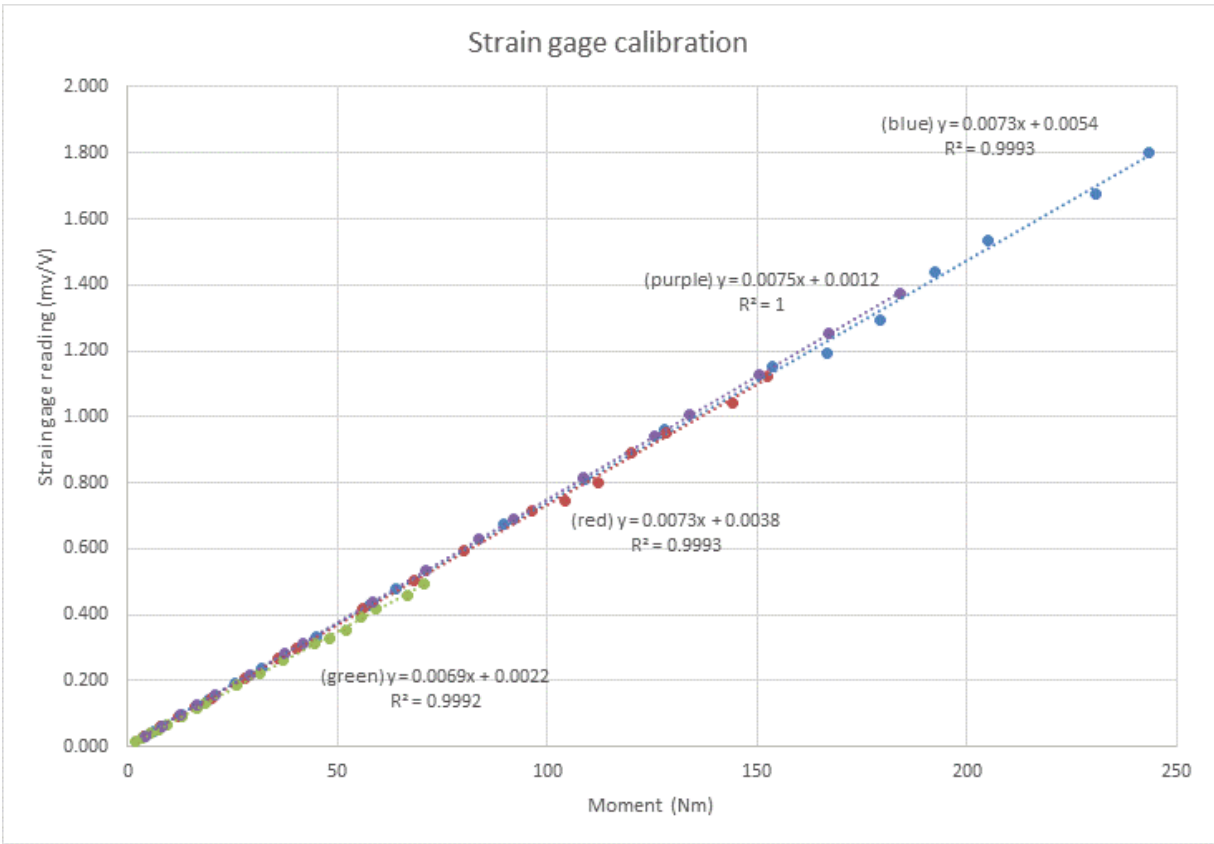Table C.1 Calibration data for load applied at d_3 Table C.2 Load applied at d_2

Figure C.1. Linear fit for select calibration data.

Appendix D   Test rig safety & maintenance

The test rig electrical equipment and connections were commissioned by the supplier and certified by the Canadian Standards Association (CSA). A table with critical fasteners and their required tightness can be found in [46]. These fasteners should be checked every month and whenever changes are made to the test rig assembly. This is an experimental test rig and the structure is not certified, revision of critical fasteners still does not guarantee the elimination on risk of structural disintegration of emergency breakdowns. The test rig should not be operated under any circumstances if any individuals are in the test area.

For a prolonged useful lifetime of the equipment and to preserve the alignment and operational efficiency, short and long term maintenance procedures should be performed. A schedule of maintenance can be found in [46].

Appendix E   Uncertainty Analysis

E.1 General Theory

Experimental measurements usually involve a certain level of uncertainty that may be caused by limited accuracy in measurement equipment, stochastic variations in measured quantities and data approximations [61]. Uncertainties can be estimated using two quantities; the precision uncertainty caused by random variation in data and the bias uncertainty caused by instrumentation inaccuracies. The total uncertainty u_r can thus be calculated using [62]:

$$u_r = \sqrt{p_r^2 + b_r^2}$$ <div align="right">E.1</div>

where p_r is the precision error, b_r is the bias error and the subscript r represents the measured quantity. A 95% confidence interval can be represented as $r \pm u_r$. Assuming a Gaussian distribution, the precision error may be calculated using the standard deviation of the mean for samples with greater than 10 measurements such that [62]:

$$p_r = \frac{2\sigma_r}{\sqrt{N}}$$ <div align="right">E.2</div>

where N is the number of measurements and σ_r is the standard deviation of the measurements. The bias error is estimated based on the type of measurement equipment and is usually listed by the manufacturer.

E.1.1 Derived parameters

If the parameter is derived through mathematical operations from more than one measured quantities the bias error for can be estimated using a partial derivative method. If the quantities are measured independently of each other the overall bias error for a derived quantity y is calculated as follows [62]:

$$b_y = \sqrt{\sum_{i=1}^{s}\left(\frac{\partial y}{\partial x_i}b_{x_i}\right)^2}$$ <div align="right">E.3</div>

where b_{r_i} is the bias error of the measured quantity x and s is the number or measurement quantities. If the measured quantities are dependant, an additional term is added under the root. Assuming measured quantities 1 and 2 are correlated, then the bias error would be calculated as [62]:

<div align="center">141</div>

$$b_y = \sqrt{\sum_{i=1}^{s} \left(\frac{\partial y}{\partial x_i} b_{x_i}\right)^2 + 2 \frac{\partial y}{\partial x_1} \frac{\partial y}{\partial x_2} b'_{x_1} b'_{x_2}} \qquad \text{E.4}$$

Bias errors for some measured quantities are shown in Table E.1.

Measurement	Instrument	Label	Uncertainty
Wind speed	Sonic Anemometer	W	± 8.0 cm/s [57]
Strain	Strain gage	R_{SG}	± 0.35% [56]
Flap angle	Digital protractor	η	± 0.5° (estimate)
Strain gage location	Tape measure	d_i	± 0.5mm (estimate)

Table E.1 Bias error for measured quantities

Strain gage constant K

The strain gage constant was calculated using equation 5.6, its bias error is derived from the regression analysis and its total uncertainty is calculated as follows:

$$u_K = \sqrt{p_k^2 + b_k^2} \qquad \text{E.5}$$

where p_k is the precision error of the calibration and is calculated from the standard deviation of the calibration measurements.

Flapwise bending moment M_r

The moment measured at any radial position r was calculated using equation 5.7, its bias error is calculated as follows:

$$b_M = \sqrt{\left(\frac{1}{K} b_{R_{SG_i}}\right)^2 + \left(\frac{R_{SG}}{K^2} b_K\right)^2} \qquad \text{E.6}$$

The total uncertainty is calculated as follows:

$$u_M = \sqrt{p_M^2 + b_M^2} \qquad \text{E.7}$$

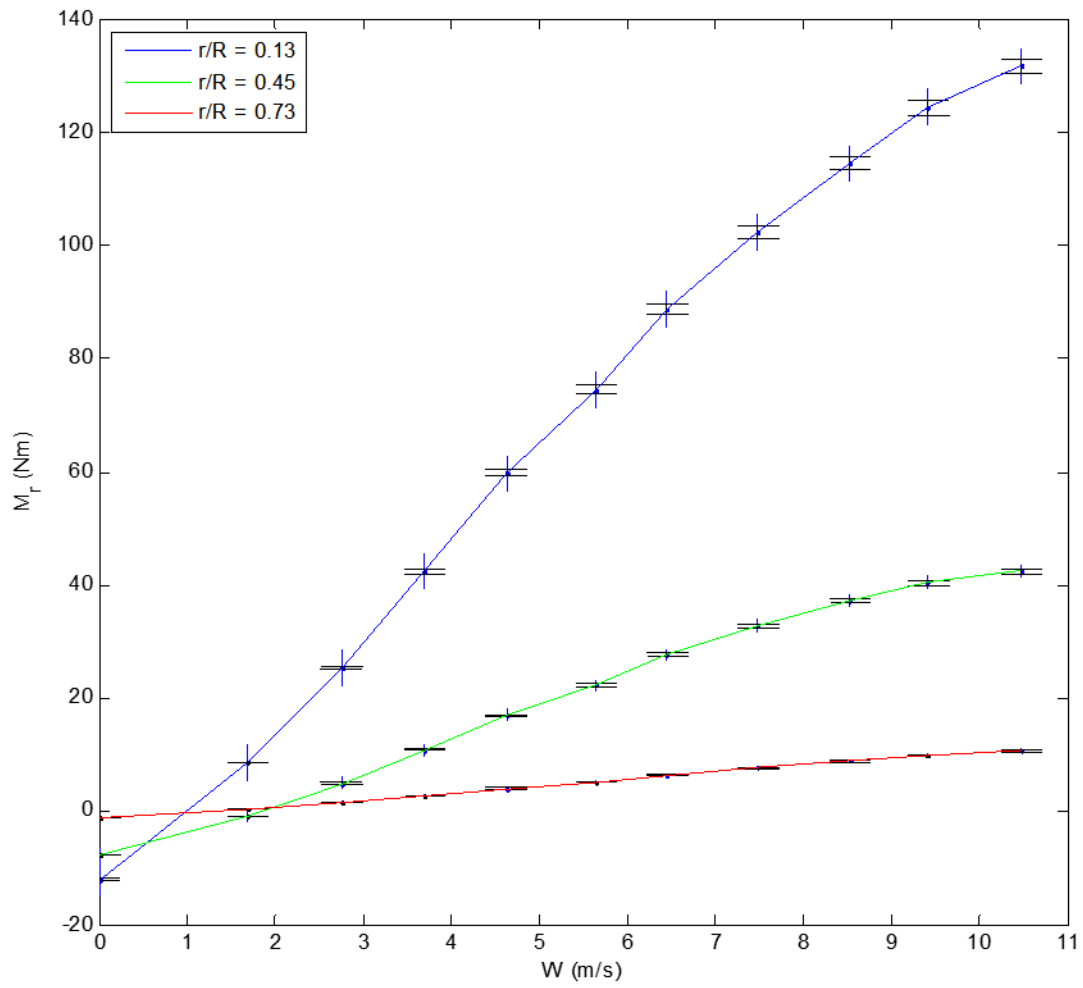Where p_M is the precision error and is calculated from the standard deviation of the measurements.

Figure E.1. Error bar plot for moment readings.